Use of Multibody System Techniques in the Analysis of Railroad Vehicle Stability and Derailment

BY

JAMES J. O'SHEA
B.S., University of Illinois at Chicago, Chicago, 2011

THESIS

Submitted as partial fulfillment of the requirements
for the degree of Doctor of Philosophy in Mechanical Engineering
in the Graduate College of the
University of Illinois at Chicago, 2016

Chicago, Illinois

Defense Committee:

Ahmed A. Shabana, Chair and Advisor, Mechanical and Industrial Engineering
Craig D. Foster, Civil and Materials Engineering
Mohsen A. Issa, Civil and Materials Engineering
Eduard Karpov, Civil and Materials Engineering
Martin B. Hamper, Toyota

This dissertation is dedicated to my parents, James and Cynthia O'Shea. Their sacrifices have provided me with opportunities and experiences that have proved invaluable. I would like to additionally recognize the following people: Kelcie Gauen, for all of her love and support; the members of TDC Mixed Martial Arts, for teaching me the lessons that cannot be found in a classroom; and the members of Beta Kappa Zeta fraternity, for their companionship.

ACKNOWLEDGEMENTS

I would like to thank my advisor, Dr. Ahmed A. Shabana. This thesis would not be possible without the opportunities that he has provided me. I would also like to thank the members of my dissertation committee: Dr. Craig Foster, Dr. Martin Hamper, Dr. Eduard Karpov, and Dr. Mohsen Issa. I appreciate the comments and efforts of Dr. Paramsothy Jayakumar and Dave Mechergui, which guided the work on which we collaborated. I would like to acknowledge the support that I received from both the National University Rail (NURail) Center as well as Computational Dynamics, Inc. Finally, I would also like to thank my colleagues from the Dynamic Simulation Laboratory for the many times in which they have assisted me.

JJO

CONTRIBUTION OF AUTHORS

Chapter 2 represents a published manuscript (Shabana et al., 2012). My research advisor, Dr. Ahmed A. Shabana, contributed to the writing of the manuscript. My colleague, Dr. Martin B. Hamper, contributed to the numerical simulations. **Chapter 3** represents work that is under preparation (O'Shea and Shabana, 2016). My research advisor, Dr. Ahmed A. Shabana, contributed to the review of this manuscript. **Chapter 4** represents a published manuscript (O'Shea and Shabana, 2013). My research advisor, Dr. Ahmed A. Shabana, contributed to the description and formulation of the semi-analytical model, as well as the review of the entire manuscript. **Chapter 5** represents work that is not yet published (O'Shea et al., 2016). My research advisor, Dr. Ahmed A. Shabana, contributed both to the writing and review of the manuscript. Dave Mechergui contributed to the numerical simulations of the slider-crank examples. Dr. Paramsothy Jayakumar contributed to the review and guidance of the work.

TABLE OF CONTENTS

TABLE OF CONTENTS (continued)

TABLE OF CONTENTS (continued)

TABLE OF CONTENTS (continued)

LIST OF TABLES

LIST OF FIGURES

LIST OF FIGURES (continued)

LIST OF FIGURES (continued)

LIST OF FIGURES (continued)

SUMMARY

Parts previously published in (Shabana et al., 2012; O'Shea and Shabana 2015; O'Shea and Shabana, 2016; and O'Shea et al., 2016) and reproduced in this dissertation with permission which is provided in Appendix A. Dr. Martin Hamper, Dr. Paramsothy Jayakumar, and David Mechergui are contributing authors.

In railroad vehicle system dynamics, the effect of the gyroscopic moments can be significant during curve negotiations. The absolute angular velocity of a vehicle component during curve negotiations can be expressed as the sum of two vectors; one vector is due to the curvature of the curve, while the second vector is due to the rate of change of the angles that define the orientation of the body with respect to a coordinate system that follows the body motion. In this dissertation, the configuration of the body in the global coordinate system is defined using a set of trajectory coordinates in order to examine the effect of the gyroscopic moments in the case of curve negotiations. These coordinates consist of an arc length, two relative translations, and three relative angles. The relative translations and relative angles are defined with respect to a trajectory coordinate system that follows the motion of the body about the curve. It is shown that when the yaw and roll angles relative to the trajectory coordinate system are constrained and the motion is predominantly rolling, the effect of the gyroscopic moment on the motion becomes negligible and, in the case of pure rolling and zero yaw and roll angles, the generalized gyroscopic moment associated with the system degrees of freedom becomes identically zero. Furthermore, the analysis presented in this dissertation shows that the roll moment, which can have a significant effect on the wheel/rail contact forces, depends on the forward velocity in the case of curve negotiations.

For this reason, roller rigs and other test apparatus that do not allow for the wheelset forward velocity cannot capture these moment components correctly and, therefore, should not be used in the analysis of curve negotiations. A multibody system (MBS) model of a suspended railroad vehicle wheelset is developed and used in this investigation to numerically study the gyroscopic effect during curve negotiations.

Curve negotiations, in addition to developing significant gyroscopic effects, can position a wheelset such that it is prone to a mode of derailment referred to as wheel flange climb. In previous research, a set of nonlinear algebraic kinematic constraint equations were developed that describe the configuration of a wheelset in contact with a track at two distinct points. In such a case of two points of contact, a simplified wheelset model that has the lateral displacement and angle of attack (AOA) as the independent variables can be developed. In this dissertation, this approach is extended to the case of a wheelset in contact with a tangent track at three distinct points. The solution of this three-point contact problem requires specifying the wheelset AOA only. This wheelset configuration is significant in derailment investigations because it is a possible configuration at the initiation of a wheel climb derailment. In order to study this wheel climb initiation configuration, a set of nonlinear kinematic constraint equations is developed as a function of the wheelset AOA and solved for the unknown system coordinates and contact surface parameters using an iterative Newton-Raphson algorithm. The wheelset AOA during wheel climb derailments can be determined forensically at the derailment site, making this approach of practical significance. It is shown that the system configuration can be fully defined for wheel climb derailment initiation, which allows for the investigation of various derailment parameters such as

the wheel/rail contact angle. Furthermore, the wheelset flange angle, which is the angle between the tangent to the wheel surface at the contact point and the wheelset axle, is shown to not be representative of the wheel/rail contact angle, which is the angle between the tangent to the contact surfaces and the lateral common tangent to the two railheads; this distinction can only be demonstrated through full definition of the system configuration that accounts for the wheelset roll angle.

A fully nonlinear unconstrained MBS wheel climb derailment model is developed to analyze the forces that govern the wheel climb motion when oriented at a large AOA. The results of the MBS model in the vicinity of the climb initiation are verified using a semi-analytical model that makes use of simplifying assumptions derived from the current interpretation of wheel climb. It is shown that, when the wheel makes flange contact with the rail at a large AOA, the lateral and vertical displacements of the wheel become coupled due to motion constraints resulting from the wheel/rail contact. This constraint produces kinematic contributions to the wheel climb motion that are shown to be significant throughout the motion. Additionally, the friction force developed at the point of contact is shown to be three dimensional, and therefore, concerns are raised regarding the validity of any planar force balance at the point of contact to capture such motion. Regardless, the forces measured at contact point are shown to not represent the forces that drive the derailment. This model is used to support the three-point contact formulation outlined above. It is seen that the initiation of the wheel climb motion is correctly predicted using proper geometry definitions in the derailment criteria, whereas such motion was not correctly predicted using geometry definitions derived from the wheelset flange angle.

The analysis presented in this investigation sheds light on the danger of using any derailment criteria that are not obtained using laws of motion. The Nadal L/V derailment limit, as well as any investigation that chooses to neglect the wheelset orientation or the effect of such orientation on the wheel/rail contact geometry, is called into question. Therefore, such criteria should not be used in judging the stability of railroad vehicle systems. Most importantly, however, the Nadal L/V derailment limit is shown to not be conservative for all cases. It is demonstrated that, with proper formulation, more accurate and justifiable criteria can be developed. Taking these important results into account, questions must be raised regarding the current interpretation of wheel climb, which does not account for kinematics, as well as the various derailment criteria that have roots in Nadal's derivation. This investigation is not intended as a derailment criteria proposal, but rather as support and rationalization for the use of correct contact geometry in derailment investigations.

With the rate of computer development, the desire for the modeling of deformable vehicle components in MBS models has grown. The floating frame of reference (FFR) formulation is widely used in the analysis of deformable bodies in MBS simulations. The modeling of deformable bodies requires the use of elastic degrees of freedom, which can increase the model size significantly. Therefore, modal reduction techniques have been proposed in order to define a proper set of assumed body deformation modes at a preprocessing stage. Crucial to the proper definition of these modes when the finite element (FE) FFR formulation is used is the understanding of the concept of the reference conditions that define the nature of the deformable body coordinate system. Substructuring techniques, such as the Craig-Bampton method, on the

other hand, have been proposed to allow for efficient model assembly and reduce model dimensionality. However, it is important to distinguish between substructuring techniques which aim at obtaining efficient model assembly and coordinate reduction and the reference conditions that define the problem to be solved. In this study, the appropriateness and generality of using the Craig-Bampton method in MBS implementation is discussed. It is shown that, when a set of reference conditions are not applied at a preprocessing stage, the Craig-Bampton transformation leads to the free-free modes of deformation as well as the natural frequencies associated with these modes. It is also shown that a square Craig-Bampton transformation is equivalent to a similarity transformation that does not alter the problem to be solved. Therefore, the goal of using the Craig-Bampton transformation is not to improve the solution accuracy, but rather to obtain a reasonably accurate solution using lower dimension models, as with any other substructuring method. This dissertation also demonstrates that free-free deformation modes cannot be used in all applications, shedding light on the importance of the concept of the reference conditions when using the FE/FFR formulation in modeling flexible bodies in MBS applications. To this end, this dissertation demonstrates numerically for the first time that the unique resonance frequency of a model can be achieved using the definition of different mode shapes associated with different boundary conditions provided that the shapes are similar. Due to the subtleties inherent to the FFR formulation, care must be taken when using and/or designing flexible MBS software in order to obtain acceptable results.

CHAPTER 1

INTRODUCTION

Parts previously published in (Shabana et al., 2012; O'Shea and Shabana 2015; O'Shea and Shabana, 2016; and O'Shea et al., 2016) and reproduced in this dissertation with permission which is provided in Appendix A. Dr. Martin Hamper, Dr. Paramsothy Jayakumar, and David Mechergui are contributing authors.

1.1 Derailment Modes

There are two common derailment scenarios which have been investigated in the railroad vehicle dynamics literature: flange wheel climb and wheel lift. Flange climb derailments are more frequent and can occur at low velocity. It is believed that the flange wheel climb, which is often associated with a large angle of attack (AOA), is the result of a tangential force that produces a contact force that acts upward at the wheel/rail contact point. The wheel lift, on the other hand, can be the result of hunting-produced high lateral velocity and large impact forces that can cause derailments. In this derailment scenario, the tangential force at one wheel can be downward as the result of the wheel lift at the other wheel (Wang and Li, 2010).

1.2 The Gyroscopic Moment

The gyroscopic moment, which is an inertia moment, is the result of multi-axis rotation of a body (Goldstein, 1950; Greenwood, 1988; Roberson and Schwertassek, 1988; Shabana, 2010). In the case of simple rotation about a fixed axis, the gyroscopic moment vanishes. While in some curving scenarios the change in some angles can be restricted, curving motion contributes to the gyroscopic

moment even in the special case when two rotations of the body relative to the curve are not allowed. The gyroscopic moment can have a significant effect in many applications including aerospace and rail systems.

1.3 Wheel Climb Derailments

The wheelset AOA is defined to be the angle α^w between the vector defining the wheel forward velocity and the tangent to the rail at the contact point, as shown in Fig. 1.1.

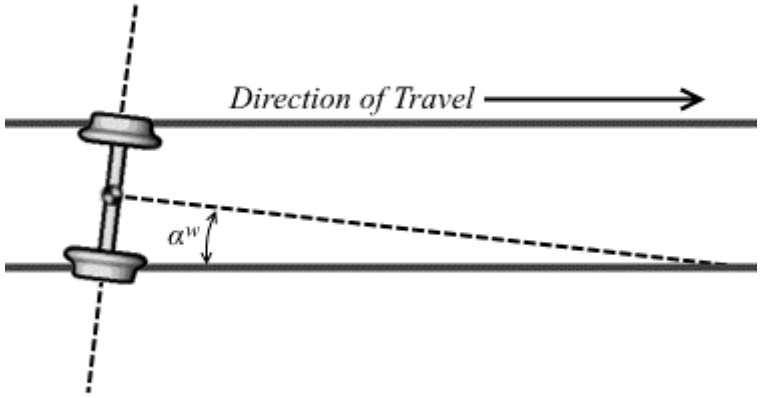

Figure 1.1. Wheelset Angle of Attack

The AOA may differ from zero during curving or in the case of unstable motion. Railroad vehicle wheelsets are designed in such a way that, when the AOA differs from zero, an additional point of contact may be made on a wheel flange in order to prevent the wheel from falling off the rail. Contact may occur exclusively at the wheel tread surface, exclusively at the wheel flange surface, or at both the wheel tread and flange surfaces. A wheel climb derailment is essentially the derailment mode in which a flanging wheel "climbs" the rail, eventually allowing the wheel to shift outside the track.

This motion, in general, creates momentarily a three-point contact scenario between the wheelset and track, which can be considered a configuration for the initiation of wheel climb derailments. The contact of the wheel flange with the rail produces contact and reaction forces that can have significant magnitude and restrict the motion of the wheel, causing wheel climb and derailment. These contact forces act in addition to the inertia, gravity, and suspension forces that act on the wheel axle.

Wheel climb then becomes one of the important derailment scenarios of railroad vehicle systems, particularly in the case of a large wheelset AOA. In order to understand the phenomenon of wheel climb at a large AOA, the application of the principles of mechanics is necessary (Goldstein, 1950; Greenwood, 1988; Roberson and Schwertassek, 1988; Shabana, 2010). Wheel climb derailments can occur at low speeds and without any indication to the vehicle operator, and therefore, have been the target of numerous investigations (Blader, 1990; Elkins and Wu, 2000; Marquis and Grief, 2011; Shust et al., 1997; Wu and Elkins, 1999; Wu et al., 2005, Wu and Wilson, 2006; Wilson et al., 2004). These investigations have produced derailment criteria which aim to measure the risk of and prevent such derailments.

1.4 Investigations and Derailment Criteria

The development and validation of derailment criteria have been the subject of numerous investigations (Blader, 1990; Elkins and Wu, 2000; Marquis and Grief, 2011; Shust et al., 1997; Wu and Elkins, 1999; Wu et al., 2005; Wu and Wilson, 2006; Wilson et al., 2004). These criteria have been used to develop operation and safety guidelines. Examples of these criteria are the Nadal single-wheel L/V limit criterion (Nadal, 1896; Nadal, 1908), Weinstock axle-sum L/V limit criterion, FRA high speed passenger distance limit (5 ft), AAR Chapter 11 50-millisecond time limit, Japanese National Railway (JNR) L/V time duration criterion, EMD L/V time duration criterion, and the TTCI wheel climb distance criterion.

Nadal used a simplified and planar force balance to derive a derailment quotient L/V at which wheel climb can occur, where L and V are the lateral and vertical contact forces at the wheel flange. While Nadal's formula is not function of the AOA, the relation is algebraic and has been used to provide intuition-based explanations for wheel climb in the case of large AOA (Shabana, 2012). Weinstock's criterion, which considers two wheels instead of a single wheel, predicts derailment by summing the absolute values of the L/V ratios of two wheels on the same axle (Weinstock, 1984). This sum is known as the axle sum L/V ratio. Weinstock's criterion considers the friction at the non-flanging wheel. If the coefficient of friction at the non-flanging wheel approaches zero, Weinstock's criterion converges to Nadal's criterion (Shabana, 2012). The JNR and EMD time duration criteria are based on modifications to the Nadal's criteria by increasing the L/V limit if the duration of the lateral thrust is less than certain time duration. In the JNR criterion, this time duration is assumed to be 50 ms (Matsudaria, 1963). The EMD is considered less conservative (Koci and Swenson, 1978). The AAR wheel climb duration limit

recommends the use of 50 ms (0.05 s); while the FRA wheel-climb distance limit recommends the use of 5 ft limit for class 6 and higher for high speed rail systems. The TTCI wheel climb distance criterion considers both Nadal's L/V limit and the L/V distance limit. This criterion, which was developed for freight trains with AAR1B wheel profile and $75°$ flange angle, is considered applicable at speeds lower than 80 km/h in the case of curve negotiations. Nadal's ratio can also be used to show that wheels with low flange angles have a lower L/V ratio, and therefore, have higher risk of derailment. Results for the effect of flange angle ranging from $63°$ to $75°$ on the L/V ratio were reported in the literature. The increase of the flange length can also lead to an increase of the flange climb distance limit, particularly when the AOA is small (Wu and Elkins, 1999; Wilson et al., 2004).

1.5 Nadal Derailment Limit

A large majority of the aforementioned derailment criteria have their roots in the well-known Nadal L/V derailment limit. Nadal's formula was proposed in order to provide a *derailment limit* on the ratio of the lateral flange/rail contact force to the vertical flange/rail contact force; in other words the value at which the wheel climb derailment process will initiate. The formula is given as

$$L/V = \left(\tan\bar{\delta} - \mu\right) / \left(1 + \mu\tan\bar{\delta}\right) \tag{1.1}$$

where $\bar{\delta}$ is a wheel flange angle that defines the angle between the tangent to the wheel surface at the point of contact and the wheelset axle. The variable μ is the coefficient of friction between the flange and rail. This formula was derived in a two-dimensional space shown in Fig. 1.2,

assuming that the contact forces can be decomposed into tangential and normal components T and N defined in the track coordinate system (Nadal, 1896; Nadal, 1908).

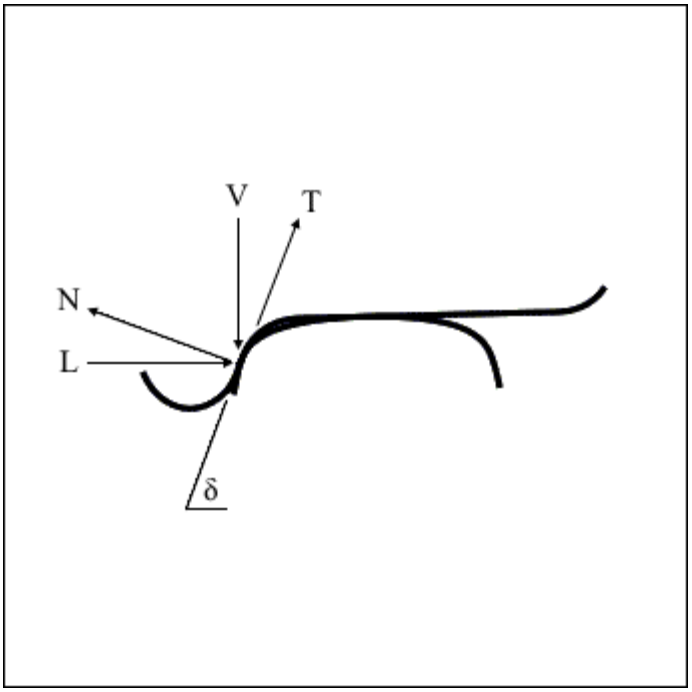

Figure 1.2. Nadal Wheel Climb Interpretation

In addition, Nadal's ratio does not consider the contact with the track at the other wheel. This formula, although attempting to capture the case of a wheel climb derailment, fails to take into account the AOA (or any wheelset orientation for that matter) at which the derailments occur. Consequently, the effect of the wheelset orientation on the contact geometry is not considered as well, and as a result, the correct geometry is not captured by Nadal's formula. Although subsequent criteria have been developed in an attempt to improve Nadal's derailment limit, Nadal's criteria is still used today because of its simplicity.

Numerous investigations have used the Nadal limit in the investigation of derailment prevention or to compare new derailment criteria (Cherchas, 1981; Leary et al., 1991; Pearce, 1996; El-Sibaie et al., 1997; Matej et al., 2002; Nagase et al., 2002; Fraser et al., 2003; Xiao et al., 2008; Zeng and Guan, 2008; Atmadzhova and Mihaylov, 2010; Schindler et al., 2010; Mahyuddin and Febriartanto, 2011; Mohammadzadeh et al., 2011; Choi et al., 2012; Kumar, 2014; Simpson et al., 2014). Additionally, numerous investigations fail to recognize the movement of the contact point, assume that the contact point occurs at the steepest section of the flange, or neglect the wheelset yaw and roll rotations (Gilchrist and Brickle, 1976; Nagurka et al., 1982; Weinstock, 1984; Ishida and Matsuo, 1999; Takai et al., 2002; Ghazavi and Taki, 2008; Magel et al., 2008; Nagumo et al., 2010; Koo and Oh, 2014; Wei et al., 2014). Other investigations have attempted to extend or correct Nadal's derivation (Barbosa, 2004; Braghin et al., 2006; Kardas-Cinal, 2009), and some recent investigations have recognized the importance of the wheelset orientation as well as the movement of the contact point (Sato et al., 2008; Zeng and Wu, 2008; Santamaria et al., 2009; Durali and Jalili, 2010; Wang and Li, 2010; Marquis and Greif, 2011; Guan et al., 2014).

1.6 Substructuring and CMS in Vehicle Applications

Complex vehicle systems can consist of many different components that can be classified as either rigid or flexible bodies. Thus, developing multibody system (MBS) models of such systems requires the formulation of the equations of motion of the deformable components which have infinite number of degrees of freedom. Nonetheless, infinite-dimension spaces are not suitable for computational approaches, and therefore approximation techniques, such as the finite element (FE) method, are often used. In the FE method, the bodies or structures are subdivided into small

structures called elements connected at points called nodes. Each node has a finite number of nodal degrees of freedom which are used to approximate the deformation of the body. In the conventional FE approach, these degrees of freedom are a combination of nodal displacements and linearized rotations. Element interpolation functions then define the element kinematics between the nodal points.

In order to obtain accurate results, a deformable body may be discretized into a very fine mesh of elements. Using a fine mesh, however, can lead to a model with a very large number of system degrees of freedom, therefore requiring significant computational effort. The desire for computational efficiency, while retaining accuracy, prompted the development of coordinate reduction techniques such as component mode synthesis (CMS) methods. In these methods, modal decomposition of the system produces a modal transformation matrix whose columns are the normal vibration modes of the system. The columns of this matrix are truncated in order to eliminate insignificant high-frequency vibration modes. The truncated modal transformation matrix relates the nodal degrees of freedom to a smaller number of modal coordinates, thus reducing the problem dimensionality. The transformed equations of motion can then be solved more efficiently using numerical methods.

The desire for design collaboration between research and development groups working within an industry on modeling very complex systems such as large scale aircraft models prompted the development of model substructuring techniques. Substructuring techniques allow for dividing a complex and large scale structure into several substructures. The mesh of each substructure can be developed independently and coordinate reduction techniques can be applied to each substructure mesh in order to reduce the dimensionality of the substructure model which is defined

in terms of interface nodes. Using the interface nodes, a reduced-order structure mesh can be obtained by assembling its reduced-order substructure meshes. A popular substructuring technique, which is widely used in MBS software and will be discussed in detail in later sections of this dissertation, is the *Craig-Bampton method* (Bampton and Craig, 1968). In the Craig-Bampton method, a coordinate partitioning separates the substructure elastic coordinates into *boundary* and *internal coordinates*. Static condensation of the stiffness matrix produces a set of constraint modes. Meanwhile, performing an eigenvalue analysis of the problem associated with internal degrees of freedom produces a set of fixed-interface modes. Combination of these two mode sets defines the Craig-Bampton transformation.

1.7 Scope and Organization of the Thesis

Chapter 2 was first published in *Computational and Nonlinear Dynamics* (Shabana et al, 2012). This chapter discusses the effect of the gyroscopic moments in the case of curve negations in order to have a better understanding of their significance in the case of railroad vehicle system dynamics.

In order to understand the effect of the gyroscopic moment in the case of curve negotiations, the motion of the body is described using a set of trajectory coordinates which consist of an arc length that defines the distance travelled by the body on the curve, two relative translational displacements, and three relative angles. The relative translations and relative angles define the configuration of the body with respect to a trajectory coordinate system that follows the body motion. It is shown that the body angular velocity vector can be written as the sum of two vectors; one of them is due to the curvature of the curve, while the second depends on the relative rotation of the body with respect to the trajectory coordinate system. This angular velocity depends

on the time rate of the distance travelled on the curve as well as the time rate of the relative angles (yaw, roll, and pitch). If the yaw and roll angles are constrained and the motion is predominantly rolling, the generalized gyroscopic moment associated with the degrees of freedom can be negligible. It will be demonstrated in this chapter that, in the case of pure rolling motion with constraints imposed on the yaw and roll angles, the Cartesian gyroscopic moment can be different from zero but the generalized gyroscopic moment associated with the degrees of freedom will always be zero.

It is important, however, to point out that the gyroscopic moment can be significant in the dynamic and stability analysis of railroad vehicle systems. The gyroscopic moments can significantly influence the wheel/rail contact forces during curve negotiations, and therefore, the effect of this inertia moment must be considered in the analysis of derailment of railroad vehicle systems. In the analysis of derailment scenarios, all the moments acting on the wheelset, including the gyroscopic moment, must be taken into consideration. This is particularly important in the dynamic and stability analysis of high speed rail systems. The analysis presented in this chapter sheds light on the danger of using derailment criteria that are not obtained using laws of motion, and therefore, should not be used in judging the stability of high speed railroad vehicle systems. (Shabana, 2012).

Chapter 3 was originally prepared in (O'Shea and Shabana, 2016). This chapter is concerned with the initiation configuration of flange wheel climb derailments that occur at a large wheelset AOA. In this chapter, a three-dimensional kinematic problem is formulated and solved using the AOA as an input. The results obtained using this kinematic problem, which is used to shed light on the wheel climb initiation, are verified using a fully nonlinear three-dimensional

unconstrained MBS model that allows for the wheel/rail separation. A vector of algebraic kinematic constraint equations is formulated assuming that the track is fixed in space. These kinematic equations, which define the wheel/track three-point contact scenario, are function of the wheelset AOA. For a given AOA, these equations can be solved for both the wheelset coordinates and the surface parameters used to define the geometry of the contact surfaces. This system of equations is solved for the unknown variables using numerical methods. Knowing the system coordinates and surface parameters, the wheelset flange angle, and subsequently the contact angle, can be correctly determined. The two angles are then compared for different values of the wheelset AOA, and the effect on the Nadal formula is investigated.

The necessity of using correct contact geometry when investigating the onset of wheel climb is discussed. Nadal's formula does not account for any wheelset orientation that is typical of a three-point contact scenario, and therefore, does not capture the correct wheel/rail contact geometry. Nadal measured the flange angle $\overline{\delta}$ with respect to the wheelset axle, while the contact angle is measured with respect to the lateral common tangent to the two railheads. As a result, the two values will be, in general, different from each other. Additionally, one cannot neglect the wheelset orientation and assume that the wheel flange will contact the rail at its steepest point during climb investigations.

It is the purpose of this chapter to shed light on and reinforce the importance of taking into account the wheelset orientation as well as to demonstrate that, for a wheelset in contact with a tangent track at three distinct points, the system configuration can be fully defined given the wheelset AOA. It is intended that the analysis presented in this chapter will be used to determine

important derailment parameters and to fully understand the wheel climb derailment initiation problem.

Chapter 4 was first published in *Nonlinear Dynamics* (O'Shea and Shabana, 2015) and contains parts prepared in (O'Shea and Shabana, 2016). This chapter investigates wheel *climb initiation* with respect to the wheelset degrees of freedom, demonstrating that the motion is a largely kinematic phenomenon.

Some researchers make the argument that, in the case of a positive AOA and positive pitch angular velocity, the wheel flange contact point on the wheel moves downward thereby creating a significant upward friction force if the lateral force significantly increases, leading to a wheel climb derailment. This interpretation of the wheel climb derailment implies that the initiation of the climb motion is kinetic- (force) based, which requires time history for such a climb initiation since any change in the acceleration does not instantaneously affect the positon coordinates.

However, as the result of the wheel flange contact with the rail, the motion of the wheel instantly becomes more restricted, thereby allowing the wheel to move only in specific directions. This restriction is a kinematic motion constraint that is applied instantaneously as the wheel flange comes into contact with the rail, preventing the wheel from penetrating the rail. The kinematic contribution to the climb motion cannot be ignored and is fundamentally different from a kinetic-based climb initiation. Kinematic wheel climb contributions can be dangerous since they are instantaneous and do not require significant applied (external) lateral forces for the initiation.

It is, therefore, the objective of this chapter is to investigate this argument by demonstrating, using the results of a new fully nonlinear unconstrained MBS wheelset derailment model, that the initiation of wheel climb can be instantaneous, does not require significant lateral

forces, and has significant contribution from kinematic conditions that require the wheel to move upward. The MBS model is three dimensional, fully nonlinear, places no constraints on the motion of the wheelset, takes into account the geometry of the wheel and rail profiles, and allows for wheel/rail separation. In the vicinity of the climb initiation, the results obtained using the fully nonlinear unconstrained wheelset model can be validated using the results of a simplified semi-analytical model, which was originally introduced at conference in (Shabana and O'Shea, 2013). The results of the MBS model are then compared against an updated result obtained using the correct geometry definition in the derailment criteria, as formulated in Chapter 3.

The fact that the initiation of wheel climb does not, in general, require significant lateral forces raises questions with regard to the application of many derailment criteria in the case of relatively large AOA. Such a scenario requires the use of three-dimensional analysis that employs both generalized coordinates and non-generalized geometric parameters; the latter are required for accurate and general description of the contact surfaces. The analysis presented in this chapter, therefore, sheds light on the appropriateness of using the intuition-based L/V criteria and the nature of the measured L and V forces. The results of the two models agree that Nadal's Limit is not a conservative criterion when wheel climb scenarios are considered. This conclusion is reached using two very different models, and is one of the main contributions of this dissertation.

Chapter 5 was originally prepared in (O'Shea et al., 2016) and is concerned with CMS and substructuring techniques in the analysis of vehicle systems that consist of rigid and deformable components. The goal of using CMS and substructuring techniques is to develop a convenient form of an already well-defined problem, which has a unique solution that does not depend on the solution method used, and to solve this problem at a lower computational cost. CMS

and substructuring techniques should not be viewed as techniques that will lead to improved or altered solutions. Instead, they should be viewed as techniques that can be used to obtain, more efficiently, a good approximation for the unique solution of the well-defined problem.

CMS and substructuring techniques lead to transformations in which a set of coordinates is expressed in terms of another set of coordinates that have a certain physical meaning that allows for coordinate reduction. If coordinate reduction is used, the resulting coordinate transformation matrix is non-square. The accuracy of the approximate solution, regardless of the method used, should be measured against the solution obtained using the square transformation (exact solution with no coordinate reduction). The solution of the reduced order model is judged as accurate if convergence to the exact solution is obtained.

For example, consider the original problem defined by the mathematical model $\mathbf{M}\ddot{\mathbf{q}} = \mathbf{Q}$, where $\mathbf{M}$ is an appropriate mass matrix, $\mathbf{q}$ is the vector of coordinates, and $\mathbf{Q}$ is a forcing function vector. The second order differential matrix equation $\mathbf{M}\ddot{\mathbf{q}} = \mathbf{Q}$ has a unique solution which can be obtained using standard differential equation or direct method solution techniques. CMS and substructuring methods, in which the coordinate vector $\mathbf{q}$ is expressed in terms of another coordinate vector $\mathbf{p}$ as $\mathbf{q} = \mathbf{B}\mathbf{p}$ where $\mathbf{B}$ is a coordinate transformation matrix, should lead to a solution that converges to this unique solution. This fact can be easily demonstrated by considering the case in which $\mathbf{B}$ is a square and nonsingular transformation. Substituting the transformation $\mathbf{q} = \mathbf{B}\mathbf{p}$ into the original system $\mathbf{M}\ddot{\mathbf{q}} = \mathbf{Q}$ and premultiplying by the inverse (or alternatively in some cases by the transpose) of the transformation $\mathbf{B}$, one obtains $\left(\mathbf{B}^{-1}\mathbf{M}\mathbf{B}\right)\ddot{\mathbf{p}} = \mathbf{B}^{-1}\mathbf{Q}$. Clearly, the similarity transformation $\mathbf{B}^{-1}\mathbf{M}\mathbf{B}$ should not change the solution of the original problem. If

CMS and substructuring techniques are used, $\mathbf{B}$ is no longer a square matrix. Nonetheless the solution obtained by these methods is judged accurate if this solution converges to the solution obtained using the square transformation, a special case of which is to consider $\mathbf{B}$ as an identity matrix.

Conventional structural finite elements used with the *floating frame of reference* (FFR) formulation have rigid body modes. In the FFR formulation, however, the large reference motion is described using Cartesian coordinates and orientation parameters. It is, therefore, necessary to define a unique displacement field by eliminating the rigid body modes of the element shape functions.

In structural mechanics, the boundary conditions are used to define the unique solution of the problem $\mathbf{M}\ddot{\mathbf{q}} = \mathbf{Q}$. These boundary conditions lead to a positive definite stiffness matrix for the problem if the boundary conditions eliminate all the rigid body modes. The boundary conditions, being algebraic constraint equations, eliminate degrees of freedom and lead to well-defined problem that has a unique solution. In the FE/FFR formulation, this is accomplished by using the reference conditions (boundary conditions) which define the nature of the flexible body coordinate system (Agrawal and Shabana, 1985; Shabana, 1996; Shabana, 2013). In addition to defining the body coordinate system, the reference conditions define a problem which has a unique solution regardless of whether or not substructuring techniques such as Craig-Bampton method, is used.

If the FE/FFR formulation is implemented correctly, the implementation should be general to obtain a solution that converges to the unique solution of the problem regardless of which coordinate reduction method is used. As previously mentioned, substructuring methods should

produce a solution that converges to this unique solution. In the case of free-free structure, the use of a combination of static correction and normal modes should not alter the unique solution of the problem.

This fact is particularly important and should not be overlooked when implementing the FFR formulation widely used in the analysis of flexible MBS applications. Overlooking this fact is an indication that the FE/FFR formulation is not fully understood and a lack of understanding this fundamental issue will limit the generality of the FE/FFR implementation as demonstrated in this chapter using a simple example.

CHAPTER 2

GYROSCOPIC MOMENTS

Previously published in (Shabana et al., 2012) and reproduced in this dissertation with permission which is listed in Appendix A. Dr. Martin Hamper is a contributing author.

In vehicle system dynamics, the effect of the gyroscopic moments can be significant during curve negotiations. The absolute angular velocity of the body can be expressed as the sum of two vectors; one vector is due to the curvature of the curve, while the second vector is due to the rate of changes of the angles that define the orientation of the body with respect to a coordinate system that follows the body motion. In this chapter, the configuration of the body in the global coordinate system is defined using the trajectory coordinates in order to examine the effect of the gyroscopic moments in the case of curve negotiations. These coordinates consist of arc length, two relative translations and three relative angles. The relative translations and relative angles are defined with respect to a trajectory coordinate system that follows the motion of the body on the curve. It is shown that when the yaw and roll angles relative to the trajectory coordinate system are constrained and the motion is predominantly rolling, the effect of the gyroscopic moment on the motion becomes negligible, and in the case of pure rolling and zero yaw and roll angles, the generalized gyroscopic moment associated with the system degrees of freedom becomes identically zero. The analysis presented in this chapter sheds light on the danger of using derailment criteria that are not obtained using laws of motion, and therefore, such criteria should not be used in judging the stability of railroad vehicle systems. Furthermore, the analysis presented in this chapter shows that the roll moment which can have a significant effect on the wheel/rail contact forces depends on the forward

velocity in the case of curve negotiations. For this reason, roller rigs that do not allow for the wheelset forward velocity cannot capture these moment components, and therefore, cannot be used in the analysis of curve negotiations. A model of a suspended railroad wheelset is used in this investigation to study the gyroscopic effect during curve negotiations.

2.1 Curve Geometry

In order to develop an expression for the gyroscopic forces when a body, denoted as body i, negotiates a curve, the motion of the body is first described with respect to a *body trajectory coordinate system* $X^{ti}Y^{ti}Z^{ti}$ that follows the body motion. Assuming that the curve geometry is known, the location of the origin and orientation of the body trajectory coordinate system can be defined as a function of one parameter, the curve arc length. In addition to this body trajectory coordinate system, a centroidal body coordinate system $X^{i}Y^{i}Z^{i}$ is introduced as shown in Fig. 2.1.

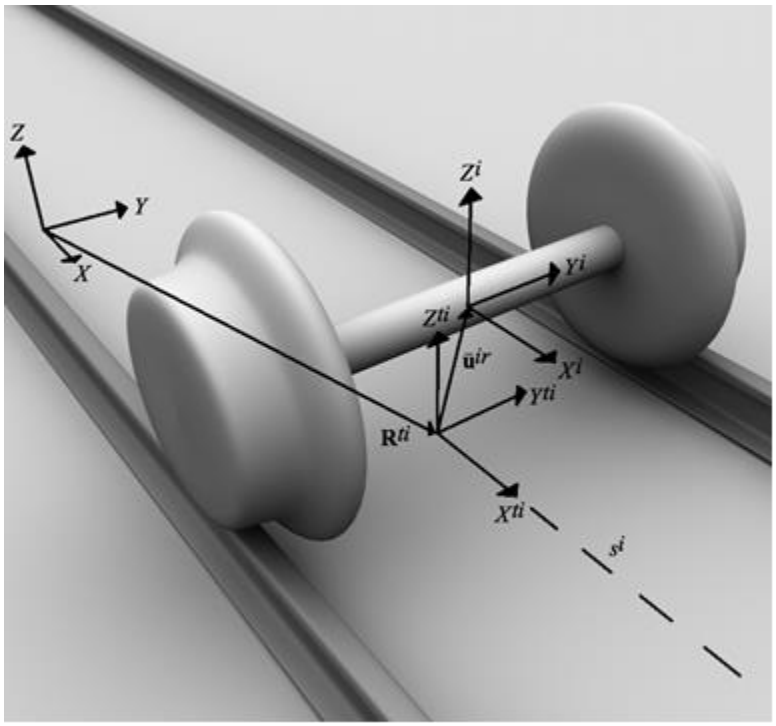

Figure 2.1. Curve Geometry and Body Configuration

The body trajectory coordinate system is selected such that it has no displacement in the longitudinal direction of motion with respect to the body coordinate system. Consequently, one can use two translational coordinates and three angles to completely define the location and orientation of the body coordinate system with respect to the trajectory coordinate system. The sixth coordinate required to define the body configuration in the global coordinate system XYZ is the distance travelled along the curve. This distance is defined by the arc length travelled s^i as shown in Fig. 2.1.

2.1.1 Trajectory Coordinate System

As previously mentioned, the location of the origin of a trajectory coordinate system $X^{ti}Y^{ti}Z^{ti}$ that follows the motion of body i can be uniquely defined in terms of the arc length s^i by the vector $\mathbf{R}^{ti} = \mathbf{R}^{ti}(s^i)$; while the orientation of the trajectory coordinate system $X^{ti}Y^{ti}Z^{ti}$ at this location with respect to the global coordinate system XYZ can be defined using the three Euler angles ψ^{ti}, θ^{ti}, and ϕ^{ti} about the three axes Z^{ti}, $-Y^{ti}$ and $-X^{ti}$, respectively (Shabana et al., 2008). These three Euler angles can be uniquely defined in terms of the arc length s^i, that is, $\psi^{ti} = \psi^{ti}(s^i)$, $\theta^{ti} = \theta^{ti}(s^i)$, and $\phi^{ti} = \phi^{ti}(s^i)$. The transformation matrix, expressed in terms of these Euler angles, that defines the orientation of the trajectory coordinate system $X^{ti}Y^{ti}Z^{ti}$ can be written as follows:

$$\mathbf{A}^{ti} = \begin{bmatrix} \mathbf{i}^{ti} & \mathbf{j}^{ti} & \mathbf{k}^{ti} \end{bmatrix} = \begin{bmatrix} \cos\psi^{ti}\cos\theta^{ti} & -\sin\psi^{ti}\cos\phi^{ti} + \cos\psi^{ti}\sin\theta^{ti}\sin\phi^{ti} & -\sin\psi^{ti}\sin\phi^{ti} - \cos\psi^{ti}\sin\theta^{ti}\cos\phi^{ti} \\ \sin\psi^{ti}\cos\theta^{ti} & \cos\psi^{ti}\cos\phi^{ti} + \sin\psi^{ti}\sin\theta^{ti}\sin\phi^{ti} & \cos\psi^{ti}\sin\phi^{ti} - \sin\psi^{ti}\sin\theta^{ti}\cos\phi^{ti} \\ \sin\theta^{ti} & -\cos\theta^{ti}\sin\phi^{ti} & \cos\theta^{ti}\cos\phi^{ti} \end{bmatrix} \quad (2.1)$$

While the frame defined by this transformation matrix is not necessarily the Frenet frame, both frames share the longitudinal axis X^{ti} and differ by a simple rotation about this axis (Rathod and Shabana, 2006). The sequence of rotation used to develop the transformation matrix of Eq. 2.1 is the sequence used by the railroad industry.

2.1.2 Trajectory Angular Velocity

The angular velocity vector of the trajectory coordinate system $X^{ti}Y^{ti}Z^{ti}$ defined in the global coordinate system can be written in terms of the time derivatives of Euler angles as $\boldsymbol{\omega}^{ti} = \mathbf{G}^{ti}\dot{\boldsymbol{\theta}}^{ti}$, where $\boldsymbol{\theta}^{ti}\left(s^i\right) = [\psi^{ti}\left(s^i\right) \quad \theta^{ti}\left(s^i\right) \quad \phi^{ti}\left(s^i\right)]^T$ and (Shabana et al., 2008)

$$\mathbf{G}^{ti} = \begin{bmatrix} 0 & \sin\psi^{ti} & -\cos\psi^{ti}\cos\theta^{ti} \\ 0 & -\cos\psi^{ti} & -\sin\psi^{ti}\cos\theta^{ti} \\ 1 & 0 & -\sin\theta^{ti} \end{bmatrix} \tag{2.2}$$

Since Euler angles of the trajectory coordinate system are function of s^i only, one has $\dot{\boldsymbol{\theta}}^{ti} = \left(\partial\boldsymbol{\theta}^{ti}/\partial s^i\right)\dot{s}^i = \boldsymbol{\theta}_s^{ti}\dot{s}^i$, where $\boldsymbol{\theta}_s^{ti} = \partial\boldsymbol{\theta}^{ti}/\partial s^i$. It follows that (Shabana et al., 2008)

$$\boldsymbol{\omega}^{ti} = \mathbf{G}^{ti}\boldsymbol{\theta}_s^{ti}\dot{s}^i \tag{2.3}$$

It is clear from this equation that in the case of a tangent track, $\boldsymbol{\theta}_s^{ti} = \mathbf{0}$, and as a consequence, $\boldsymbol{\omega}^{ti} = \mathbf{0}$.

2.2 Body Configuration

The global position vector of the center of mass of body i can be written as

$$\mathbf{R}^i = \mathbf{R}^{ti} + \mathbf{A}^{ti}\bar{\mathbf{u}}^{ir} \tag{2.4}$$

where $\bar{\mathbf{u}}^{ir}$ is the position vector of the center of mass with respect to the origin of the trajectory coordinate system $X^{ti}Y^{ti}Z^{ti}$. This vector can be defined in terms of two-time dependent coordinates as

$$\bar{\mathbf{u}}^{ir} = [0 \quad y^{ir} \quad z^{ir}]^T \tag{2.5}$$

where y^{ir} and z^{ir} are the coordinates of the center of mass of the body in the Y^{ti} and Z^{ti} directions, respectively. The first element of the vector $\bar{\mathbf{u}}^{ir}$ is zero because the trajectory coordinate system $X^{ti}Y^{ti}Z^{ti}$ is selected such that it does not have a displacement with respect to the body coordinate system $X^{i}Y^{i}Z^{i}$ in the longitudinal direction.

2.2.1 Body Orientation

The rotation matrix $\mathbf{A}^{ir}$ that defines the orientation of the centroidal body coordinate system $X^{i}Y^{i}Z^{i}$ with respect to the trajectory coordinate system $X^{ti}Y^{ti}Z^{ti}$ can be expressed in terms of three Euler angles ψ^{ir}, ϕ^{ir}, and θ^{ir} about the Z^{i}, X^{i} and Y^{i} axes. This sequence of Euler angle rotations leads to the following transformation matrix (Shabana et al., 2008):

$$\mathbf{A}^{ir} = \begin{bmatrix} \cos\psi^{ir}\cos\theta^{ir} - \sin\psi^{ir}\sin\phi^{ir}\sin\theta^{ir} & -\sin\psi^{ir}\cos\phi^{ir} & \cos\psi^{ir}\sin\theta^{ir} + \sin\psi^{ir}\sin\phi^{ir}\cos\theta^{ir} \\ \sin\psi^{ir}\cos\theta^{ir} + \cos\psi^{ir}\sin\phi^{ir}\sin\theta^{ir} & \cos\psi^{ir}\cos\phi^{ir} & \sin\psi^{ir}\sin\theta^{ir} - \cos\psi^{ir}\sin\phi^{ir}\cos\theta^{ir} \\ -\cos\phi^{ir}\sin\theta^{ir} & \sin\phi^{ir} & \cos\phi^{ir}\cos\theta^{ir} \end{bmatrix} \tag{2.6}$$

The angles ψ^{ir}, ϕ^{ir}, and θ^{ir} are called the *yaw*, *roll*, and *pitch angles*, respectively. In most railroad vehicle system simulation scenarios, the yaw and roll angles are small, while the pitch angle can be very large due to the wheelset rotation about its axis.

2.2.2 Body Angular Velocity

The absolute angular velocity $\boldsymbol{\omega}^i$ of the body can be written as the sum of two angular velocities; the angular velocity $\boldsymbol{\omega}^{ti}$ of the trajectory coordinate system $X^{ti}Y^{ti}Z^{ti}$, and the angular velocity $\boldsymbol{\omega}^{ir}$ of the body with respect to the trajectory coordinate system. That is, $\boldsymbol{\omega}^i = \boldsymbol{\omega}^{ti} + \boldsymbol{\omega}^{ir}$, where $\boldsymbol{\omega}^{ir} = \mathbf{A}^{ti}\mathbf{G}^{ir}\dot{\boldsymbol{\theta}}^{ir}$, $\boldsymbol{\theta}^{ir} = [\psi^{ir} \quad \phi^{ir} \quad \theta^{ir}]^T$, and

$$\mathbf{G}^{ir} = \begin{bmatrix} 0 & \cos\psi^{ir} & -\sin\psi^{ir}\cos\phi^{ir} \\ 0 & \sin\psi^{ir} & \cos\psi^{ir}\cos\phi^{ir} \\ 1 & 0 & \sin\phi^{ir} \end{bmatrix} \tag{2.7}$$

It follows that

$$\boldsymbol{\omega}^i = \mathbf{G}^{ti}\boldsymbol{\theta}_s^{ti}\dot{s}^i + \mathbf{A}^{ti}\mathbf{G}^{ir}\dot{\boldsymbol{\theta}}^{ir} \tag{2.8}$$

The matrix $\mathbf{G}^{ir}$ becomes singular when $\cos\phi^{ir} = 0$, which corresponds to the case in which the roll angle approaches $\pi/2$. Because the roll angle is small in most railroad vehicle applications, such a singular configuration is not encountered in most simulation scenarios.

2.2.3 Body Trajectory Coordinates

The analysis presented in this section shows that total of six coordinates are required in order to describe the general three-dimensional motion of body i in the global coordinate system XYZ in terms of the generalized trajectory coordinates which are defined as follows:

$$\mathbf{p}^i = [s^i \quad y^{ir} \quad z^{ir} \quad \psi^{ir} \quad \phi^{ir} \quad \theta^{ir}]^T \tag{2.9}$$

Using these trajectory coordinates, the global position vector of an arbitrary point on the body can be written as

$$\mathbf{r}^i = \mathbf{R}^i + \mathbf{A}^i \bar{\mathbf{u}}^i \tag{2.10}$$

where $\mathbf{R}^i = \mathbf{R}^{ti} + \mathbf{A}^{ti}\bar{\mathbf{u}}^{ir}$ is the position vector of the center of mass of body i, $\mathbf{A}^i = \mathbf{A}^{ti}\mathbf{A}^{ir}$ is the rotation matrix that defines the orientation of the body coordinate system with respect to the global coordinate system, and $\bar{\mathbf{u}}^i = [x^i \quad y^i \quad z^i]^T$ is the position vector of the arbitrary point on the body defined in the body coordinate system. Equation 2.10 is, therefore, expressed in terms of the six generalized trajectory coordinates defined by Eq. 2.9 since $\mathbf{R}^{ti} = \mathbf{R}^{ti}(s^i)$, $\mathbf{A}^{ti} = \mathbf{A}^{ti}(s^i)$, $\bar{\mathbf{u}}^{ir} = \bar{\mathbf{u}}^{ir}(y^{ir}, z^{ir})$, and $\mathbf{A}^{ir} = \mathbf{A}^{ir}(\psi^{ir}, \phi^{ir}, \theta^{ir})$.

2.3 Gyroscopic Moments

In order to understand the effect of the gyroscopic moments in the case of curve negotiations, the Newton-Euler equations will be used. In order to obtain a simpler form of the gyroscopic moments in these equations, the absolute angular velocity vector of the body can be defined in the body coordinate system. Using Eq. 2.8 and the fact that $\mathbf{A}^i = \mathbf{A}^{ti}\mathbf{A}^{ir}$, one has

$$\bar{\boldsymbol{\omega}}^i = \mathbf{A}^{iT}\boldsymbol{\omega}^i = \mathbf{A}^{iT}\mathbf{G}^{ti}\boldsymbol{\theta}_s^{ti}\dot{s}^i + \mathbf{A}^{irT}\mathbf{G}^{ir}\dot{\boldsymbol{\theta}}^{ir} \tag{2.11}$$

This definition of the angular velocity will be used to develop a velocity transformation that will shed light on the nature of the gyroscopic moments in the case of curve negotiations. It is clear that the absolute angular velocity vector of Eq. 2.11 can be written as the sum of two vectors; $\mathbf{A}^{iT}\mathbf{G}^{ti}\boldsymbol{\theta}_s^{ti}\dot{s}^i$ and $\mathbf{A}^{irT}\mathbf{G}^{ir}\dot{\boldsymbol{\theta}}^{ir}$. The first vector, $\mathbf{A}^{iT}\mathbf{G}^{ti}\boldsymbol{\theta}_s^{ti}\dot{s}^i$, is the result of the curvature of the curve. In the case of straight line motion (tangent tracks), $\boldsymbol{\theta}_s^{ti} = \mathbf{0}$, and the first vector on the right hand

side of Eq. 2.11 is zero. The second vector, $\mathbf{A}^{irT}\mathbf{G}^{ir}\dot{\boldsymbol{\theta}}^{ir}$, is the result of the change of the orientation of the body with respect to the curve.

The spatial Newton-Euler equations of motion are given as

$$\begin{bmatrix} m^i\mathbf{I} & \mathbf{0} \\ \mathbf{0} & \bar{\mathbf{I}}^i_{\theta\theta} \end{bmatrix} \begin{bmatrix} \ddot{\mathbf{R}}^i \\ \bar{\boldsymbol{\alpha}}^i \end{bmatrix} = \begin{bmatrix} \mathbf{F}^i_e \\ \bar{\mathbf{M}}^i_e - \bar{\boldsymbol{\omega}}^i \times (\bar{\mathbf{I}}^i_{\theta\theta}\bar{\boldsymbol{\omega}}^i) \end{bmatrix} \tag{2.12}$$

where m^i is the mass of the rigid body, $\mathbf{I}$ is a 3×3 identity matrix, $\bar{\mathbf{I}}^i_{\theta\theta}$ is the inertia tensor defined with respect to the centroidal body coordinate system, $\bar{\boldsymbol{\alpha}}^i = \dot{\bar{\boldsymbol{\omega}}}^i$ is the absolute angular acceleration vector defined in the body coordinate system, $\mathbf{F}^i_e$ is the resultant of the external forces defined in the global coordinate system, and $\bar{\mathbf{M}}^i_e$ is the resultant of the external moments defined also in the body coordinate system.

The Cartesian gyroscopic moment defined in the body coordinate system in Eq. 2.12 is the vector $\bar{\boldsymbol{\omega}}^i \times (\bar{\mathbf{I}}^i_{\theta\theta}\bar{\boldsymbol{\omega}}^i)$. One can show that this moment becomes the zero vector in the case of a simple rotation about a fixed axis. This Cartesian gyroscopic moment can be different from zero during curve negotiations even if two angles are constrained. Nonetheless, as will be demonstrated in this chapter, the generalized gyroscopic moment associated with the degree of freedom is zero if the angular velocity can be written in terms of the time rate of one coordinate only.

2.4 Rotation Constraints

Consider the special case of curve negotiation in which the yaw and roll angles ψ^{ir} and ϕ^{ir} remain equal to zero. If these conditions are imposed as algebraic equations, one has

$$\psi^{ir} = 0, \qquad \phi^{ir} = 0 \tag{2.13}$$

In this special case, the matrices $\mathbf{A}^{ir}$ and $\mathbf{G}^{ir}$ reduce to

$$\mathbf{A}^{ir} = \begin{bmatrix} \cos\theta^{ir} & 0 & \sin\theta^{ir} \\ 0 & 1 & 0 \\ -\sin\theta^{ir} & 0 & \cos\theta^{ir} \end{bmatrix}, \quad \mathbf{G}^{ir} = \begin{bmatrix} 0 & 1 & 0 \\ 0 & 0 & 1 \\ 1 & 0 & 0 \end{bmatrix} \tag{2.14}$$

It follows that the second term on the right hand side of Eq. 2.11 reduces to $\mathbf{j}^{i}\dot{\theta}^{ir}$, where $\mathbf{j}^{i}$ is a unit vector along the Y^{i} axis of the body.

2.4.1 Angular Velocity

In the case of the constrained motion considered in this section, the angular velocity vector of Eq. 2.11 can be written as

$$\bar{\boldsymbol{\omega}}^{i} = \mathbf{A}^{iT}\mathbf{G}^{ti}\boldsymbol{\theta}_{s}^{ti}\dot{s}^{i} + \mathbf{j}^{i}\dot{\theta}^{ir} \tag{2.15}$$

This equation shows that in the case in which two relative rotations are constrained when the body negotiates a curve, the angular velocity vector can be written as the sum of two vectors; one vector $\mathbf{A}^{iT}\mathbf{G}^{ti}\boldsymbol{\theta}_{s}^{ti}\dot{s}^{i}$ is due to the curve negotiation, while the other vector $\mathbf{j}^{i}\dot{\theta}^{ir}$ is due to the pitch rotation. While in this case there is a gyroscopic moment, the effect of this gyroscopic moment on the

motion becomes negligible as the body approaches a state of pure rolling. The angular velocity vector of Eq. 2.15 can also be written in the following form:

$$\bar{\boldsymbol{\omega}}^i = \begin{bmatrix} -\sin\theta^{ir} \\ 0 \\ \cos\theta^{ir} \end{bmatrix} \dot{\psi}^{ti} + \begin{bmatrix} 0 \\ 1 \\ 0 \end{bmatrix} \dot{\theta}^{ir} = \begin{bmatrix} -\sin\theta^{ir} & 0 \\ 0 & 1 \\ \cos\theta^{ir} & 0 \end{bmatrix} \begin{bmatrix} \dot{\psi}^{ti} \\ \dot{\theta}^{ir} \end{bmatrix} = \mathbf{H}_2^i \dot{\mathbf{p}}_2^i \tag{2.16}$$

In this equation,

$$\mathbf{H}_2^i = \begin{bmatrix} -\sin\theta^{ir} & 0 \\ 0 & 1 \\ \cos\theta^{ir} & 0 \end{bmatrix}, \qquad \dot{\mathbf{p}}_2^i = \begin{bmatrix} \dot{\psi}^{ti} \\ \dot{\theta}^{ir} \end{bmatrix} \tag{2.17}$$

2.4.2 Cartesian Gyroscopic Moment

One can show in this case of two independent coordinates, ψ^{ti} and θ^{ir}, that the Cartesian gyroscopic moment vector $\bar{\boldsymbol{\omega}}^i \times (\bar{\mathbf{I}}_{\theta\theta}^i \bar{\boldsymbol{\omega}}^i)$ is given by

$$\bar{\boldsymbol{\omega}}^i \times (\bar{\mathbf{I}}_{\theta\theta}^i \bar{\boldsymbol{\omega}}^i) = \begin{bmatrix} \dot{\psi}^{ti}\dot{\theta}^{ir}\left(I_{zz}^i - I_{yy}^i\right)\cos\theta^{ir} \\ \frac{1}{2}\left(\dot{\psi}^{ti}\right)^2\left(I_{zz}^i - I_{xx}^i\right)\sin 2\theta^{ir} \\ \dot{\psi}^{ti}\dot{\theta}^{ir}\left(I_{xx}^i - I_{yy}^i\right)\sin\theta^{ir} \end{bmatrix} \tag{2.18}$$

In deriving this equation, a diagonal inertia tensor is assumed such that

$$\bar{\mathbf{I}}_{\theta\theta}^i = \begin{bmatrix} I_{xx}^i & 0 & 0 \\ 0 & I_{yy}^i & 0 \\ 0 & 0 & I_{zz}^i \end{bmatrix} \tag{2.19}$$

Equation 2.20 defines the vector of Eq. 2.18 in the body trajectory coordinate system. As will be shown later, this expression for the gyroscopic moments simplifies considerably in the case of a uniform disk.

$$\mathbf{A}^{ir}\left(\bar{\boldsymbol{\omega}}^{i}\times(\bar{\mathbf{I}}^{i}_{\theta\theta}\bar{\boldsymbol{\omega}}^{i})\right)=\begin{bmatrix}\dot{\psi}^{ti}\dot{\theta}^{ir}\left(\left(I^{i}_{zz}-I^{i}_{yy}\right)\cos^{2}\theta^{ir}+\left(I^{i}_{xx}-I^{i}_{yy}\right)\sin^{2}\theta^{ir}\right)\\ \frac{1}{2}\left(\dot{\psi}^{ti}\right)^{2}\left(I^{i}_{zz}-I^{i}_{xx}\right)\sin 2\theta^{ir}\\ \frac{1}{2}\dot{\psi}^{ti}\dot{\theta}^{ir}\left(I^{i}_{xx}-I^{i}_{zz}\right)\sin 2\theta^{ir}\end{bmatrix} \tag{2.20}$$

2.4.3 Cartesian and Generalized Gyroscopic Moments

Euler equations of motion can be written as (Eq. 2.12)

$$\bar{\mathbf{I}}^{i}_{\theta\theta}\bar{\boldsymbol{\alpha}}^{i}=\bar{\mathbf{M}}^{i}_{e}-\bar{\boldsymbol{\omega}}^{i}\times(\bar{\mathbf{I}}^{i}_{\theta\theta}\bar{\boldsymbol{\omega}}^{i}) \tag{2.21}$$

Substituting for $\bar{\boldsymbol{\alpha}}^{i}=\mathbf{H}^{i}_{2}\ddot{\mathbf{p}}^{i}_{2}+\dot{\mathbf{H}}^{i}_{2}\dot{\mathbf{p}}^{i}_{2}$ and pre-multiplying by the transpose of $\mathbf{H}^{i}_{2}$, one obtains the following matrix equation that includes two scalar equations:

$$\mathbf{M}^{i}_{2}\ddot{\mathbf{p}}^{i}_{2}=\mathbf{Q}^{i}_{e2}+\mathbf{Q}^{i}_{v2}+\mathbf{Q}^{i}_{g2} \tag{2.22}$$

In this equation,

$$\left.\begin{aligned}&\mathbf{M}^{i}_{2}=\begin{bmatrix}I^{i}_{\psi} & 0\\ 0 & I^{i}_{yy}\end{bmatrix},\quad \mathbf{Q}^{i}_{v2}=\begin{bmatrix}\frac{1}{2}\left(I^{i}_{zz}-I_{xx}\right)\sin 2\theta^{ir}\\ 0\end{bmatrix}\dot{\psi}^{ti}\dot{\theta}^{ir},\\ &\mathbf{Q}^{i}_{e2}=\mathbf{H}^{iT}_{2}\bar{\mathbf{M}}^{i}_{e},\quad \mathbf{Q}^{i}_{g2}=\begin{bmatrix}\frac{1}{2}\dot{\psi}^{ti}\dot{\theta}^{ir}\left(I^{i}_{zz}-I^{i}_{xx}\right)\sin 2\theta^{ir}\\ \frac{1}{2}\left(\dot{\psi}^{ti}\right)^{2}\left(I^{i}_{xx}-I^{i}_{zz}\right)\sin 2\theta^{ir}\end{bmatrix}\end{aligned}\right\} \tag{2.23}$$

In this equation, $I^i_{\psi} = I^i_{xx}\sin^2\theta^{ir} + I^i_{zz}\cos^2\theta^{ir}$, $\mathbf{Q}^i_{v2}$ defines the generalized Coriolis moments associated with the independent coordinates ψ^{ti} and θ^{ir}, and $\mathbf{Q}^i_{g2}$ defines the generalized gyroscopic moments associated with ψ^{ti} and θ^{ir}. It is important to point out that the vector $\mathbf{R}^i$ in Eq. 2.12 can be expressed in terms of the trajectory coordinates as well. This can lead to a different form of the generalized Euler equations, and a different form of the equations of motion. Since the interest in this chapter is on the gyroscopic moments which can be obtained from the information presented in Euler equations, the details of the formulation of the equations of motion in terms of the trajectory coordinates will not be provided in this chapter. These details can be found in previously published work (Shabana et al., 2008).

2.4.4 Uniform Disk

In the special case of uniform disk, $I^i_{xx} = I^i_{zz}$. In this special case, the generalized gyroscopic moment $\mathbf{Q}^i_{g2}$ of Eq. 2.23 is equal to zero, while the Cartesian gyroscopic moment of Eq. 2.18 defined in the disk coordinate system reduces to

$$\bar{\boldsymbol{\omega}}^i \times (\bar{\mathbf{I}}^i_{\theta\theta}\bar{\boldsymbol{\omega}}^i) = \dot{\psi}^{ti}\dot{\theta}^{ir}\begin{bmatrix} \left(I^i_{zz} - I^i_{yy}\right)\cos\theta^{ir} \\ 0 \\ \left(I^i_{xx} - I^i_{yy}\right)\sin\theta^{ir} \end{bmatrix} \tag{2.24}$$

This equation shows that the Y^i component of the Cartesian gyroscopic moment is identically equal to zero.

The gyroscopic moment vector of Eq. 2.20 defined in the trajectory coordinate system reduces to

$$\mathbf{A}^{ir}\left(\bar{\boldsymbol{\omega}}^{i}\times(\bar{\mathbf{I}}^{i}_{\theta\theta}\bar{\boldsymbol{\omega}}^{i})\right)=\dot{\psi}^{ti}\dot{\theta}^{ir}\begin{bmatrix}\left(I^{i}_{xx}-I^{i}_{yy}\right)\\0\\0\end{bmatrix} \tag{2.25}$$

This equation shows that, in the case of constant curvature, pitch angular velocity, and forward velocity; the X^{ti} component of the gyroscopic moment remains constant during curve negotiation, while the Y^{ti} component of the gyroscopic moment is identically zero. This result is expected in the trajectory coordinate system since the angular velocity along the roll axis is assumed to be zero. The rotation about the other two axes produce non-zero gyroscopic moment component along the roll axis. Since the generalized gyroscopic moment is equal to zero, the non-zero gyroscopic roll moment will have an effect only on the constraint moment associated with the roll angle. In railroad vehicle system applications, this roll gyroscopic moment can influence the wheel/rail contact forces, as will be demonstrated by the results presented in the chapter.

2.4.5 Comments on Railroad Derailment Criteria

Some of the derailment criteria used by railroad industry is based on the ratio between the lateral force L and the vertical force V applied to a wheel. The L/V ratio has its root in Nadal's formula. According to these derailment criteria, derailment will not occur if the L/V ratio remains small. The L/V ratio is obtained using a planar transformation of the forces at the contact point, and therefore, it does not take into consideration the effect of the gyroscopic moments. In order to

understand some of the assumptions made when using such a criterion, an example of a wheel is considered. Consider the case in which $\dot{\theta}^{ir} = 39.031$ rad/s, $\dot{s}^{i} = 17.8816$ m/s (64.374 km/h), the radius of curvature of the curve $R = \dot{s}^{i} / \dot{\psi}^{ti} = 349.4$ m, the rolling radius $r = 0.4572$ m, $I^{i}_{xx} = I^{i}_{zz} = 656$ kg.m^2, and $I^{i}_{zz} = 168$ kg.m^2. Using these data, one can show that the non-zero X^{ti} component of the gyroscopic moment is 974.794 N.m. If the speed is doubled (128.748 km/h), one can show that this non-zero component of the gyroscopic moment will be 3899.178 N.m. High speed rail systems operate at much higher speeds, and therefore, further increase in the speed can lead to a significant increase in the gyroscopic roll moment. When approaching pure rolling during curve negotiation (i.e. very small slip rate), there can be situations in which the lateral forces are negligible. Nonetheless, a significant roll gyroscopic moment can be created and can have significant effect on the normal forces. For this reason the use of criteria based on the L/V ratio, which does not take into account the effect of all forces and moments acting on the wheelset, must be carefully examined when high speed rail systems are considered (Shabana, 2012).

2.5 Pure Rolling

Using Eq. 2.23, one can show that in the case of uniform disk, the generalized Coriolis and gyroscopic moments are identically the zero vectors. In this section, it will be shown that in the case of pure rolling, the generalized gyroscopic moment vanishes regardless of whether or not the disk is uniform.

In the case of pure rolling, the forward velocity of the body $\dot{s}^{i}$ is related to the time rate of the pitch angle $\dot{\theta}^{ir}$. In this case, one has the rolling constraint condition $\dot{s}^{i} = \beta \dot{\theta}^{ir}$, where β is

a constant. Substituting this rolling condition into Eq. 2.15, one obtains the following expressions for the angular velocity and angular acceleration:

$$\bar{\boldsymbol{\omega}}^i = \mathbf{H}^i \dot{\theta}^{ir}, \qquad \bar{\boldsymbol{\alpha}}^i = \mathbf{H}^i \ddot{\theta}^{ir} + \dot{\mathbf{H}}^i \dot{\theta}^{ir} \tag{2.26}$$

where $\mathbf{H}^i$ is a velocity transformation matrix that has dimension 3×1, and is defined as

$$\mathbf{H}^i = \mathbf{A}^{iT} \mathbf{G}^{ti} \boldsymbol{\theta}_s^{ti} \beta + \mathbf{j}^i \tag{2.27}$$

The Euler equation of motion is $\bar{\mathbf{I}}_{\theta\theta}^i \bar{\boldsymbol{\alpha}}^i = \bar{\mathbf{M}}_e^i - \bar{\boldsymbol{\omega}}^i \times (\bar{\mathbf{I}}_{\theta\theta}^i \bar{\boldsymbol{\omega}}^i)$ (see Eq. 2.12). Substituting the angular acceleration from Eq. 2.26 into the Euler equation and pre-multiplying by the transpose of the velocity transformation matrix $\mathbf{H}^i$, one obtains the following scalar equation:

$$\left(\mathbf{H}^{iT} \bar{\mathbf{I}}_{\theta\theta}^i \mathbf{H}^i\right) \ddot{\theta}^{ir} = \mathbf{H}^{iT} \left(\bar{\mathbf{M}}_e^i - \bar{\mathbf{I}}_{\theta\theta}^i \dot{\mathbf{H}}^i \dot{\theta}^{ir}\right) - \mathbf{H}^{iT} \left(\bar{\boldsymbol{\omega}}^i \times (\bar{\mathbf{I}}_{\theta\theta}^i \bar{\boldsymbol{\omega}}^i)\right) \tag{2.28}$$

In this equation, the gyroscopic moment vector reduces to the scalar $\mathbf{H}^{iT} \left(\bar{\boldsymbol{\omega}}^i \times (\bar{\mathbf{I}}_{\theta\theta}^i \bar{\boldsymbol{\omega}}^i)\right)$. One can show that this scalar is equal to zero since the angular velocity in this special case of pure rolling becomes a function of the time rate of one variable $\dot{\theta}^{ir}$, and as a consequence, $\mathbf{H}^i$ reduces to a vector. To show that in this case the generalized gyroscopic moment associated with the degree of freedom vanishes, the scalar $\mathbf{H}^{iT} \left(\bar{\boldsymbol{\omega}}^i \times (\bar{\mathbf{I}}_{\theta\theta}^i \bar{\boldsymbol{\omega}}^i)\right)$ can be written using Eq. 2.16 as

$$\mathbf{H}^{iT} \left(\bar{\boldsymbol{\omega}}^i \times (\bar{\mathbf{I}}_{\theta\theta}^i \bar{\boldsymbol{\omega}}^i)\right) = \mathbf{H}^{iT} \left(\mathbf{H}^i \times (\bar{\mathbf{I}}_{\theta\theta}^i \bar{\boldsymbol{\omega}}^i)\right) \dot{\theta}^{ir} = \mathbf{H}^{iT} \tilde{\mathbf{H}}^i (\bar{\mathbf{I}}_{\theta\theta}^i \bar{\boldsymbol{\omega}}^i) \dot{\theta}^{ir} = 0 \tag{2.29}$$

In this equation, $\tilde{\mathbf{H}}^i$ is the skew symmetric matrix associated with the vector $\mathbf{H}^i$ $\left(\tilde{\mathbf{H}}^i \mathbf{H}^i = \mathbf{0}\right)$. Equation 2.29 shows that the generalized gyroscopic moment associated with the degree of freedom vanishes when two angles are constrained and the body experiences pure rolling. This

occurs regardless of whether or not the disk is uniform. If the motion is predominantly rolling with insignificant sliding, the generalized gyroscopic moment associated with the degree of freedom will be negligible. The numerical results presented in following sections will be used to demonstrate this fact.

2.6 Redundant Coordinate Formulation

In this section, a closed form expression for the equations of motion that govern steady state curving of a wheelset is obtained using redundant coordinates which are not totally independent because of the motion kinematic constraints. Such a formulation helps in understanding the direction of the inertia moments in a Cartesian space. The resulting equations will be used to shed light on the significant effect of the gyroscopic and Coriolis roll moments on the wheel/rail contact forces. In the analysis presented in this section, it is assumed that the wheelset travels with a constant forward velocity in order to justify the use of the rotational equations developed.

2.6.1 Motion Constraints and Assumptions

If the roll angle ϕ^{ir} and yaw angle ψ^{ir} with respect to the track are assumed negligible, the transformation matrix that defines the orientation of the wheelset with respect to the track coordinate system can be defined using the transformation matrix $\mathbf{A}^{ir}$ of Eq. 2.14. As previously mentioned, the assumptions of no roll and yaw angles relative to the track must be imposed as kinematic constraints if these two angles are not considered in the formulation of the dynamic

equations. The algebraic equations that define the zero roll and yaw angles are $\phi^{ir} = 0$, and $\psi^{ir} = 0$ (Eq. 2.13).

The relationship between the absolute angular velocity vector $\bar{\boldsymbol{\omega}}^i$ defined in the wheelset coordinate system and the same angular velocity vector $\left(\boldsymbol{\omega}^i\right)^t$ defined in the track coordinate system is $\bar{\boldsymbol{\omega}}^i = \left(\mathbf{A}^{ir}\right)^T \left(\boldsymbol{\omega}^i\right)^t$. The angular acceleration vector $\bar{\boldsymbol{\alpha}}^i$ defined in the wheelset coordinate system can then be expressed in terms of the absolute angular acceleration vector $\left(\boldsymbol{\alpha}^i\right)^t = \begin{bmatrix} \left(\alpha_x\right)^t & \left(\alpha_y\right)^t & \left(\alpha_z\right)^t \end{bmatrix}^T$ defined in the track coordinate system as

$$\bar{\boldsymbol{\alpha}}^i = \left(\mathbf{A}^{ir}\right)^T \left(\boldsymbol{\alpha}^i\right)^t + \left(\dot{\mathbf{A}}^{ir}\right)^T \left(\boldsymbol{\omega}^i\right)^t \tag{2.30}$$

In this equation, $\left(\boldsymbol{\omega}^i\right)^t = \begin{bmatrix} 0 & \dot{\theta}^{ir} & \dot{\psi}^{ti} \end{bmatrix}^T$ is the absolute angular velocity vector defined in the track coordinate system, $\dot{\psi}^{ti} = \dot{s}^i / R$, and R is the radius of curvature of the track space curve. It follows that

$$\left(\dot{\mathbf{A}}^{ir}\right)^T \left(\boldsymbol{\omega}^i\right)^t = -\dot{\theta}^{ir}\dot{\psi}^{ti} \begin{bmatrix} \cos\theta^{ir} \\ 0 \\ \sin\theta^{ir} \end{bmatrix} \tag{2.31}$$

This component of the angular acceleration, which is quadratic in the velocities, must be considered if the equations of motion of the wheelset are written in terms of absolute accelerations defined in the track coordinate system.

2.6.2 Rotational Equations of Motion

In the case of constrained motion, Euler equations can be written as $\bar{\mathbf{I}}^i_{\theta\theta}\bar{\boldsymbol{\alpha}}^i = \bar{\mathbf{M}}^i_e - \bar{\boldsymbol{\omega}}^i \times \left(\bar{\mathbf{I}}^i_{\theta\theta}\bar{\boldsymbol{\omega}}^i\right) + \bar{\mathbf{M}}^i_c$, where $\bar{\mathbf{M}}^i_c$ is the vector of constraint moments resulting from imposing the conditions of zero roll and yaw relative to the track coordinate system. Substituting Eq. 2.30 into Euler equations and premultiplying by $\mathbf{A}^{ir}$, which is the transpose of the velocity transformation matrix of Eq. 2.30, one obtains

$$\left(\mathbf{I}^i_{\theta\theta}\right)^t\left(\boldsymbol{\alpha}^i\right)^t = \left(\mathbf{M}^i\right)^t + \left(\mathbf{M}^i_c\right)^t - \left(\boldsymbol{\omega}^i\right)^t \times \left(\left(\mathbf{I}^i_{\theta\theta}\right)^t\left(\boldsymbol{\omega}^i\right)^t\right) - \mathbf{A}^{ir}\bar{\mathbf{I}}^i_{\theta\theta}\left(\dot{\mathbf{A}}^{ir}\right)^T\left(\boldsymbol{\omega}^i\right)^t \tag{2.32}$$

In this equation, $\left(\mathbf{I}^i_{\theta\theta}\right)^t = \mathbf{A}^{ir}\bar{\mathbf{I}}^i_{\theta\theta}\left(\mathbf{A}^{ir}\right)^T$, and $\left(\mathbf{M}^i\right)^t = \mathbf{A}^{ir}\bar{\mathbf{M}}^i$ and $\left(\mathbf{M}^i_c\right)^t = \mathbf{A}^{ir}\bar{\mathbf{M}}^i_c$ are, respectively, the vectors of resultant and constraint moments defined in the track coordinate system. Because of the wheelset symmetry due to its circular shape, one can show that $\left(\mathbf{I}^i_{\theta\theta}\right)^t = \bar{\mathbf{I}}^i_{\theta\theta}$. Note that the last term in the preceding equation is quadratic in the velocity and it is of the same order as the gyroscopic moment. Note also that the constraint moment vector $\left(\bar{\mathbf{M}}^i_c\right)^t$ is not equal to zero because Eq. 2.32 is expressed in terms of redundant coordinates and not the degrees of freedom. Furthermore, $\ddot{s}^i$ does not appear in the preceding equation since the forward velocity of the wheelset is assumed to be constant. If the forward velocity is not assumed constant, the equations of motion must include inertia coupling between the forward motion and rotations of the wheelset. Using the fact that $I^i_{xx} = I^i_{zz}$, the preceding equation can be written more explicitly as

$$\begin{bmatrix} I^i_{xx}\left(\alpha^i_x\right)^t \\ I^i_{yy}\left(\alpha^i_y\right)^t \\ I^i_{zz}\left(\alpha^i_z\right)^t \end{bmatrix} = \begin{bmatrix} \left(M^i_x\right)^t \\ \left(M^i_y\right)^t \\ \left(M^i_z\right)^t \end{bmatrix} + \begin{bmatrix} \left(M^i_c\right)^t_x \\ \left(M^i_c\right)^t_y \\ \left(M^i_c\right)^t_z \end{bmatrix} - \dot{\theta}^{ir}\dot{\psi}^{ti}\begin{bmatrix} \left(I^i_{zz} - I^i_{yy}\right) \\ 0 \\ 0 \end{bmatrix} + \dot{\theta}^{ir}\dot{\psi}^{ti}\begin{bmatrix} I^i_{xx} \\ 0 \\ 0 \end{bmatrix} \tag{2.33}$$

This equation reduces to Eq. 2.34. These are the equations that govern the rotational motion of the wheelset in terms of absolute accelerations defined in the track coordinate system.

$$\begin{bmatrix} I^i_{xx}\left(\alpha^i_x\right)^t \\ I^i_{yy}\left(\alpha^i_y\right)^t \\ I^i_{zz}\left(\alpha^i_z\right)^t \end{bmatrix} = \begin{bmatrix} \left(M^i_x\right)^t \\ \left(M^i_y\right)^t \\ \left(M^i_z\right)^t \end{bmatrix} + \begin{bmatrix} \left(M^i_c\right)^t_x \\ \left(M^i_c\right)^t_y \\ \left(M^i_c\right)^t_z \end{bmatrix} + \dot{\theta}^{ir}\dot{\psi}^{ti} \begin{bmatrix} I_{yy} \\ 0 \\ 0 \end{bmatrix} \tag{2.34}$$

Note that the last vector on the right side of this equation is the sum of two vectors; the gyroscopic moment vector and the Coriolis moment resulting from the expression of the absolute acceleration defined in the track coordinate system. In the case of unconstrained motion, the equation of motion along the roll axis is $I^i_{xx}\left(\alpha^i_x\right)^t = \left(M^i_x\right)^t + \dot{\theta}^{ir}\dot{\psi}^{ti}I^i_{yy}$. This equation shows that for positive $\dot{\theta}^{ir}$ and $\dot{\psi}^{ti}$, the roll moment $\dot{\theta}^{ir}\dot{\psi}^{ti}I^i_{yy}$ tends to load the outer wheel. The gyroscopic moment defined by the third vector on the right hand side of Eq. 2.33, however, tends to load the inner wheel since I^i_{xx} is always greater than I^i_{yy}. Therefore, ignoring any of the last two vectors on the right hand side of Eq. 2.33 can lead to incorrect wheel/rail forces. Equations 2.33 and 2.34 also show that the quadratic velocity roll moment components are functions of the wheelset forward velocity ($\dot{\psi}^{ti} = \dot{s}^i/R$), and therefore, scaled roller rigs that do not allow for the forward motion of the wheelset will not capture these roll moment components and such roller rigs cannot be used in the analysis of curve negotiations.

2.7 Numerical Simulations

In this section, a model of a suspended wheelset is used to examine the gyroscopic moments during curve negotiations. The gyroscopic moments are obtained using two different simulation models which have different numbers of degrees of freedom. In the first model, the wheelset is assumed to have six degrees of freedom with respect to the track; in this case, no constraints are imposed on the rotations of the wheelset. In the second simulation model, the yaw and roll rotations of the wheelset with respect to the trajectory coordinate system are constrained, leading to a suspended wheelset model that has four degrees of freedom. As previously discussed in this chapter, while two rotations (yaw and roll) are constrained in the four degree of freedom model, the gyroscopic moments are non-zero because of the track curvature and wheelset pitch rotation. In order to examine the gyroscopic effects on the wheelset dynamics and contact forces, an additional simulation scenario is considered; in this scenario the gyroscopic moment is eliminated from the equations of motion. All numerical results presented are obtained using the general purpose multibody system (MBS) computer program SIGMA/SAMS (Shabana, 2010).

2.7.1 Wheelset/Track Model

The suspended wheelset model considered in this section consists of a track, a wheelset, and a frame as shown in Fig. 2.2.

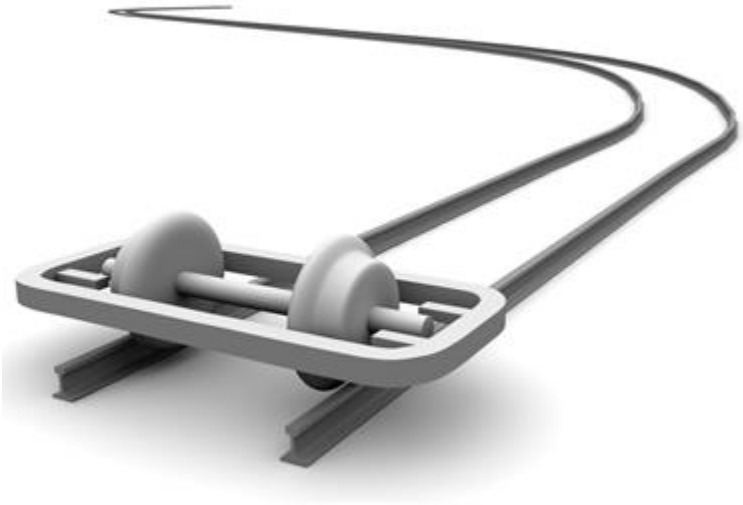

Figure 2.2. Suspended Wheelset/Track Model

The track, which is an *S*-curve, is assumed to be fully constrained during the simulation. The track space curve geometry defined by the data given in Table 2.1 is shown in Fig. 2.3.

Node #	Distance (ft)	Curvature (deg.)	Super-elevation (in)	Grade (%)	Right rail cant angle	Left rail cant angle
1	0	0	0	0	0.025	-0.025
2	200	0	0	0	0.025	-0.025
3	600	3	3	0	0.025	-0.025
4	900	3	3	0	0.025	-0.025
5	1200	0	0	0	0.025	-0.025
6	1600	0	0	0	0.025	-0.025
7	1900	-3	-3	0	0.025	-0.025
8	2200	-3	-3	0	0.025	-0.025
9	2600	0	0	0	0.025	-0.025
10	2800	0	0	0	0.025	-0.025

Table 2.1. Track Parameters

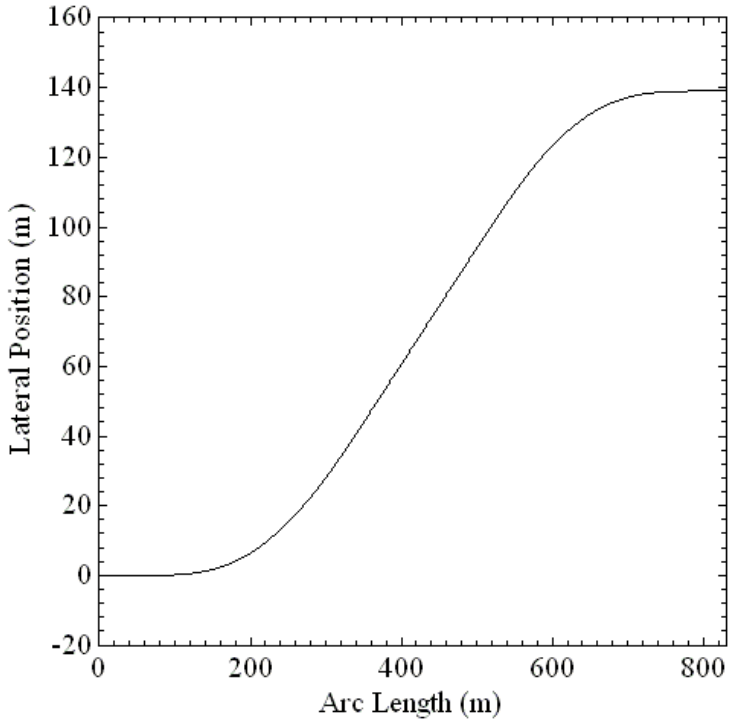

Figure 2.3. Track S-Curve Lateral Position

A small radius of curvature is used in some segments of the track in order to increase the contribution of the forward velocity of the wheelset during curve negotiations to the gyroscopic moments. The wheelset has a mass of 1,568 kg, and has mass moments of inertia of 658, 168, and 658 kg.m^2 about the centroidal body coordinate system axes X^i, Y^i, and Z^i respectively. The wheelset is given an initial velocity $\dot{s}^i = 83$ m/s (185 mph), an initial angular velocity $\dot{\theta}^{ir} = 181.748$ rad/s, and an initial lateral disturbance of 0.5 m/s to initiate the hunting phenomenon (Gilchris, 1998). The frame is connected to the wheelset using four linear spring-damper elements. The frame has a mass of 10,000 kg, a mass moment of inertia about its X and Y axes of 1,799 kg.m^2, and a mass moment of inertia about its Z axis of 2,450 kg.m^2. The first two spring-damper elements

act in the lateral direction and have stiffness coefficients $k_y = 300$ KN/m and zero damping coefficients, while the remaining two spring-damper elements act in the longitudinal direction and have stiffness and damping coefficients $k_x = 162$ KN/m and $c_x = 12$ KN·s/m respectively. The frame is assumed to have a constant forward velocity of $\dot{s}^i = 83$ m/s throughout the simulation. All other degrees of freedom of the frame with respect the track are assumed to be constrained. Therefore, if no other constraints are imposed on the motion of the wheelset and the wheel/rail contact is assumed to be elastic, the model has six degrees of freedom which define a general motion of the wheelset with respect to the track. If the yaw and roll rotations of the wheelset are constrained, the model has four degrees of freedom that define the motion of the wheelset with respect to the track. Because of the track curvature and pitch rotation of the wheelset, the wheelset is also subjected to gyroscopic moments when the four degree of freedom model is used.

2.7.2 Model Results with the Gyroscopic Moment

In the numerical study presented in this section, the gyroscopic moments acting on the wheelset during curve negotiations are evaluated. Imposing rotational constraints on the wheelset has an effect on the gyroscopic moment which is also examined by comparing the results of two different simulation scenarios. In the first scenario no constraints are imposed on the motion of the wheelset, leading to a six degree of freedom model (6-DOF model). In the second simulation scenario, constraints are imposed on the wheelset yaw and roll angles such that $\psi^{ir} = 0$ and $\phi^{ir} = 0$ (4-DOF model). Figures 2.4 and 2.5 show the wheelset lateral displacement and yaw angle when the 6-DOF model is used during curve negotiation.

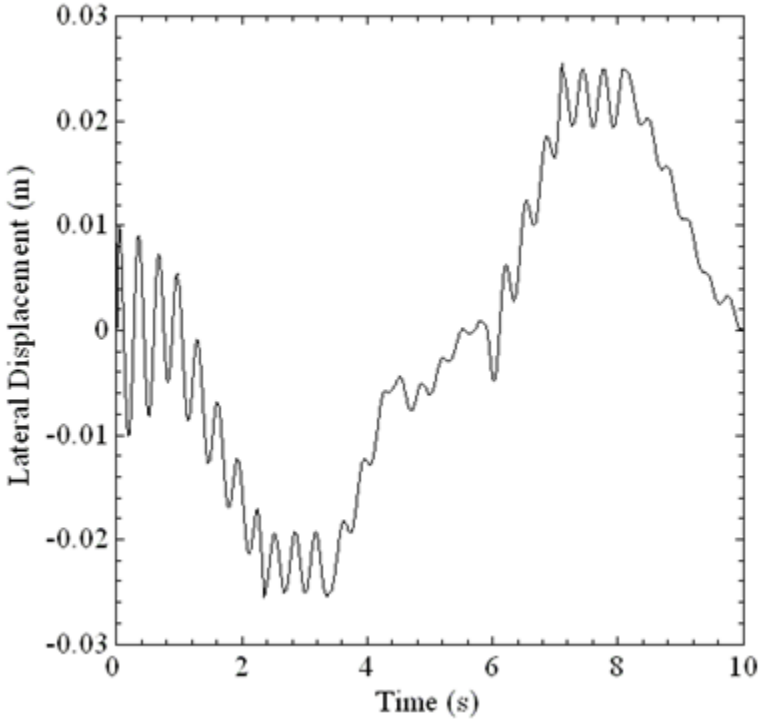

Figure 2.4. Wheelset Lateral Displacement

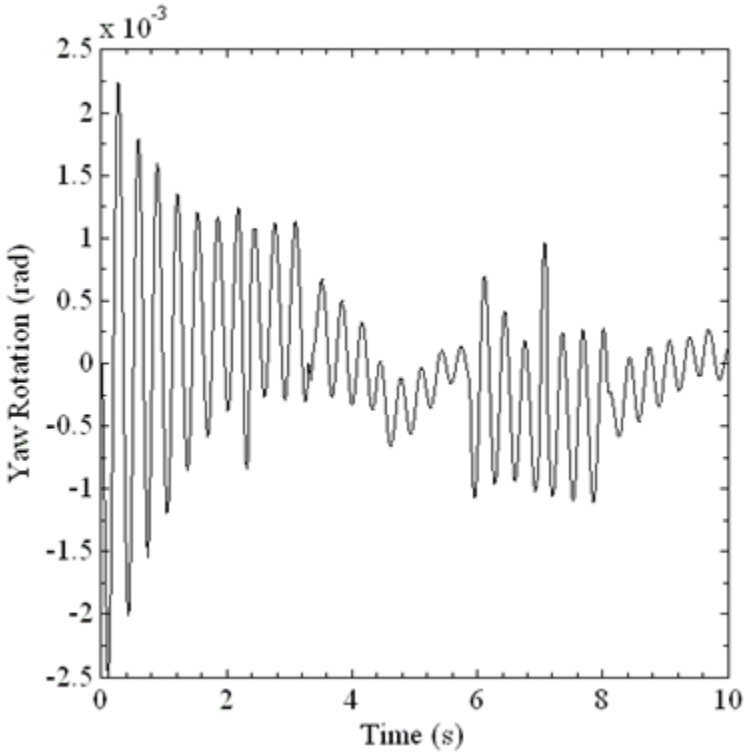

Figure 2.5. Wheelset Yaw Rotation

Figure 2.6 shows the resultant of the forces acting at the center of mass of the wheelset. The components of the resultant force vector shown in this figure are defined in the trajectory coordinate system.

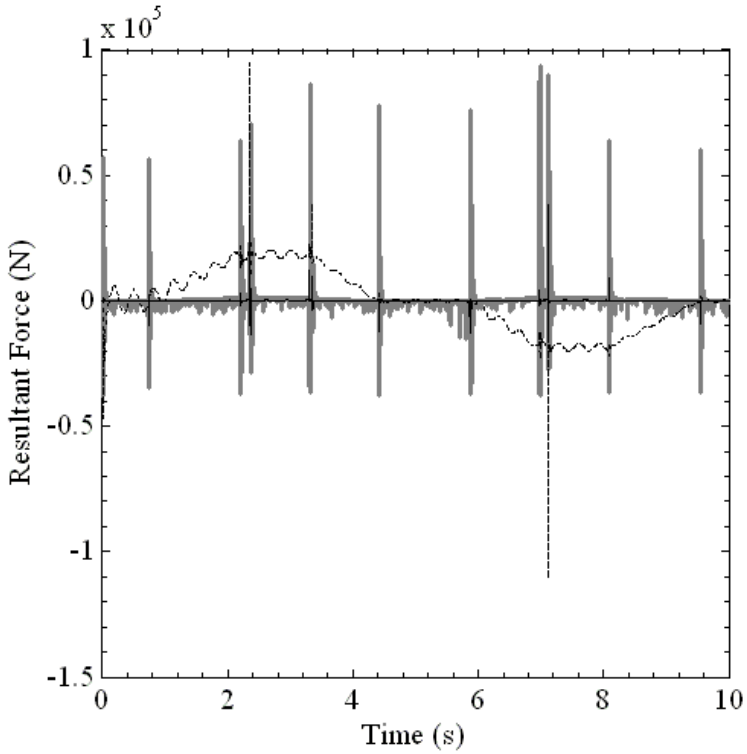

Figure 2.6. Components of the Wheelset Resultant Force Vector

(_____X, - - - - - - Y, _____ Z)

Figure 2.7 shows the components of the resultant moments acting on the wheelset. These components, which are defined in the trajectory coordinate system, include the effect of the contact forces as well as the gyroscopic moments.

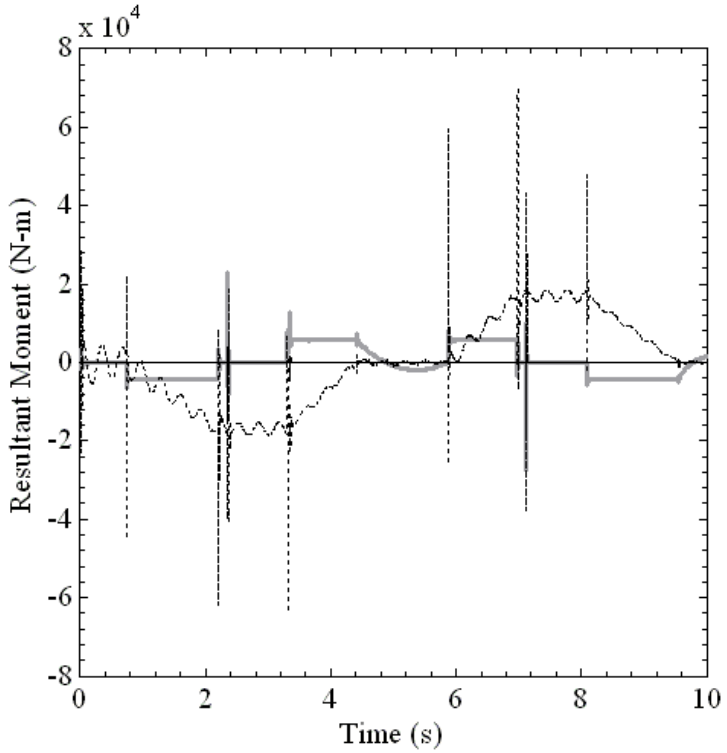

Figure 2.7. Components of the Wheelset Resultant Moments

(- - - - - - X, ——— Y, ——— Z)

Figure 2.8 shows the components of the gyroscopic moments defined in the trajectory coordinate system, while Fig. 2.9 shows the difference between the resultant moments acting on the wheelset and the gyroscopic moments.

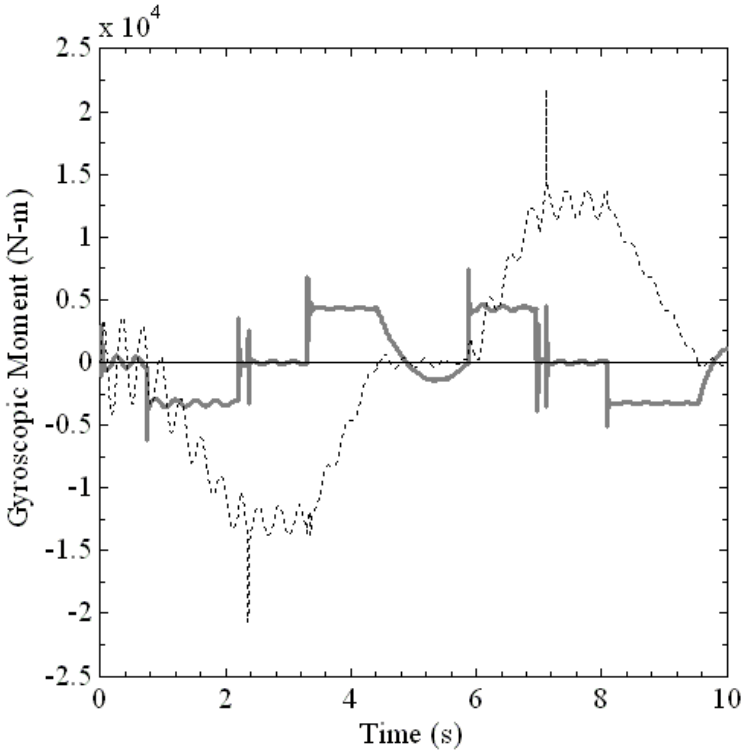

Figure 2.8. Components of the Wheelset Gyroscopic Moments

(- - - - - - X, ——— Y, ——— Z)

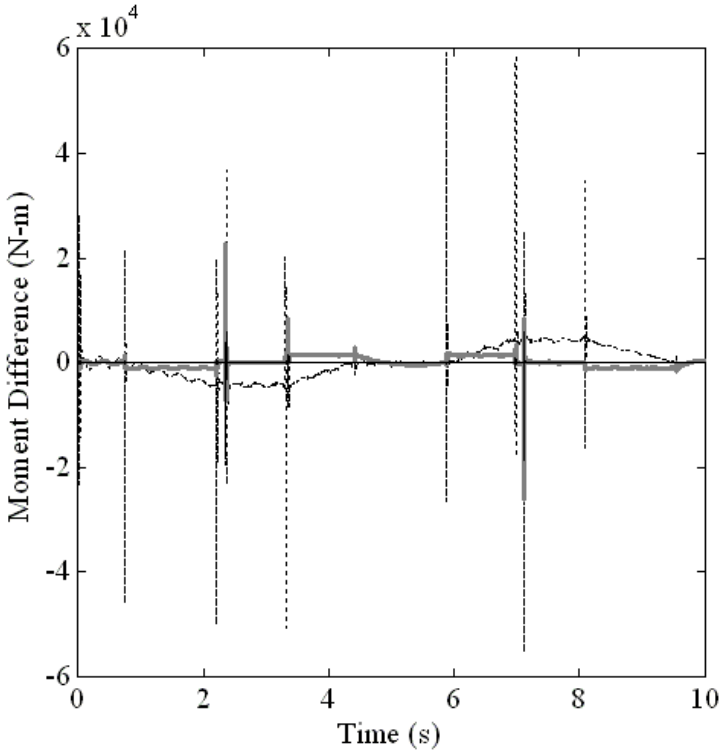

Figure 2.9. Difference between the Wheelset Resultant and Gyroscopic Moments (- - - - - - X, ——— Y, ——— Z)

It should be noted that the spikes in the results presented in these figures occur at the spiral entries and exists. Figure 2.10 shows the magnitude of the gyroscopic moment applied to the wheelset as it negotiates the *S*-curve in the case of the two different simulation scenarios considered in this chapter.

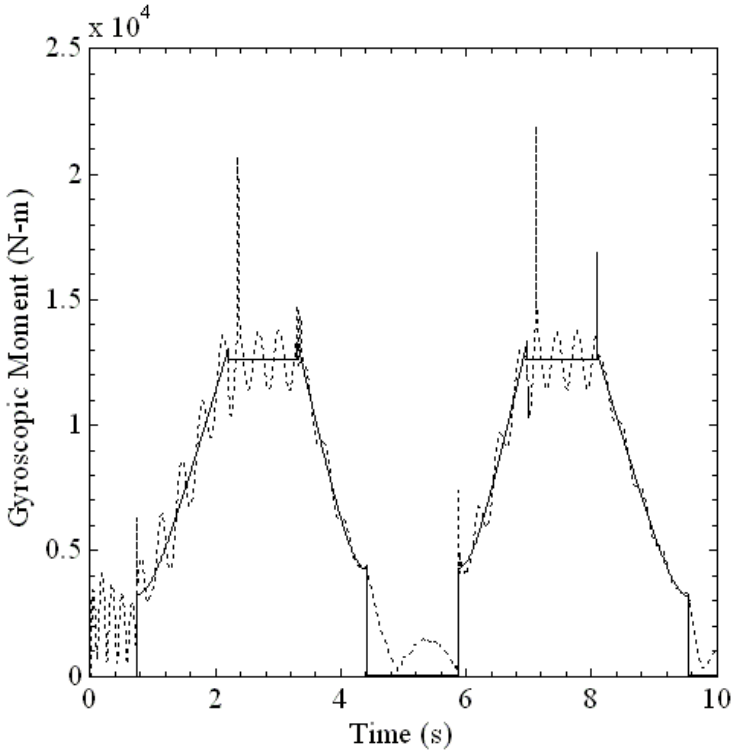

Figure 2.10. Magnitude of the Wheelset Gyroscopic Moment

(_____4-DOF, - - - - - - 6-DOF)

It can be seen that the magnitude of the gyroscopic moment experienced by the wheelset increases for both simulations as the curved sections of track (shown in Fig. 2.3) are negotiated. In the case of the 6-DOF model, the rotations of the wheelset relative to the track are the cause of oscillations in the magnitude of the gyroscopic moment applied to the body. In the case of the 4-DOF model, the yaw and roll rotations are eliminated using the rotational constraints, and therefore, the magnitude of the gyroscopic moment experienced by the wheelset does not have the oscillations that appear in the results of the 6-DOF model.

2.7.3 Gyroscopic Moments and Wheelset Dynamics

In order to examine the effect of the gyroscopic moments on the dynamics of the wheelset, a third simulation model is introduced. In this model, the gyroscopic moment is eliminated from the equations of motion of the six degree of freedom wheelset during the negotiation of the *S*-curve (6-DOF-WG model).

The wheelset lateral displacement with respect to the track is shown in Fig. 2.11 as a function of time for the three simulations.

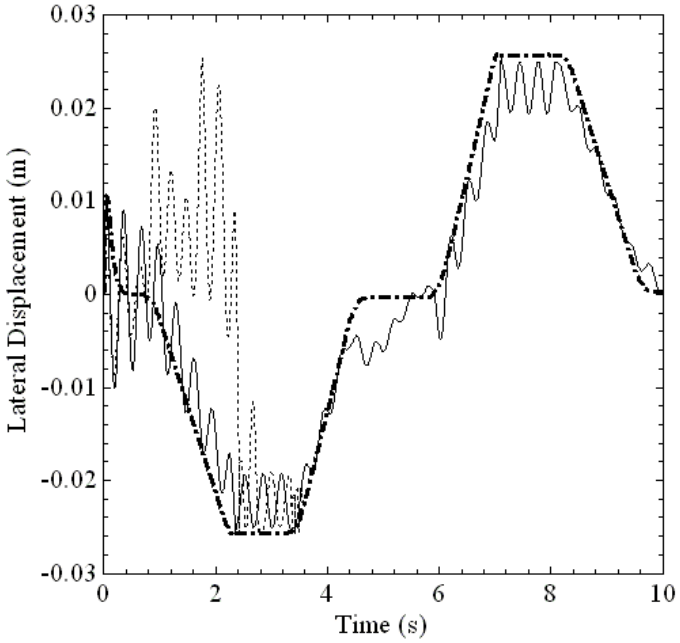

Figure 2.11. Wheelset Lateral Displacement

(_____6-DOF, ___ . ___ 4-DOF, _ _ _ _ _ _ 6-DOF-WG)

When the effect of the gyroscopic moments is neglected (6-DOF-WG model), the wheelset eventually derails demonstrating the significant effect of the gyroscopic moment. Figures 2.12 and 2.13 show a comparison of the normal contact forces for the 6-DOF and 6-DOF-WG models.

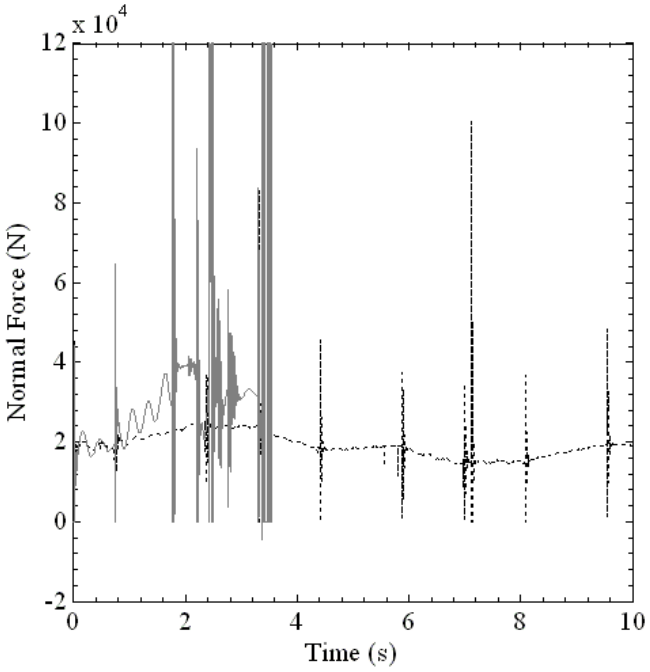

Figure 2.12. Wheelset Normal Forces at Right Contact

(_____6-DOF-WG, - - - - - - 6-DOF)

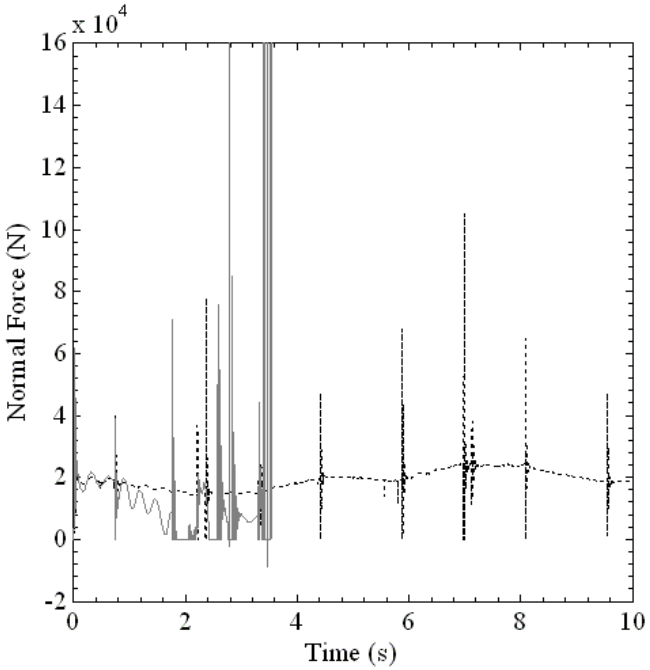

Figure 2.13. Wheelset Normal Forces at Left Contact

(_____6-DOF-WG, - - - - - - 6-DOF)

Eliminating the gyroscopic effect on the wheelset causes the loads on the inner and outer wheels to be different in magnitude from the loads in the case in which the gyroscopic moment is considered. Wheel lift, as the result of wheel unloading, when coupled with lateral instability, can result in a high potential for vehicle derailment (Nishimura, 2009).

2.8 Concluding Remarks

It is shown in this chapter that the generalized gyroscopic moment associated with the degree of freedom of a body can be insignificant in the case of curve negotiation when the yaw and roll angles are constrained and the motion is predominantly rolling. This, however, is not the case in

derailment scenarios where the gyroscopic moments can be significant. As a result, the gyroscopic moments should be considered in developing derailment criteria for railroad vehicle systems. At high speeds, the roll gyroscopic moment can have a significant effect on the normal contact force at the wheels in contact with the rail. In the case of high speeds, all the moments acting on the wheel, including the gyroscopic moment, must be included in the analysis. The analysis presented in this chapter, therefore, sheds light on the assumptions made when using railroad vehicle derailment criteria that are based on the L/V ratio, where L is the lateral force and V is the vertical force acting on the wheel. These derailment criteria are not in general obtained using laws of motion, and therefore, should not be used in judging the stability of railroad vehicle systems.

The analysis presented in this chapter shows that the roll moment which can have a significant effect on the wheel/rail contact forces depends on the forward velocity in the case of curve negotiations. For this reason, roller rigs that do not allow for the wheelset forward velocity cannot be used in the analysis of curve negotiations.

CHAPTER 3

THREE-POINT CONTACT

Previously prepared in (O'Shea and Shabana, 2016) and reproduced in this dissertation with permission which is listed in Appendix A.

In previous research, a set of nonlinear algebraic kinematic constraint equations were developed that describe the configuration of a wheelset in contact with a track at two distinct points. In such a case of two points of contact, a simplified wheelset model that has the lateral displacement and angle of attack (AOA) as the independent variables can be developed. In the current chapter, this approach is extended to the case of a wheelset in contact with a tangent track at three distinct points. The solution of this three-point contact problem requires specifying the wheelset AOA only. This wheelset configuration is significant in derailment investigations because it is a possible configuration at the initiation of a wheel climb derailment. In order to study this wheel climb initiation configuration, a set of nonlinear kinematic constraint equations is developed as a function of the wheelset AOA and solved for the unknown system coordinates and contact surface parameters using an iterative Newton-Raphson algorithm. The wheelset AOA during wheel climb derailments can be determined forensically at the derailment site, making this approach of practical significance. It is shown in this chapter that the system configuration can be fully defined for wheel climb derailment initiation, which allows for the investigation of various derailment parameters such as the wheel/rail contact angle. It is then reinforced in this study that the wheelset flange angle, which is the angle between the tangent to the wheel surface at the contact point and the

wheelset axle, is not representative of the wheel/rail contact angle, which is the angle between the tangent to the contact surfaces and the lateral common tangent to the two railheads; this distinction can only be demonstrated through full definition of the system configuration that accounts for the wheelset roll angle. This chapter therefore calls into question the Nadal L/V derailment limit as well as any investigation that chooses to neglect the wheelset orientation or the effect of such orientation on the wheel/rail contact geometry. This chapter is not intended as a derailment criteria proposal, but rather as support and rationalization for the use of correct contact geometry in derailment investigations. This chapter reiterates the important result that the Nadal L/V derailment limit is not conservative, and demonstrates that, with proper formulation, more accurate and justifiable derailment criteria can be developed.

3.1 Semi-Analytical Analysis

The system considered in this section is a railroad vehicle wheelset in contact with a track section at three distinct points: one point of contact on each wheel tread, and one point of contact on the flange of the right wheel. A three-point contact scenario is a significant case of study and therefore examined in this chapter as it is a configuration at which wheel climb derailments initiate: as the wheel flange makes contact with the rail and the wheel begins to climb, the contact point switches from the wheel tread to the wheel flange. Therefore, at least for an instant, contact is made at three points and can be considered as an initiation configuration of the wheel climb motion. Understanding the wheelset configuration at this critical point in time can assist derailment investigations and produce more applicable derailment criteria. The investigation presented in this

section is three-dimensional. The unconstrained configuration of this two-body system must then be defined using twelve system coordinates which can be written in vector form as

$$\mathbf{q} = \begin{bmatrix} R_x^w & R_y^w & R_z^w & \psi^w & \phi^w & \theta^w & R_x^r & R_y^r & R_z^r & \psi^r & \phi^r & \theta^r \end{bmatrix}^T \tag{3.1}$$

where $\mathbf{R}^i$ is the position vector of the body i reference, and ψ^i, ϕ^i, and θ^i are the three independent rotational coordinates of body i, where $i = w, r$ indicates the wheel and track, respectively. A vector of algebraic kinematic constraint equations that restrict motion and define the system configuration at the position level is formed using the approach outlined in appendix B, which includes fixed-coordinate constraints, contact constraints, and driving constraints (Shabana, 2010). The number of constraint equations imposed on the system is equal to the number of unknown system coordinates $\mathbf{q}$ and system surface parameters $\mathbf{s}$ in order to fully define the system configuration, where the vector $\mathbf{s}$ is written as

$$\mathbf{s} = \begin{bmatrix} \mathbf{s}_1^T & \mathbf{s}_2^T & \mathbf{s}_3^T \end{bmatrix}^T \tag{3.2}$$

where

$$\mathbf{s}_k = \begin{bmatrix} s_1^w & s_2^w & s_1^r & s_2^r \end{bmatrix}_k^T, \quad k = 1,2,3 \tag{3.3}$$

In this equation, k refers to the contact number. The vector of constraint equations can then be solved, using an iterative approach such as the Newton-Raphson algorithm, for the unknown system coordinates and surface parameters. With the system configuration known, parameters such as the wheel/rail contact angle can be investigated.

3.2 System Description

A railroad vehicle wheelset and track are considered in this chapter. A wheelset coordinate system $X^wY^wZ^w$ is rigidly attached to the wheelset center and therefore follows the translation and rotation of the wheelset, as shown in Fig. 3.1.

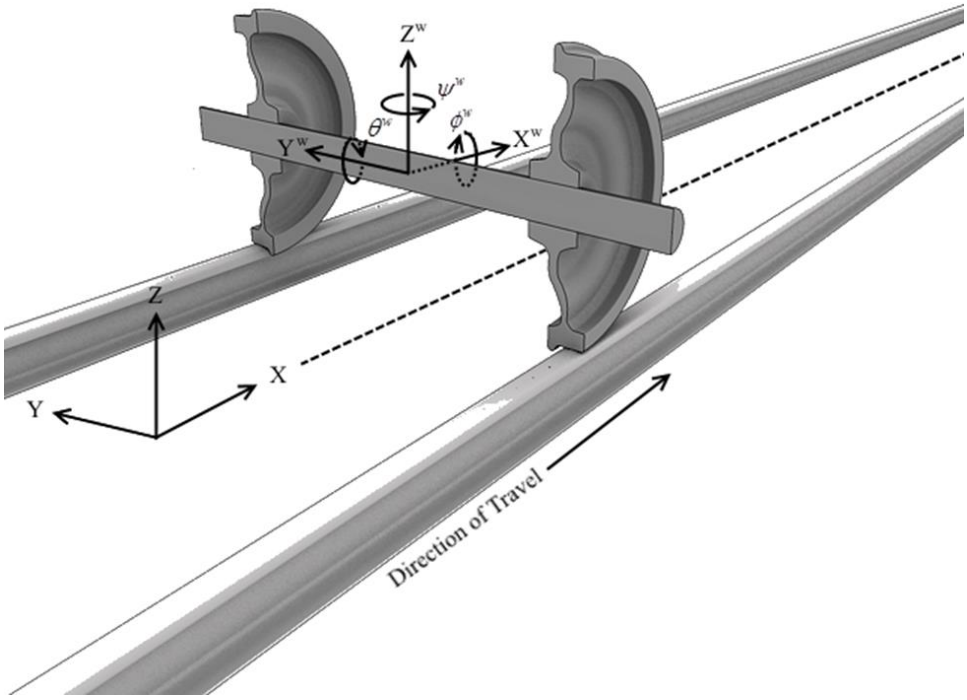

Figure 3.1. Coordinate Systems

The wheel profiles are assumed symmetric and assumed constant through a full revolution about the wheelset axis, and therefore, for this chapter, the location of contact point k on the wheelset surface can be defined, as shown in Fig. 3.2, as

$$\bar{\mathbf{u}}_k^w = \begin{bmatrix} g\left(\left(s_1^w\right)_k\right)\sin\left(s_2^w\right)_k \\ \left(y_0^w\right)_k + \left(s_1^w\right)_k \\ -g\left(\left(s_1^w\right)_k\right)\cos\left(s_2^w\right)_k \end{bmatrix} \tag{3.4}$$

where $g\left(\left(s_1^w\right)_k\right)$ is the wheel profile function shown in Fig. 3.3, and $\left(y_0^w\right)_k$ is the lateral distance of the wheel profile function origin $X^{wp}Y^{wp}Z^{wp}$ from the wheelset center.

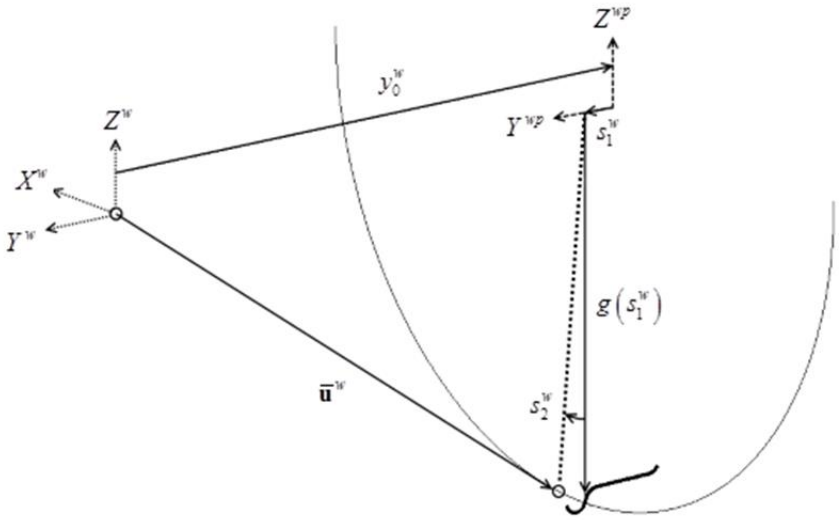

Figure 3.2. Wheel Profile and Surface Description

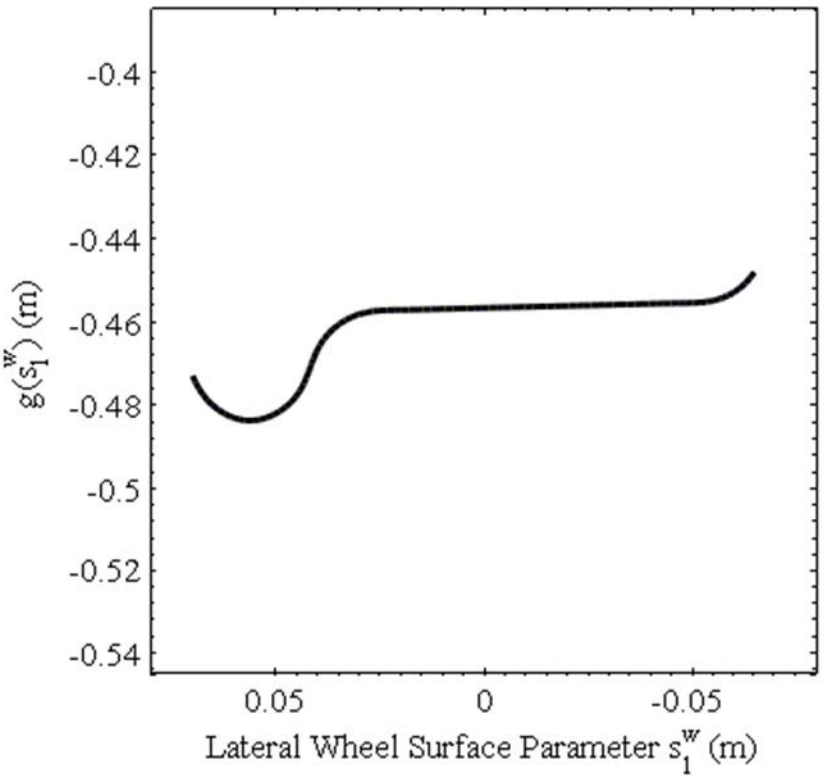

Figure 3.3. Wheel Profile Function

For the wheelset used in this chapter, $\left(y_0^w\right)_k = \pm 0.74$ m.

The track used in this chapter is a straight track. A track coordinate system $X^r Y^r Z^r$, rigidly attached to the track centerline, has the same position and orientation as the global reference frame XYZ, shown in Fig. 3.1. The rail profiles are assumed symmetric and constant along the length of the track, and therefore the location of contact point k on the track surface can be defined, as shown in Fig. 3.4, as

$$\bar{\mathbf{u}}_k^r = \begin{bmatrix} \left(s_1^r\right)_k \\ \left(y_0^r\right)_k + \left(s_2^r\right)_k \cos\gamma_k - f\left(\left(s_2^r\right)_k\right)\sin\gamma_k \\ \left(s_2^r\right)_k \sin\gamma_k + f\left(\left(s_2^r\right)_k\right)\cos\gamma_k \end{bmatrix} \tag{3.5}$$

where $f\left(\left(s_2^r\right)_k\right)$ is the rail profile function shown in Fig. 3.5, $\left(y_0^r\right)_k$ is the lateral distance of the rail profile function origin $X^{rp}Y^{rp}Z^{rp}$ from the track centerline, and γ_k is the inclination of the rails in the direction of the track center.

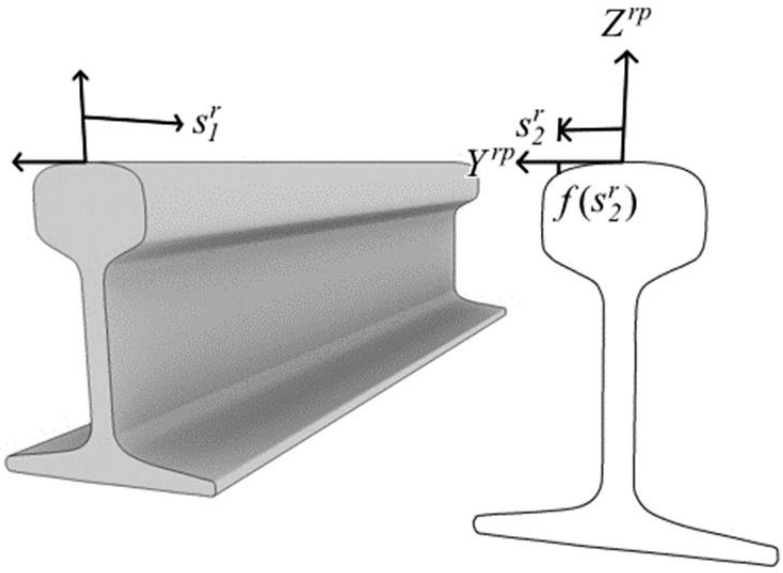

Figure 3.4. Rail Profile and Surface Description

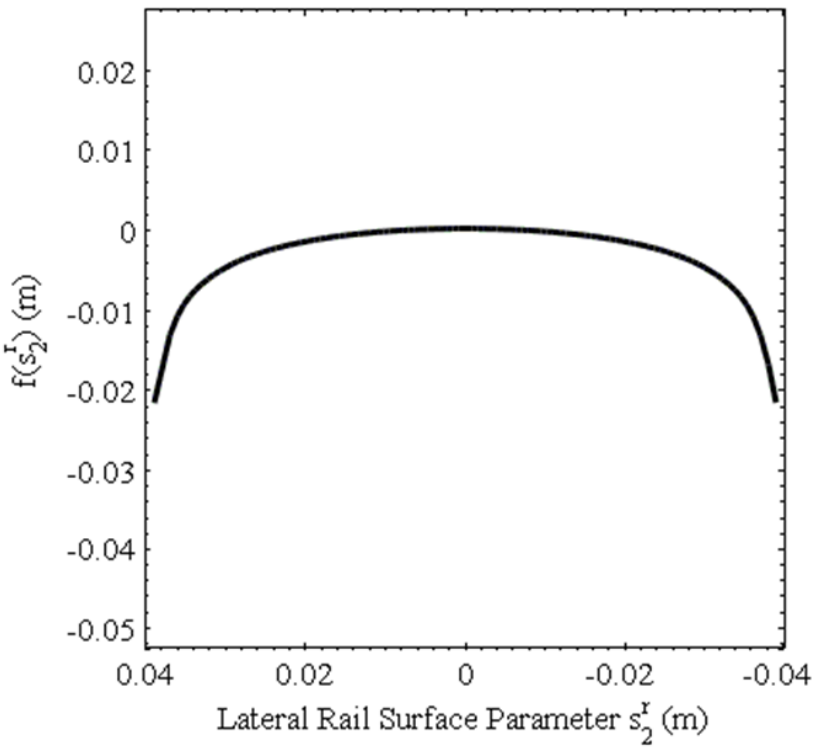

Figure 3.5. Rail Profile Function

For this chapter, it is assumed that $\left(y_0^r\right)_k = \pm 0.75565\,\text{m}$ and $\gamma_k = \pm 25\,\text{mrad}$.

The wheelset and track are considered rigid in this chapter, and therefore, the penetration of the surfaces of the two bodies is not allowed. On the other hand, it is assumed that the wheelset remains in contact with the track at three distinct points, and therefore, separation of the wheelset from the track at any of these points is not allowed either. This configuration is a possible wheel

climb initiation configuration that exists at least for an instant. Finally, the track is assumed fixed in space, and therefore, the system has three degrees of freedom that can be specified in order to fully define the configuration of the system. In this chapter, the longitudinal wheelset position, the wheelset AOA, and the wheelset pitch rotation are selected as these driving variables. For a tangent track section, with constant rail profiles, the wheelset longitudinal position may be set to a constant or zero, for simplicity, without loss of generality. Additionally, for a symmetric wheelset without surface deformations, the wheelset pitch rotation may also be set to a constant or zero, for simplicity, without loss of generality. Therefore the system configuration in this chapter is driven by the wheelset AOA.

3.3 Lead/Lag Contact

When resting at a neutral position on a section of tangent track, the wheelset will contact the track at one point on each wheel tread; these contact points are located in-plane with the wheelset axis. When the wheelset is shifted laterally, a displacement that leads to a flange contact with the rail, the wheelset must undergo a roll rotation, which is defined as a rotation about the forward axis of the wheelset, due to the slight taper of the wheel tread sections: the rolling radius of the flanging wheel will increase and the rolling radius of the other wheel will decrease. The three contact points, however, will still be located in-plane with the wheelset axis: this configuration refers to the case of zero AOA. As the wheelset is rotated to some AOA, while maintaining three points of contact with the track, a *lead-lag* contact scenario is encountered: the contact points are now located in front of and behind the wheelset axis, with respect to the wheelset coordinate system. The contact geometry at such orientation is significantly different than the case of zero AOA and therefore

must be considered. The forward shift of the flange contact point versus the wheelset AOA is shown in Fig 3.6, including a side-view of the wheel as reference.

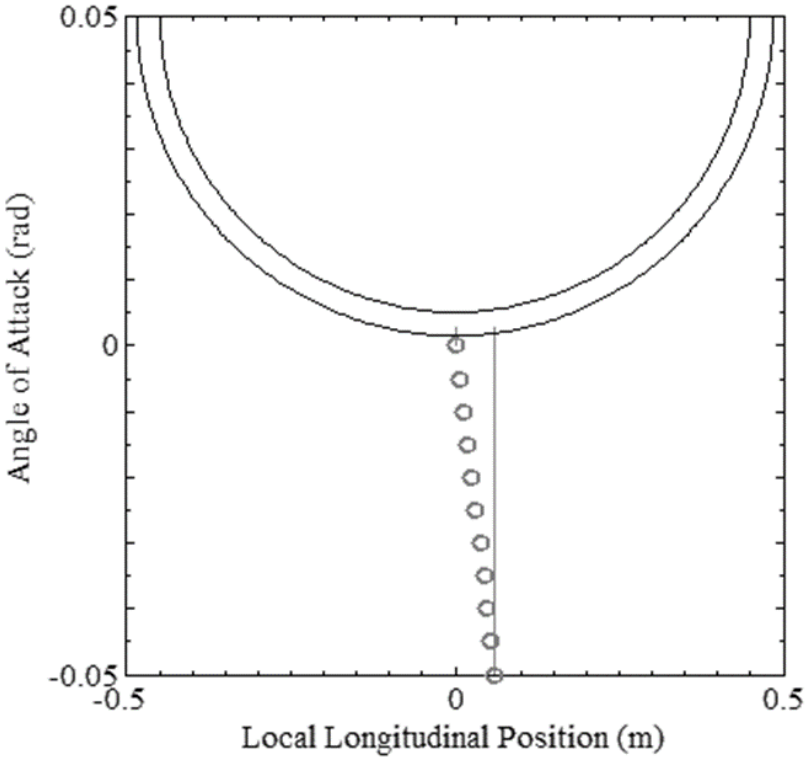

Figure 3.6. Lead Contact on Wheel Flange

In addition to the flange contact point moving forward with respect to the wheelset axis, the contact point will also move downward along the flange profile towards the tip of the flange as well. This

phenomenon is also shown as a function of the wheelset AOA in Fig. 3.7, where the wheel profile is also shown for reference.

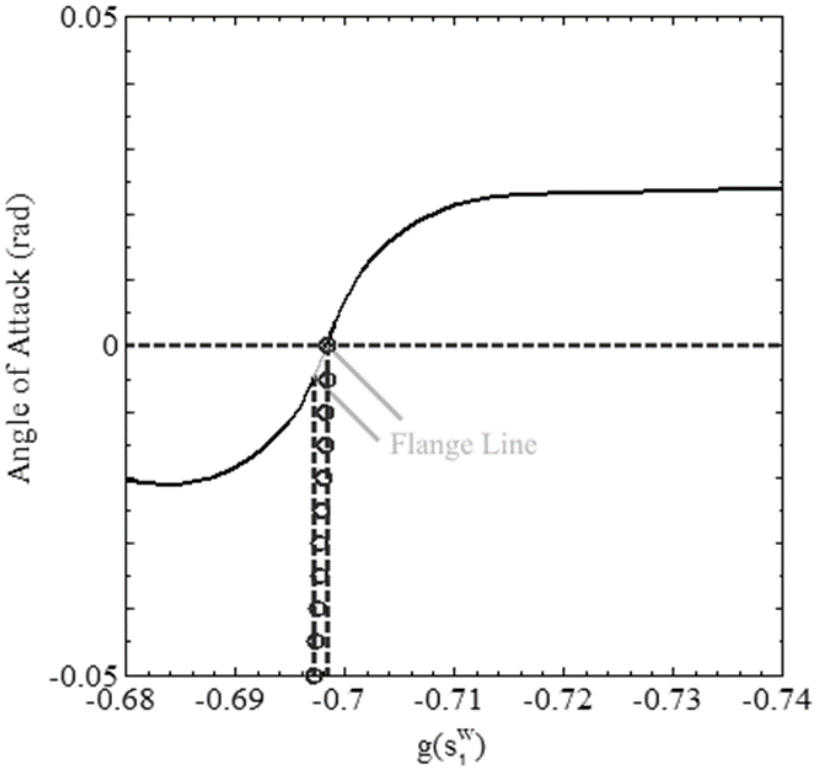

Figure 3.7. Downward Movement of Flange Contact Point

3.4 Wheel Climb Flange Line

By rotating the wheelset through a large AOA, it is possible to define a *wheel climb flange line*, or the length along the wheel flange profile that contains the set of possible contact point locations at

climb initiation. This flange line, through an AOA of 50 mrad, is shown in Fig. 3.7. It has been a common practice to use the steepest point of the wheel flange to calculate a flange angle to be used as input to the Nadal L/V derailment limit. This figure indicates that, if the slope of the flange is not constant along the flange line, then the steepest point on the wheel flange will not be representative of the actual flange angle at the point of contact for some wheelset configuration. It is therefore recommended that, during derailment investigations, the wheelset configuration is fully defined at climb initiation to understand the proper contact geometry.

3.5 Flange- versus Contact-Angle

It is shown in section 3.4 that the flange will contact the rail at different points on the wheel flange profile depending on the orientation of the wheelset with respect to the track, the geometry of the wheel and rail profiles, and the AOA of the wheelset. As the profile contact points vary with the movement of the contact point, the slope of the flange profile at the contact point will also change with the movement of the contact point. Using Eq. 3.4, the wheel lateral tangent associated with the lateral surface parameter s_1^w may be defined in the wheelset coordinate system as

$$\bar{\mathbf{t}}_1^w = \partial \bar{\mathbf{u}}^w / \partial s_1^w = \left[g'\left(s_1^w\right)\sin s_2^w \quad 1 \quad -g'\left(s_1^w\right)\cos s_2^w \right]^T \tag{3.6}$$

where $g'\left(s_1^w\right) = \partial g\left(s_1^w\right)/\partial s_1^w$. When the wheelset is oriented with zero AOA, the point of contact lies in a vertical plane with the wheelset axis, and therefore at such orientation, one can assume $s_2^w = 0$ if the effect of the pitch rotation is not considered. For this configuration, the vector $\bar{\mathbf{t}}_1^w$ simplifies to

$$\bar{\mathbf{t}}_1^w = \partial \bar{\mathbf{u}}^w / \partial s_1^w = \left[0 \quad 1 \quad -g'\left(s_1^w\right) \right]^T \tag{3.7}$$

The *flange angle* $\bar{\delta}$ is then defined as shown in Fig. 3.8.

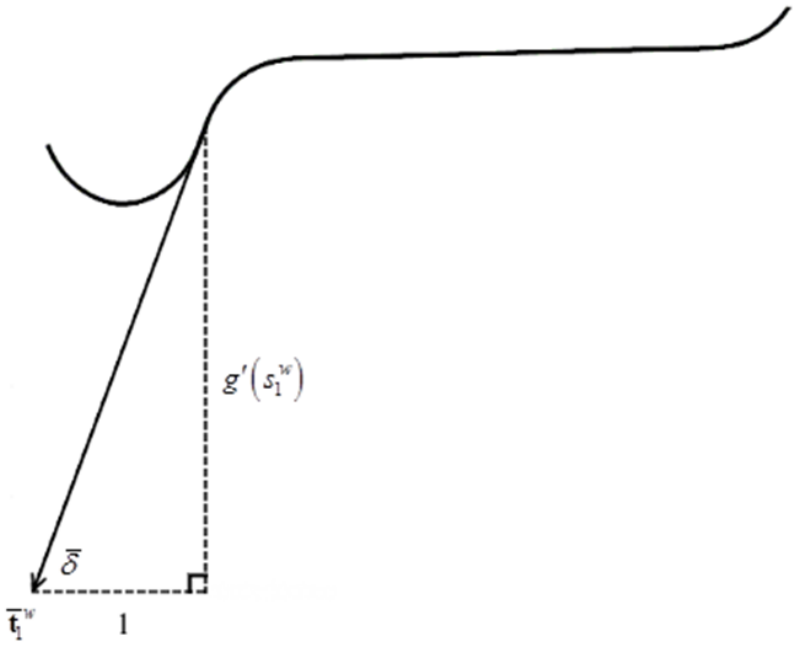

Figure 3.8. First Tangent at the Wheel Flange Contact Point

Once the system configuration is known, the flange angle at the climb initiation can be calculated. For the system considered in this chapter, for an AOA through 50 mrad, the wheelset flange angle at climb initiation is shown in Fig. 3.9.

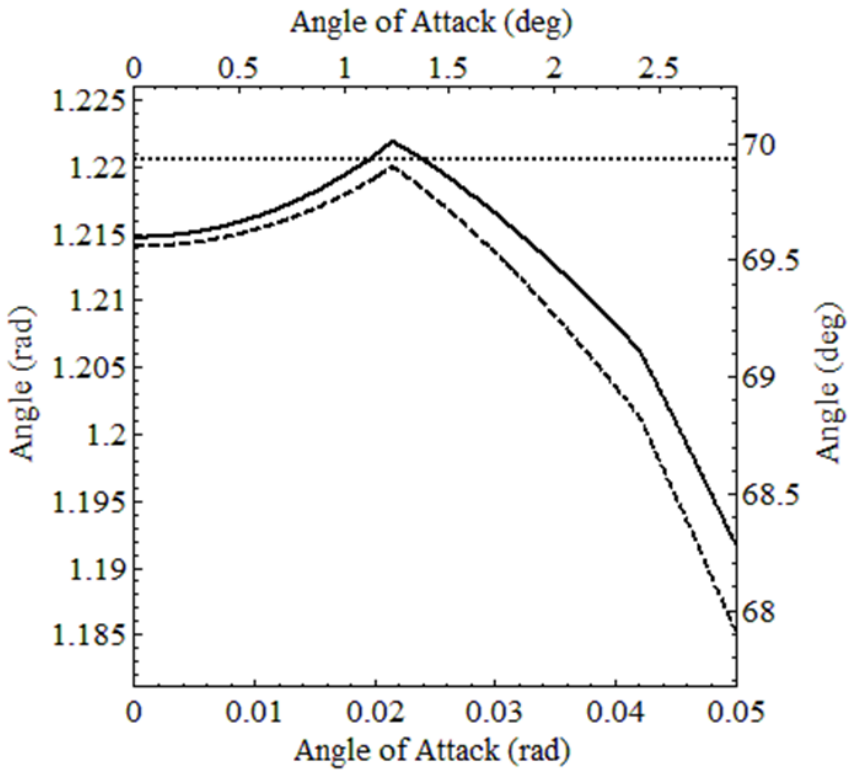

Figure 3.9. Flange and Contact Angles vs. Wheelset Angle of Attack

(_____Contact Angle, - - - - - -Flange Angle, ... Maximum Flange Angle)

Nadal's derivation did not account for any wheelset orientation, including roll, and therefore the single wheel considered in Nadal's analysis is assumed to have the same orientation as the track. As a consequence, the wheelset axle and the lateral common tangent to the railhead centers are parallel. In this specific case, the flange and contact angles are identical, justifying the use of the flange angle by Nadal. However, wheel climb derailments are more likely to occur at an AOA; additionally, the case of no wheelset orientation during flange contact will most likely result in a loss of contact at the guided wheel. In order to capture the physical phenomenon of wheel climb, a *contact angle*, which defines the angle between the vector tangent to the contact surfaces at the point of contact and the lateral common tangent to the two railhead centers, must be considered. Taking into account the wheelset yaw ψ^w and roll ϕ^w, the orientation of the wheelset coordinate system, excluding the effect of the pitch rotation, may be written as

$$\mathbf{A}^w = \begin{bmatrix} \cos\psi^w & -\sin\psi^w\cos\phi^w & \sin\psi^w\sin\phi^w \\ \sin\psi^w & \cos\psi^w\cos\phi^w & -\cos\psi^w\sin\phi^w \\ 0 & \sin\phi^w & \cos\phi^w \end{bmatrix} \tag{3.8}$$

The tangent vector $\bar{\mathbf{t}}_1^w$ can be defined in the same coordinate system as the track through the transformation

$$\mathbf{t}_1^w = \left(\mathbf{A}^r\right)^T \mathbf{A}^w \bar{\mathbf{t}}_1^w = \begin{bmatrix} -\sin\psi^w\cos\phi^w + \cos\psi^w g'\left(s_1^w\right)\sin s_2^w - \sin\psi^w\sin\phi^w g'\left(s_1^w\right)\cos s_2^w \\ \cos\psi^w\cos\phi^w + \sin\psi^w g'\left(s_1^w\right)\sin s_2^w + \cos\psi^w\sin\phi^w g'\left(s_1^w\right)\cos s_2^w \\ \sin\phi^w - \cos\phi^w g'\left(s_1^w\right)\cos s_2^w \end{bmatrix} \tag{3.9}$$

where $\mathbf{A}^r$, for this chapter, is the identity matrix. The contact angle, defined in the same coordinate system as the track, is then written as

$$\delta = \arctan\left(\frac{\sin\phi^w - \cos\phi^w g'\left(s_1^w\right)\cos s_2^w}{\cos\psi^w \cos\phi^w + \sin\psi^w g'\left(s_1^w\right)\sin s_2^w + \cos\psi^w \sin\phi^w g'\left(s_1^w\right)\cos s_2^w} \right) \tag{3.10}$$

which takes into account the wheelset orientation as well as the forward movement of the contact point. The contact angle in this chapter is shown in Fig. 3.9 and is compared against the flange angle for angles of attack through 50 mrad. In the case of zero AOA, the difference between the flange and contact angles is the result of the roll rotation of the wheelset; the contact angle is steeper as a result of the rotation of the wheelset and consequently the wheel profile. As the AOA increases, so does the difference between the flange angle and contact angles; the wheelset orientation as well as the movement of the contact point now both contribute to this difference. Nonetheless, it is clear from the figure that the flange angle is not an accurate description of the angle that must be used in derailment investigations, and that the contact angle should be used instead.

3.6 Comments on Derailment Analysis

As mentioned earlier, numerous investigations use the steepest section of the wheel flange profile in order to calculate the flange angle to be used as input in the Nadal L/V derailment limit. The maximum flange angle for the wheel profile used in this chapter is shown for reference in Fig. 3.9. It is seen from the figure that the steepest portion of the wheel flange is never actually in contact with the rail at climb initiation. Additionally, for the profile used, this flange angle is only representative of the actual contact angle for two values of the AOA, approximately 19.6 mrad and 23.9 mrad. It is clear then, from these statements, that this practice is not justified for an accurate derailment analysis.

3.7 Concluding Remarks

The Nadal L/V derailment limit, along with subsequent derailment criteria, is developed in order to evaluate the proneness of a wheelset to a wheel climb derailment. Wheel climb derailments can initiate when the wheelset is in contact with the track at three distinct points. The formulation presented in this chapter demonstrates that the configuration of a wheelset in contact with a tangent track at three distinct points can be fully defined for a given AOA. It has been recently noted in the literature that the orientation of the wheelset at climb initiation, as well as the consequences of such orientation on the wheel/rail contact geometry, plays a significant role in the derailment. Because the system configuration is fully defined using the presented formulation, derailment parameters such as the wheel/rail contact angle can be solved for; this angle is compared against the wheelset flange angle for various angles of attack to enforce that a distinction must be made between the two values. Additionally, it is shown that the steepest point on the wheel flange is not necessarily in contact with the rail due to the orientation of the wheelset, and therefore, this point on the wheel profile should not be used in contact angle calculations by default. These results then raise concern with regards to the Nadal L/V derailment limit, which is a planar force balance and does not take into account the orientation of the wheelset. Additional concern is raised with regards to the practice of using the steepest section of the wheel flange to calculate the flange angle, which is then used as input to the Nadal calculation.

The results of the formulation indicate the need for using the correct contact geometry in the investigations of the derailments of modern railroad systems.

CHAPTER 4

WHEEL CLIMB

Previously published in (O'Shea and Shabana, 2015) and reproduced in this dissertation with permission which is listed in Appendix A. Parts previously prepared in (O'Shea and Shabana, 2016) and reproduced in this dissertation with permission which is listed in Appendix A.

A fully nonlinear unconstrained multibody system (MBS) wheel climb derailment model is developed to analyze the forces that govern the wheel climb motion when oriented at a large angle of attack (AOA). The results of the MBS model in the vicinity of the *climb initiation* are verified using a semi-analytical model that makes use of simplifying assumptions derived from the current interpretation of wheel climb. It is shown that, when the wheel makes flange contact with the rail at a large AOA, the lateral and vertical displacements of the wheel become coupled due to motion constraints resulting from the wheel/rail contact. This constraint produces kinematic contributions to the wheel climb motion that are shown to be significant throughout the motion. Additionally, the friction force developed at the point of contact is shown to be three-dimensional and therefore concerns are raised regarding the validity of any planar force balance at the point of contact to capture such motion. Regardless, the forces measured at contact point are shown to not represent the forces that drive the derailment. Most importantly, however, is that the *Nadal* L/V Limit is shown to not be conservative in the case considered in this chapter.

Finally, the MBS wheel climb derailment model is used to validate and support the formulation described in chapter 3. Using this model, it is seen that the initiation of the wheel climb motion is correctly predicted using proper geometry definitions in the derailment criteria,

whereas such motion was not correctly predicted using the geometry definitions used by Nadal. This finding is not intended as a derailment criteria proposal, but rather as support and rationalization for the use of correct contact geometry in derailment investigations. Taking these important results into account, questions must be raised regarding the current interpretation of wheel climb, which does not account for kinematics, as well as the various derailment criteria that have roots in Nadal's derivation.

4.1 MBS Derailment Model

In this section, a new three-dimensional fully nonlinear unconstrained MBS model is developed using the software SIGMA/SAMS (Shabana, 2010). The results of the general unconstrained MBS wheelset/track model are discussed in order to shed light on the key aspects of the wheel climb motion. The model presented is three-dimensional, places no constraints on the motion of the wheelset, and uses an elastic contact approach that takes into account the full wheel/rail profiles. The results demonstrate that the lateral and vertical motion of the wheels are coupled due to contact with the track, that wheel climb derailments occurring at a large AOA must be studied in three dimensions, and that the climb mechanism has kinetic and kinematic contributions. The example provided in this section ultimately acts as a three-dimensional MBS counter-example to the use of the Nadal L/V Limit in derailment investigations, indicating that the L/V Limit is not a conservative criterion for all cases.

4.1.1 Wheelset/Track Model

The model presented in this section is three-dimensional and consists of two rigid bodies: a wheelset and a straight track that comprises of two rails. The wheelset is given a centroidal body coordinate system (CBCS) $X^wY^wZ^w$, shown in Fig. 4.1, that is fixed to the wheelset center of mass and follows the translations and rotations of the wheelset. The CBCS motion is defined with respect to an inertial reference frame XYZ, also shown in Fig. 4.1.

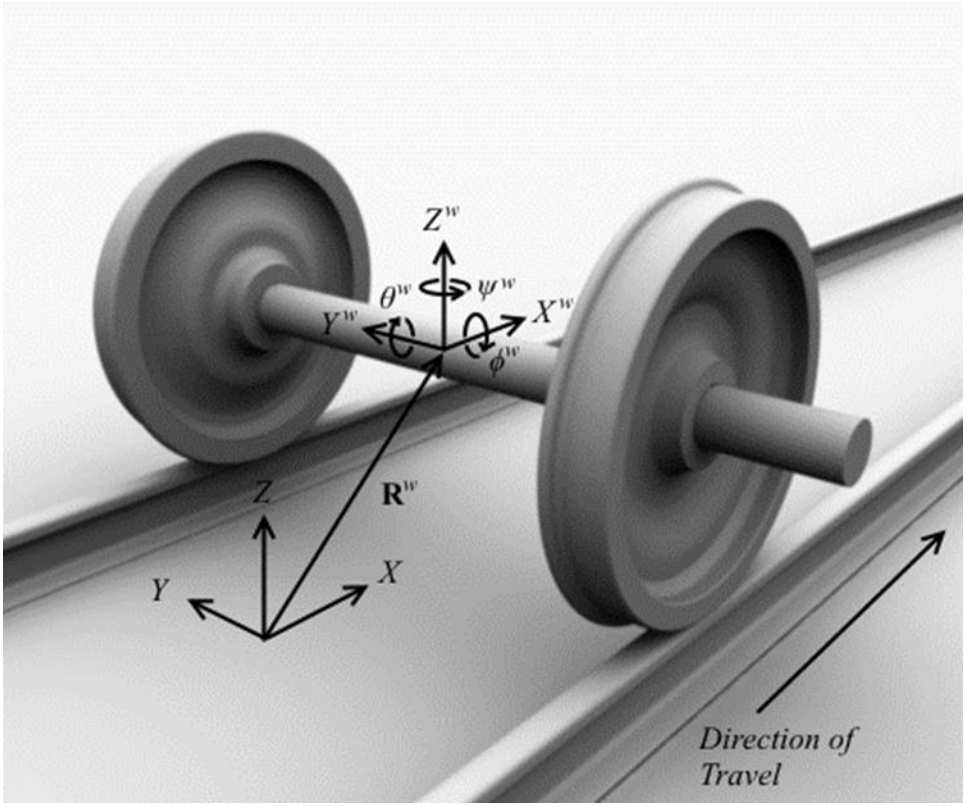

Figure 4.1. Coordinate Systems

The XY-plane is located in-plane with the rail head centers. The CBCS position is defined by the vector $\mathbf{R}^w = \begin{bmatrix} R_x^w & R_y^w & R_z^w \end{bmatrix}^T$. The orientation of the wheelset is defined using the three Euler angles ψ^w, ϕ^w, and θ^w about the Z^w, X^w, and Y^w axes respectively (Shabana, 2013). The angles ψ^w, ϕ^w, and θ^w are henceforth referred to as the *yaw*, *roll*, and *pitch* of the wheelset, respectively (Roberson and Schwertassek, 1988; Shabana et al., 2008). The wheelset *angle of attack* (AOA) α^w is shown in Fig. 4.2, and it is noted that $\alpha^w = -\psi^w$.

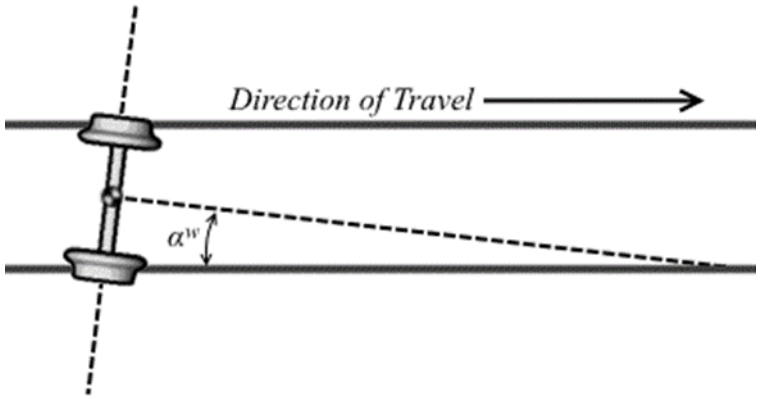

Figure 4.2. Wheelset Angle of Attack

The CBCS absolute velocity is defined by the vector $\dot{\mathbf{R}}^w = \begin{bmatrix} \dot{R}_x^w & \dot{R}_y^w & \dot{R}_z^w \end{bmatrix}^T$ and angular velocity by the vector $\boldsymbol{\omega}^w = \begin{bmatrix} \omega_x^w & \omega_y^w & \omega_z^w \end{bmatrix}^T$. The wheelset consists of two symmetric wheels rigidly connected by an axle. The inertial properties of the wheelset, including the mass m^w, and moments of inertia $\bar{i}_{xx}^w$, $\bar{i}_{yy}^w$, and $\bar{i}_{zz}^w$ about the X^w, Y^w, and Z^w axes, respectively, are given in Table 4.1.

m^w	$\bar{i}_{xx}^w$	$\bar{i}_{yy}^w$	$\bar{i}_{zz}^w$
1,568 kg	658 kg.m^2	168 kg.m^2	658 kg.m^2

Table 4.1. Wheelset Inertia Properties

Because of symmetry, the wheelset products of inertia with respect to the wheelset CBCS axes are equal to zero. The position and velocities of the wheelset at climb initiation are shown in Table 4.2.

R_x^w	R_y^w	R_z^w	ψ^w	ϕ^w	θ^w
0.1000 m	-1.9742e-2 m	0.4568 m	-0.0500 rad	-6.6643e-4 rad	0 rad
$\dot{R}_x^w$	$\dot{R}_y^w$	$\dot{R}_z^w$	ω_x^w	ω_y^w	ω_z^w
5 m/s	0 m/s	0 m/s	0.5215 rad/s	10.4208 rad/s	-6.9535e-2 rad/s

Table 4.2. Wheelset Initial Conditions

The wheel profile curve $g\left(s_1^w\right)$ used in this investigation is the AAR-1B profile curve, where s_1^w is a lateral surface parameter. The wheel surface is then obtained by the complete revolution of the profile curve about the wheelset axis. The wheel profile curve is shown in Fig. 4.3.

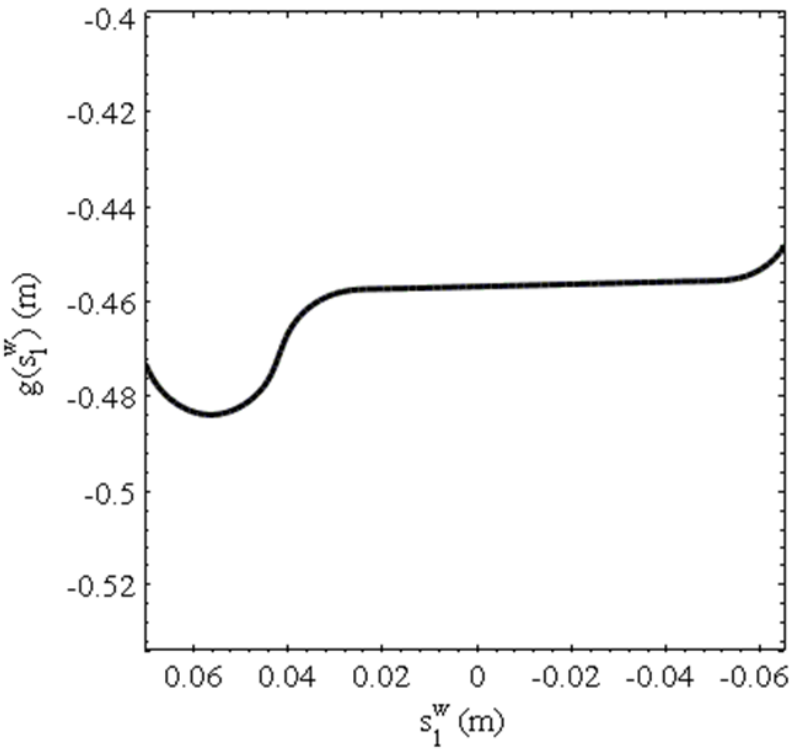

Figure 4.3. Wheel Profile Curve

In this investigation, the wheel profiles are located at a lateral distance of 0.74 m from the wheelset center.

The wheelset is driven into the right rail by an applied absolute lateral force that has magnitude equal to the weight of the wheelset. This force is held constant throughout the simulation and is applied at the wheelset center of mass. The wheelset experiences the effect of gravity but is not acted upon by any suspension forces. The two rails are completely fixed in space and do not experience any deflections. The rail profile curve $f\left(s_2^r\right)$ used in this investigation is the 140lb-A.R.E.A. profile, where s_2^r is a lateral surface parameter. The rail profile curve is shown in Fig. 4.4.

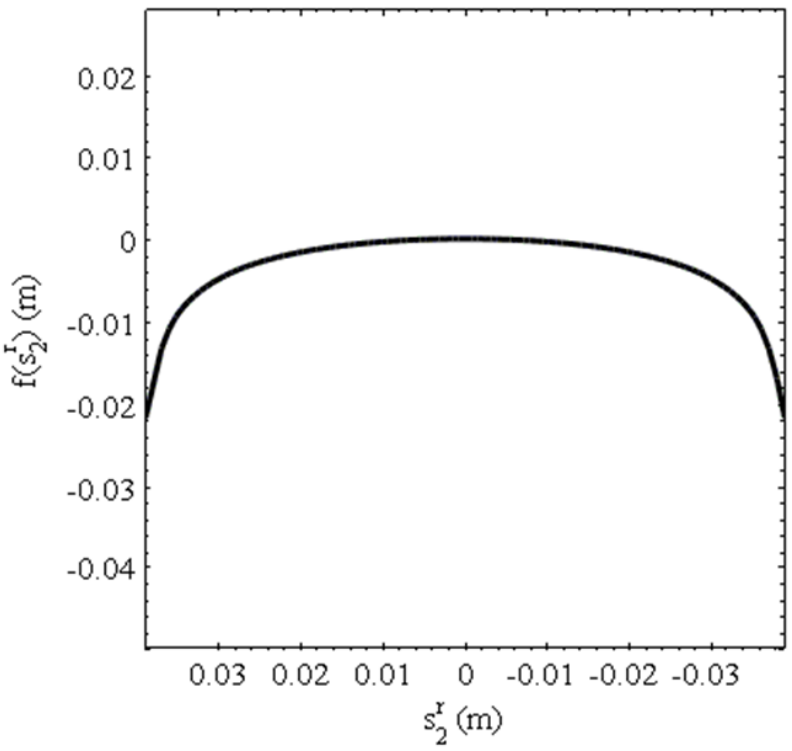

Figure 4.4. Rail Profile Curve

The rail profile frames are located at a lateral distance of 0.75565m from the track centerline and canted 25 mrad towards the track center. The wheel and rail are both modeled as steel and given identical material properties, including the modulus of elasticity E, modulus of rigidity G, and Poisson's ratio ν. These properties as well as the coefficient of friction μ between the surfaces are listed in Table 4.3.

μ	E	G
0.5	210 GPa	80 GPa

Table 4.3. Contact Parameters

The contacts between the wheel and rail surfaces are modeled using the ECF-A contact algorithm, which is an elastic contact formulation that allows small penetrations of the surfaces in contact and calculates the normal contact force using a complaint force element that includes stiffness and damping forces, as described in (Shabana et al., 2008). Such a model also allows for wheel/rail separation. Four nonlinear algebraic equations are solved using an iterative Newton-Raphson procedure to determine the values of the surface parameters at the contact points. These surface parameters are used to determine the location of the contact points online. The coordinates and velocities of the contact points are used to evaluate the penetration, normal forces, and creepages. The geometry of the wheel and rail and the normal contact force are used to determine the principal curvatures and the dimensions of the contact ellipse using Hertz's contact theory. The creep forces are calculated using Kalker's USETAB (Kalker, 1990). These forces are entered into the dynamic formulation as generalized forces associated with the MBS generalized coordinates. The system nonlinear dynamic equations of motion are integrated numerically using an explicit direct numerical integration method. Although an elastic contact formulation is used, the rigidity of the two bodies is still enforced, preventing the relative motion of any point on the bodies with respect to the body references.

4.1.2 Simulation Results

The numerical analysis of the model described above was carried out using SIGMA/SAMS (Shabana, 2010), a general-purpose MBS computer program. The results of the simulation are given in the following subsections. Snapshots of the derailment for the flanging and non-flanging wheels are given for reference in Fig. 5 for: the derailment initiation, 55.6 ms into the derailment, 111.4 ms into the derailment, and the simulation termination (223.0 ms).

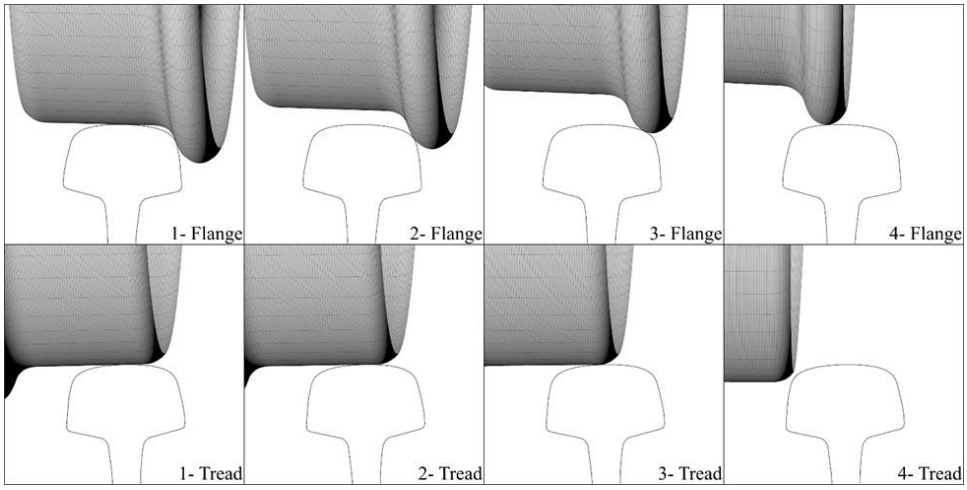

Figure 4.5. Front-View Derailment Snapshots

It is noted at this point that, for this derailment scenario, contact is maintained at the flange throughout the derailment. Contact is lost briefly at the tread contact point and then again permanently towards the end of the simulation.

4.1.2.1 Lateral Motion

The wheelset CBCS lateral displacement with respect to its initial configuration is plotted in Fig. 4.6.

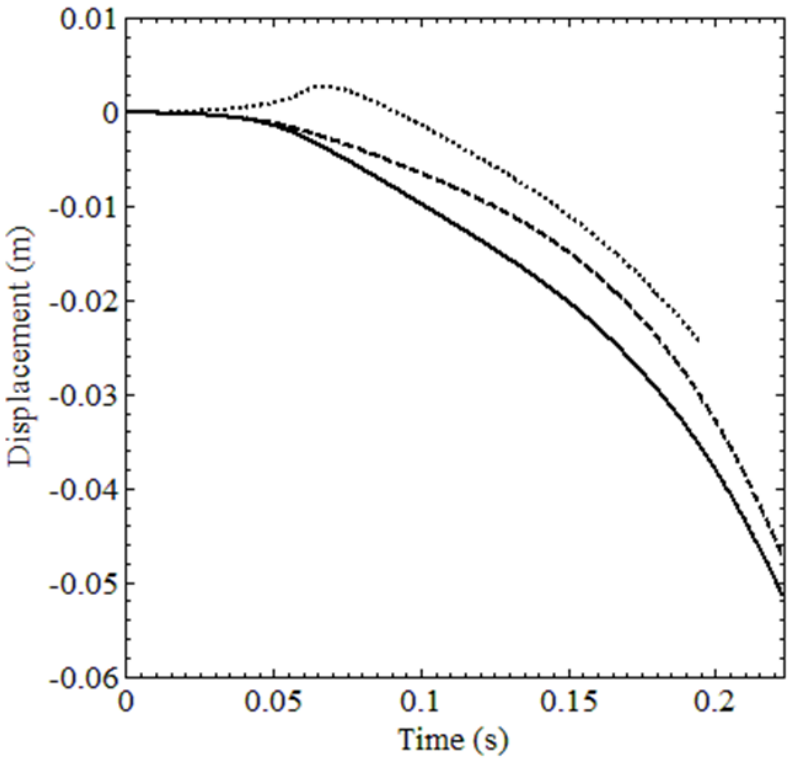

Figure 4.6. Lateral Displacements

(——— Wheelset, - - - - - - Flange, ... Tread)

The wheelset center is shown to move laterally towards the flanging rail under an applied lateral force. The rate of the lateral motion of the wheelset is shown to increase in magnitude as the

derailment continues. Also shown in the figure are the lateral displacements of the flanging and non-flanging contact points with respect to their initial positions. It is seen that the flanging contact point displaces laterally in the same direction of the wheelset, yet lags the displacement of the wheelset center due to the changing orientation of the wheelset. The non-flanging contact point is shown to move towards the rim of the wheel because of the changing orientation of the wheelset. Such motion becomes saturated, and the contact point then displaces laterally with the general motion of the wheelset.

Because of the tread conicity and flange geometry, a lateral shift of the wheelset in this climb scenario will result in a change of the rolling radius of each contact point, as demonstrated in Fig. 4.7, which shows the change in the rolling radius of the flanging and non-flanging wheels.

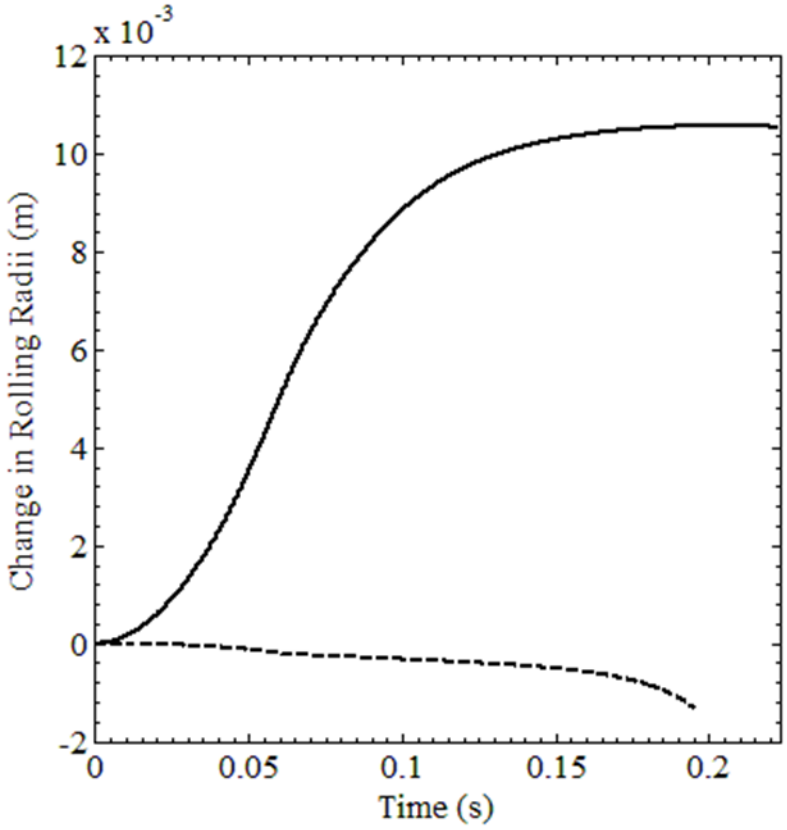

Figure 4.7. Change in Wheelset Rolling Radii

(——— Flange, - - - - - - Tread)

The rolling radius of the flange increases as the contact point moves towards the flange tip. The rolling radius of the tread decreases as the contact point moves to the tread rim, and then continues to decrease as the rim begins to leave the rail. A difference between the rolling radii of the two wheels will result in a roll angle. Therefore, the roll angle of the wheelset changes as the rolling radius of each wheel changes, as shown in Fig. 4.8.

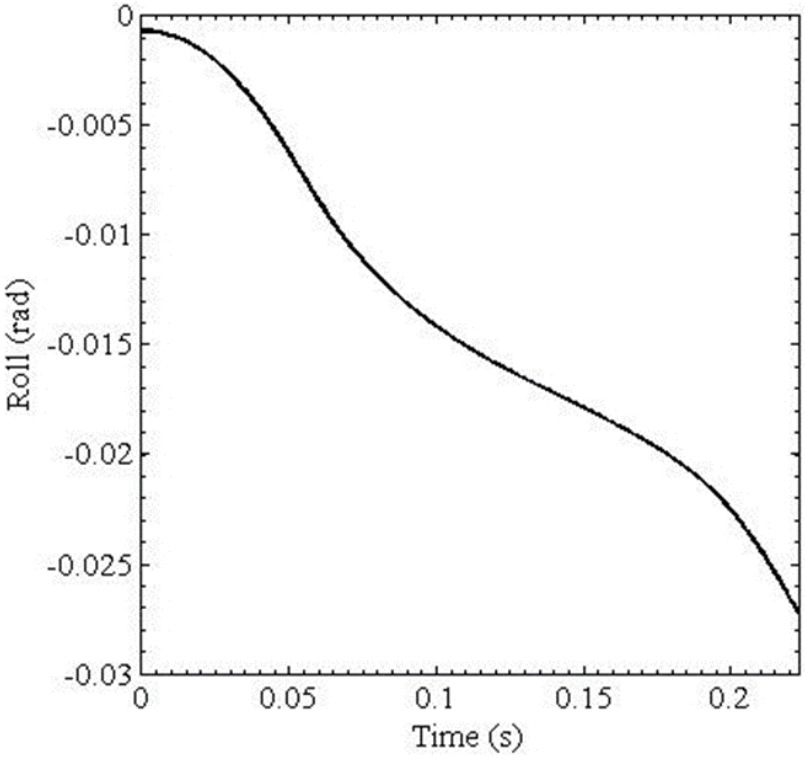

Figure 4.8. Wheelset Roll Angle

The roll angle increases in magnitude as the flanging wheel climbs the rail and the non-flanging wheel moves towards the track center.

4.1.2.2 Kinematics

As previously mentioned, an applied lateral force causes the wheelset to experience lateral displacement from its position at climb initiation. By kinematics, the contact between the flanging wheel and the rail requires the flanging wheel to, in general, displace vertically for any lateral shift. Exceptions could include any drastic changes in the wheelset orientation. However, once the contact point moves to the flange tip, the coupling between the lateral and vertical motion of the wheel is no longer maintained. The CBCS vertical displacement and the vertical displacements of the flanging and non-flanging contact points are plotted in Fig 4.9.

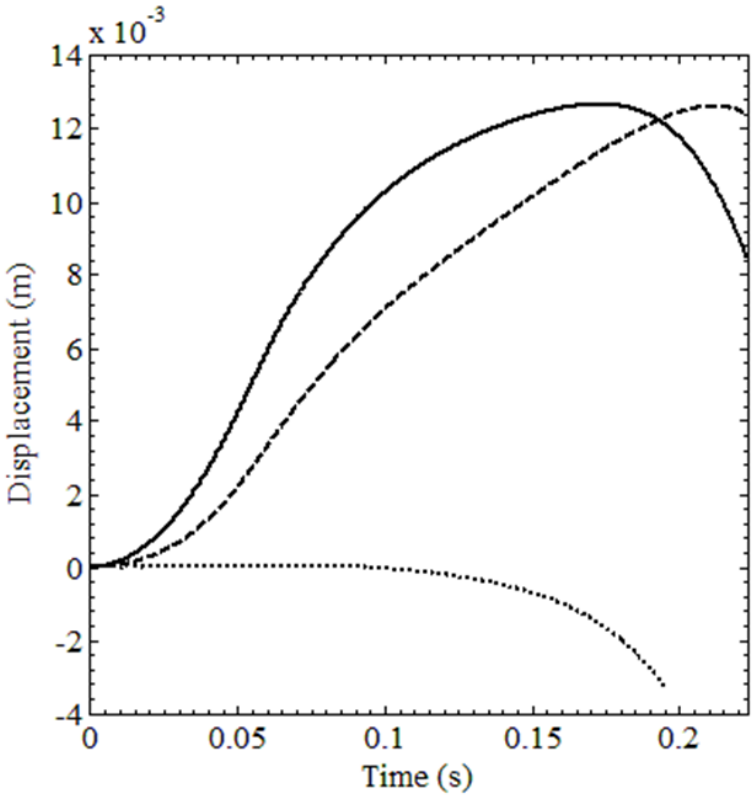

Figure 4.9. Vertical Displacements

(——— Wheelset, - - - - - - Flange, ... Tread)

The wheelset center of mass displaces upwards through the majority of the climb, and then moves downwards as the flanging contact point nears the top of the rail and the non-flanging contact point begins to fall from the rail. The flanging contact point climbs the rail throughout the derailment and then begins to move down the far side of the rail. The non-flanging contact point gradually displaces downward until the tread nears the edge of the rail, in which the motion is much more pronounced.

The kinematic motion restrictions are, in the case of elastic contact, imposed on the wheelset by reaction forces developed at the contact points. For the case of a wheelset negotiating a tangent track, the normal reaction forces act in the YZ-plane; the angles of the normal reaction forces, measured from the Y axis, are shown in Fig. 4.10.

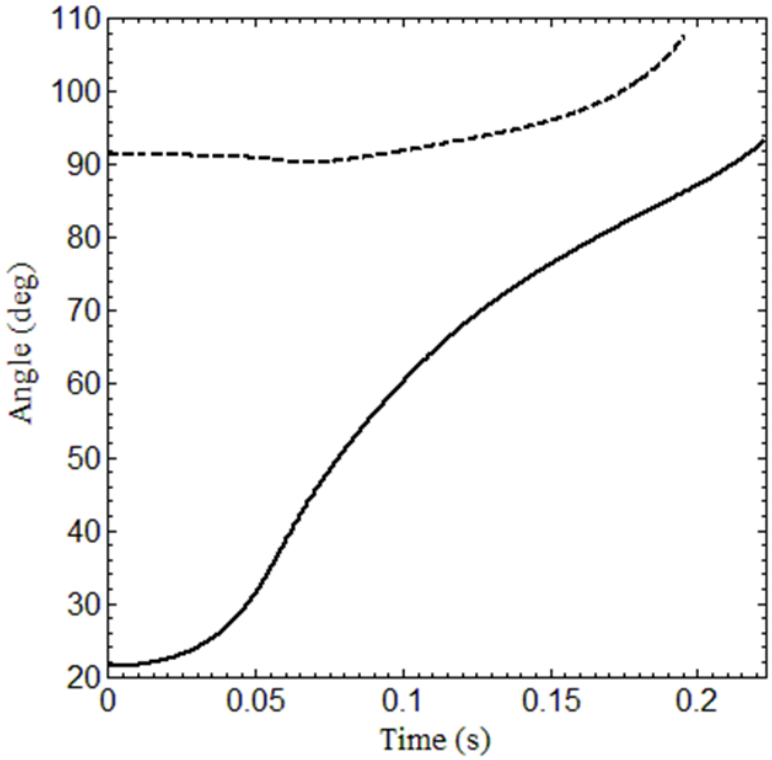

Figure 4.10. Reaction Force Orientations

(——— Flange, - - - - - - Tread)

The angle of the normal reaction force of the flanging contact point increases as the rail must transition from resisting the lateral motion created by the applied force to supporting the weight of the wheel. The angle of the normal reaction force of the non-flanging contact point decreases as the contact point moves to the rim of the wheel, and then increases as the contact point begins to move in the direction of the track center. The magnitudes of the normal reaction forces are shown in Fig. 4.11.

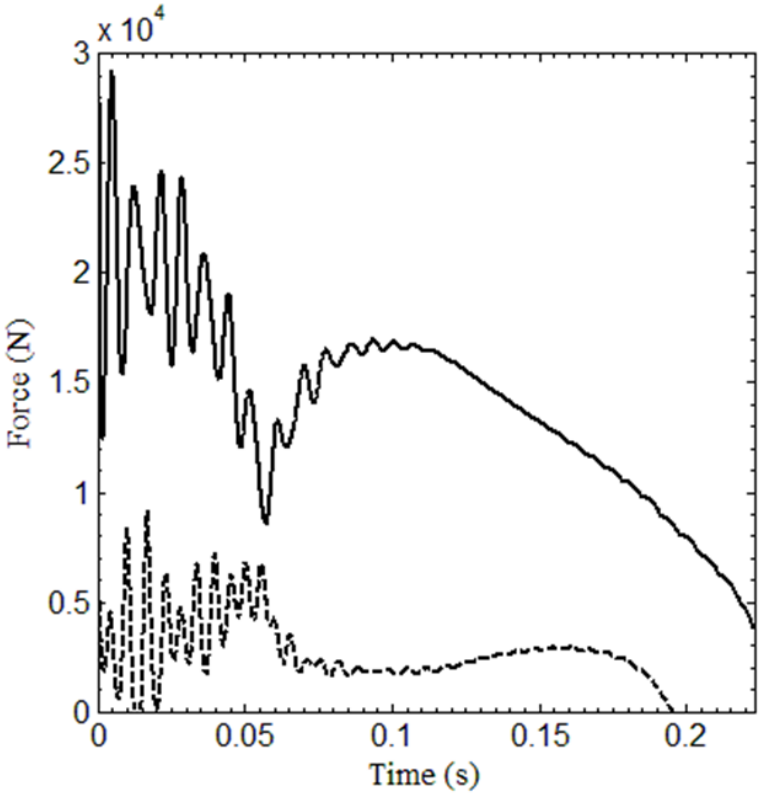

Figure 4.11. Reaction Force Magnitudes

(——— Flange, - - - - - - Tread)

The normal reaction forces are oscillatory by the nature of the contact formulation, and it is clear from the figure that the two wheels are unevenly loaded. The two magnitudes, in general, gradually converge until a point at which the direction of the friction forces changes sign, which will be discussed in the next section. It is at this point that the two magnitudes diverge. The flange normal reaction then decreases through the simulation. The non-flanging wheel begins to support a larger portion of the weight of the wheelset, until the tread begins to leave the rail.

4.1.2.3 Three-Dimensional Climb

Because the wheelset is oriented at an AOA, the contact forces will, in general, have non-zero components in three Cartesian directions with respect to the track. The wheelset AOA is shown in Fig. 12, and is shown to decrease throughout the derailment.

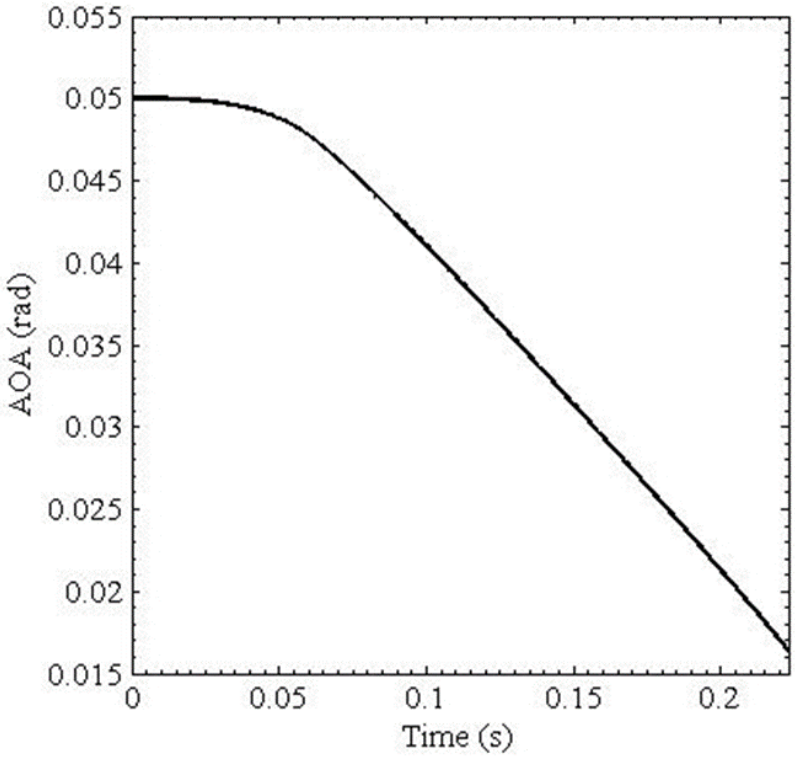

Figure 4.12. Wheelset Angle of Attack

The MBS model results shown in this figure clearly demonstrate that the AOA remains nearly constant in the vicinity of the climb initiation. The change is gradual at the initiation of the climb, but then becomes more pronounced as the derailment propagates. The components of the friction forces generated at the flanging and non-flanging contact points are shown in Figs. 4.13 and 4.14, respectively. It is clear from the figures that the forces are, in general, three-dimensional with respect to the track.

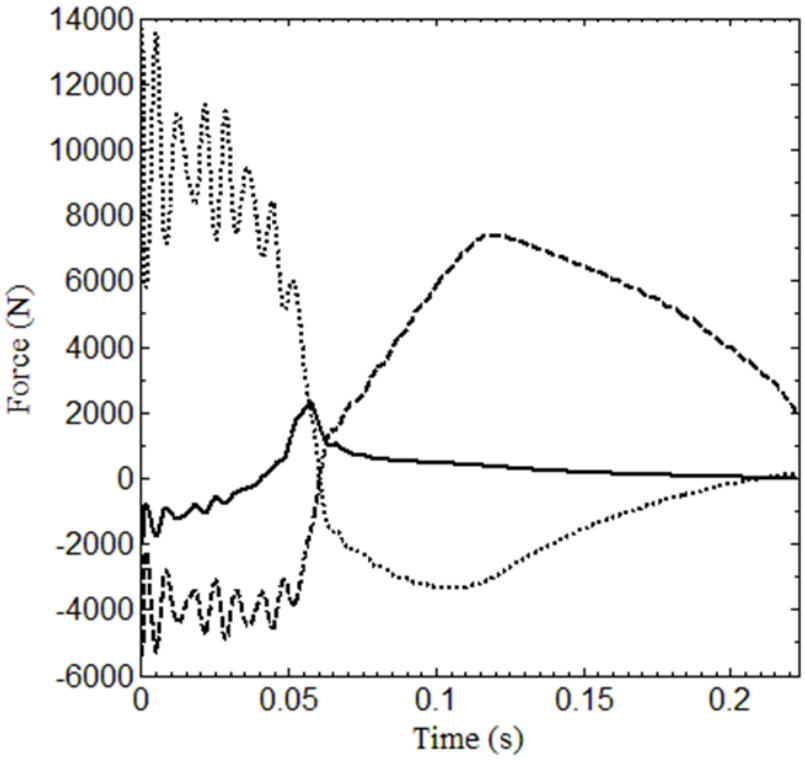

Figure 4.13. Flange Friction Components

(——— X, - - - - - - Y, ... Z)

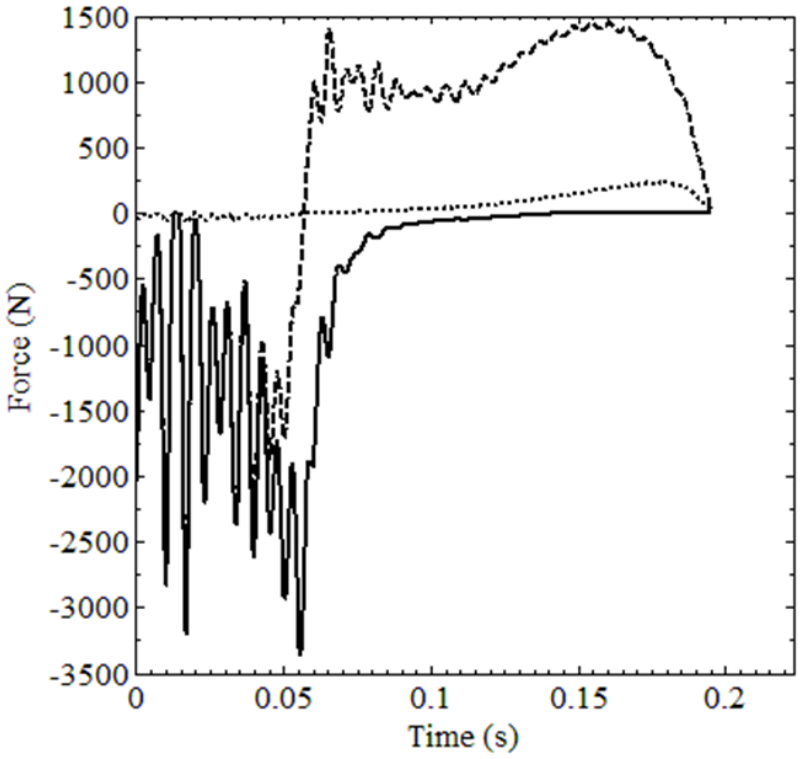

Figure 4.14. Tread Friction Forces

(——— X, - - - - - - Y, ... Z)

It is noted that the Y and Z components of the friction forces change direction during the derailment, for both the flanging and non-flanging contact points.

4.1.2.4 <u>Derailment Measure</u>

As seen above, the wheel climb derailment has vertical force contributions from both the normal reaction forces as well as the friction forces, indicating that the motion must be studied from both

kinematic and kinetic perspectives. Additionally, when taking both the normal reaction and friction forces into account, it is clear that the derailment is not two-dimensional, and that the motion should not be studied using any planar formulation. Such contact forces as mentioned above are, in practice, measured at the wheel rail interface. It should be noted, however, that such measures are not indicative of the force driving the wheelset to derailment. Figure 15 shows the ratio of the total lateral contact forces to magnitude of the applied lateral force experienced by the wheelset.

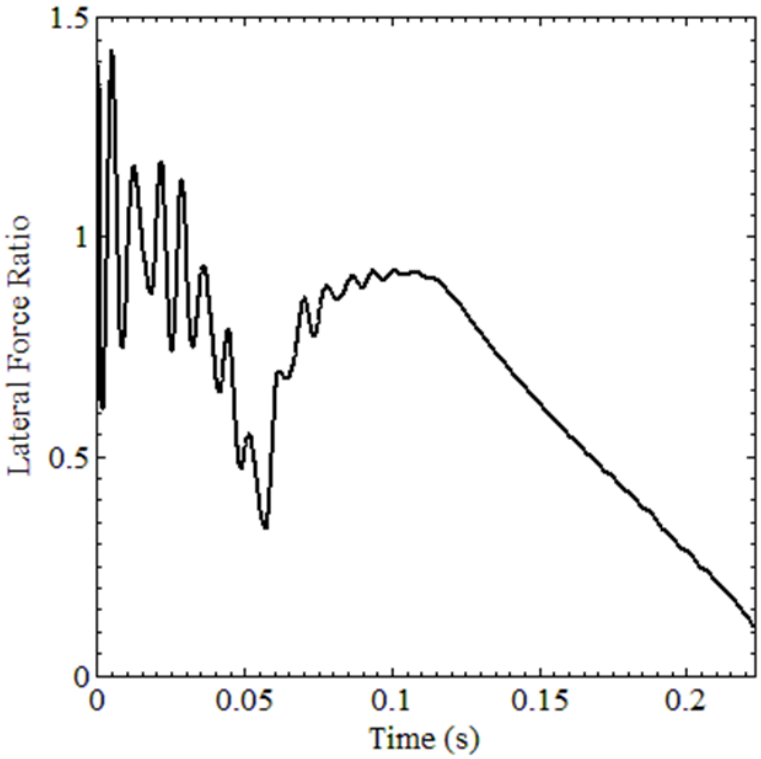

Figure 4.15. Lateral Force Ratio

It is clear that the forces are not representative and caution should be taken when using such measures in derailment investigations.

The L/V Limit Criterion was introduced in order to predict and prevent wheel climb derailments, and states that when the ratio of the lateral contact force to the vertical contact force of the wheel flange exceeds a certain limit, wheel climb will occur. Three L/V ratios are shown in Fig. 4.16: the actual L/V measured at the flanging contact point, the result of the Nadal L/V calculation if the flange angle used in the calculation is updated at each step of the simulation, and the result of the Nadal L/V calculation if the maximum flange angle of the wheel is used at each time step.

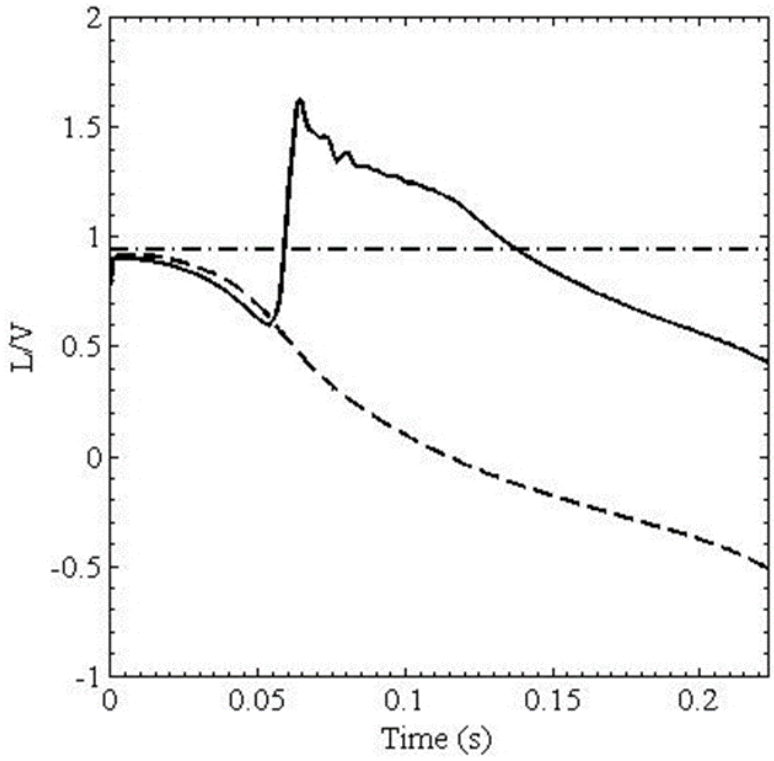

Figure 4.16. Right Flange L/V

(——— Measured, - - - - - - Updated Nadal, - . - . - . - Max Nadal)

There are three important details of this figure: first, the wheelset derailment initiates at a value that is less than the Nadal L/V limit, indicating that the measure is not conservative. Second, the wheelset L/V then begins to increase during the changing of the friction directions, increasing past the Nadal L/V limit calculation. Third, the wheelset L/V then falls below the Maximum Nadal L/V, although the derailment continues.

4.1.3 Verification of the Model Results

In order to verify the results of the MBS model, a simple semi-analytical model can be developed, and will be formulated in the following sections. This simple model consists of a wheelset, in which contact is only modeled at one wheel that is represented by a disk, and a rail. Because of the geometric and kinematic assumptions used in the semi-analytical model, the comparison of the two models should be limited to the vicinity of the climb initiation. In the vicinity of the climb initiation, the results of the two models agree well, as will be demonstrated later in this chapter. The predicted L/V ratios obtained using the two models are in a good agreement. After the short lived interval of the climb initiation, it is expected that the results of the two models will not be in a good agreement because of the motion and geometric assumptions used in developing the semi-analytical model. The fact that the results of the two models agree well in the vicinity of the wheel climb initiation confirms that a major contribution to the climb initiation is the kinematic restriction imposed on the motion of the wheel as it comes into contact with the rail.

4.2 Semi-Analytic Climb Model

As previously mentioned, there is a strong belief in the rail industry and research community that wheel climb at a large AOA is initiated by friction. The argument often made is that as the wheel comes into flange contact with the rail at a large AOA, an increase in the lateral force acting on the wheel leads to an increase in the normal reaction force at the flange contact point. Since in this case the contact point on the wheel is moving downward, the large reaction force normal to the flange produces a significant upward friction force that results in wheel climb. The goal is to use a simple model that sheds light on the forces that contribute to the wheel climb initiation in the

case of large AOA, and to compare these contributions against the fully nonlinear unconstrained MBS model results.

4.2.1 Angle of Attack Assumption

In this semi-analytical model, the AOA is assumed constant. When investigating the cases of constant or non-constant AOA, it is important to point out that when the wheel contacts the rail with a large AOA, a change in the AOA requires a large lateral force, which when combined with the resulting normal reaction force at the contact point, produces a large yaw moment sufficient to decrease the AOA. This effect is seen in the MBS model results. Nonetheless, such a decrease does not occur instantaneously and requires time; this is particularly true in the case of a large wheelset mass moment of inertia. Furthermore, a significant decrease in the AOA over a short time period is likely to lead to wheel/rail separation which is not the scenario considered in this investigation. Therefore, when examining the very brief period of climb initiation, assuming the AOA as constant is justified. The case of non-constant AOA will be considered in future investigations.

4.2.2 Simplifications

The semi-analytical model examines the case of a wheelset negotiating a tangent track at a large and constant AOA. In order to reflect on the Nadal L/V ratio, which is used as the basis for many derailment criteria, the model developed in this investigation will examine the forces at the wheel flange only. The inertia of the non-flanging wheel and wheelset axle is still taken into account. The rail community's interpretation of the mechanism of wheel climb at a large AOA is clearly

based on two basic assumptions: First, it is assumed that the wheel remains in contact with the rail during the process of wheel climb. Second, because of the assumption of large AOA, it assumed that the contact point remains on the wheel flange. In the case of a constant large AOA and using the geometry assumptions employed in this section, the following two basic assumptions can be made when developing the simplified semi-analytical model:

1. *The wheel/rail contact occurs on the wheel flange, and the contact point moves on a circular curve*. For the model considered in this investigation, this circular curve is assumed to have a constant radius, and therefore, the flange geometry does not enter into the formulation of the contact problem. This simplifying assumption allows deriving a closed form kinematic relationship that sheds light on the climb initiation. This closed form kinematic relationship cannot be obtained if the flange geometry is considered.
2. *There is no wheel/rail separation during the distance to climb*. This assumption has been used in previous investigations by other researchers in developing derailment criteria. Wheel/rail separation during climbing can introduce impact forces and discontinuities that are not considered in the simplified model developed in this study. The continuous wheel/rail contact can be modeled using a penalty or constraint formulation (Shabana and O'Shea, 2013). In principle, both formulations should lead to similar results. The constraint method has the advantage of reducing the model dimensionality and allows for obtaining closed form expressions for some of the kinematic and force variables of the model considered in this investigation.

Both of these assumptions will be used in this section to examine if wheel climb is initiated purely by friction or if there are significant kinematic contributions that lead to an instantaneous initiation

of wheel climb. This wheel climb may or may not be sustained by other forces, including the friction force. The problem is reduced geometrically using the above assumptions to modeling the contact between a circular arc and a straight line. The model geometry simplifications are shown in Fig. 4.17.

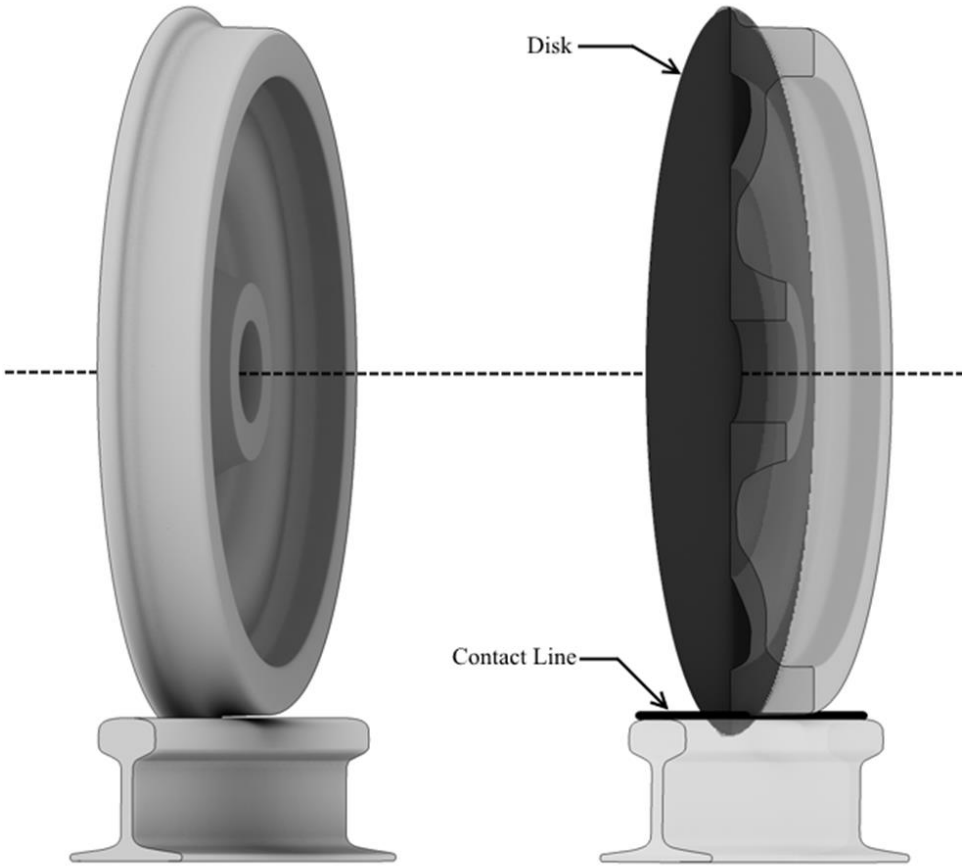

Figure 4.17. Geometric Wheel Flange/Rail Contact Simplification at a Large Angle of Attack

As previously mentioned, in order to ensure that these simplifications lead to a model that produces valuable information on the nature of wheel climb initiation, the results obtained using the simplified model are compared against the general fully nonlinear three-dimensional MBS model that is based on an elastic contact formulation that allows for wheel/rail separation and accounts for the wheel and rail profile geometries.

4.2.3 Distance to Climb

The analysis of the model developed in this section will show that in the case of a tangent track, large AOA, and zero roll angle, the wheel longitudinal motion is completely decoupled from the vertical and yaw displacements in the vicinity of the climb initiation. Therefore, the use of the *distance to climb* in tangent track wheel climb criteria needs to be investigated. Furthermore, the model developed in this section will show that there is no coupling between the pitch rotation and both the vertical and yaw displacements of the wheel in the vicinity of the climb initiation. The pitch rotation has an effect on the velocity of the contact point, and consequently, on the direction of the friction force that influences the vertical motion of the wheel. It is important, however, to point out that these conclusions regarding the distance to climb and the pitch rotation may not be applicable in the case of curve negotiations; a case that will be considered in future investigations.

4.2.4 Kinematics

In this section, the kinematic constraints that govern the motion of a simplified wheel climb model are formulated in order to shed light on some of the concepts that must be considered when the phenomenon of wheel climb at a large AOA is considered.

4.2.4.1 Geometry

In the analysis presented in this section it is assumed that the wheel (disk), shown in Fig. 4.18, has a large AOA α, negotiates a track segment approximated as tangent, and has zero roll angle ϕ.

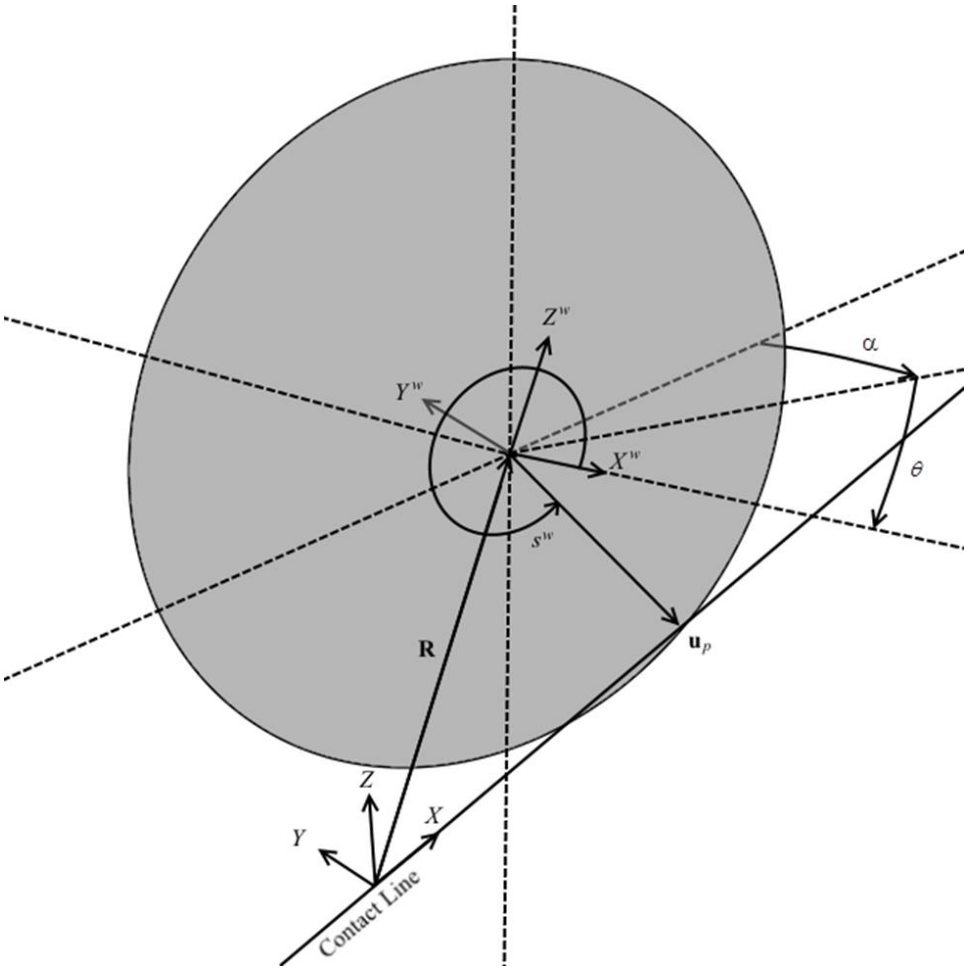

Figure 4.18. Simplified Model Geometry and Coordinates

Because of the simple geometry used, the AOA α can be related to the wheel yaw angle ψ. The wheel, which is assumed in this section to have the simplified geometry of a disk, is assumed to have a pitch rotation θ about its axis and maintains a contact with the rail. The transformation matrix that defines the wheel orientation in the global coordinate system is given by

$$\mathbf{A} = \begin{bmatrix} \cos\theta\cos\alpha & -\sin\alpha & \sin\theta\cos\alpha \\ \cos\theta\sin\alpha & \cos\alpha & \sin\theta\sin\alpha \\ -\sin\theta & 0 & \cos\theta \end{bmatrix} \tag{4.1}$$

Using Fig. 4.18 and the assumption that the contact occurs on wheel flange, the location of the contact point on the rotating wheel can be defined with respect to the wheel coordinate system as

$$\bar{\mathbf{u}}_P = \begin{bmatrix} r\cos s^w & 0 & r\sin s^w \end{bmatrix}^T \tag{4.2}$$

In this equation, s^w is an angular parameter that defines the location of the contact point, and r is the radial distance between the contact point and the wheel center. In this section, r is assumed to remain constant and equal to the radius of the wheel at the contact point. Using this assumption and the assumption of non-conformal contact, the contact problem is reduced to a circular arc/straight line contact. Consequently, one needs only one geometric parameter s^w which will be treated as a non-generalized coordinate (Shabana and Sany, 2001). This parameter will be systematically eliminated using the contact constraint.

Assuming that the rail is fixed and the wheel is translating and rotating, the global position vector $\mathbf{r}_P = \begin{bmatrix} (\mathbf{r}_P)_x & (\mathbf{r}_P)_y & (\mathbf{r}_P)_z \end{bmatrix}^T$ of the contact point can be written as

$$\mathbf{r}_P = \mathbf{R} + \mathbf{A}\bar{\mathbf{u}}_P = \begin{bmatrix} R_x \\ R_y \\ R_z \end{bmatrix} + r \begin{bmatrix} \cos\left(\theta - s^w\right)\cos\alpha \\ \cos\left(\theta - s^w\right)\sin\alpha \\ -\sin\left(\theta - s^w\right) \end{bmatrix} \tag{4.3}$$

In this equation, $\mathbf{R} = \begin{bmatrix} R_x & R_y & R_z \end{bmatrix}^T$ is the global position vector of the wheel center. It is clear from Eq. 4.3 that in order to determine the global position of the contact point, one must determine first the geometric parameter s^w as well as the wheel generalized coordinates $\mathbf{R}$ and θ.

4.2.4.2 Contact Constraints

If the rotating wheel remains in contact with the rail, the two constraint equations $\left(\mathbf{r}_P\right)_y = y_c$ and $\left(\mathbf{r}_P\right)_z = z_c$, where y_c and z_c are constants that define the location of the rail as shown in Fig. 4.18, must be satisfied. These equations can be written more explicitly using Eqs. 4.1 and 4.3 as

$$\left.\begin{aligned} R_y + r\cos\left(\theta - s^w\right)\sin\alpha = y_c \\ R_z - r\sin\left(\theta - s^w\right) = z_c \end{aligned}\right\} \tag{4.4}$$

The non-generalized coordinate s^w can be eliminated from these two equations leading to the following single constraint equation; this constraint equation is applicable in the two cases of constant and non-constant AOA:

$$\left(R_y - y_c\right)^2 + \left(R_z - z_c\right)^2 \sin^2\alpha = r^2 \sin^2\alpha \tag{4.5}$$

4.2.4.3 Study Model

Two different cases can be considered in developing this semi-analytical wheel climb model. In the first case, the AOA α is assumed to remain constant and this angle is not considered as a degree of freedom of the system. In this first case, there is a constraint moment associated with the yaw rotation. In the second case, the AOA is allowed to vary and is considered as a degree of freedom of the system. Consequently, the yaw inertia must be considered. It is important, however, to point out that the change in the yaw angle as the result of an increase in the lateral force has to evolve with time, and such a change is not instantaneous.

This section is focused on the first case in which the AOA is assumed to be constant. Because of its simplicity, the model with the constant AOA is considered first, while the more complex model in which the AOA is allowed to vary will be considered in future investigations. Nonetheless, the kinematic equations developed in this section are applicable to both models. Furthermore, the results obtained using the constant AOA model will be compared, in the vicinity of the climb initiation, with the results of the fully nonlinear unconstrained model.

4.2.5 Constant Angle of Attack

In this section, the nonlinear algebraic equation that defines the contact constraints at the velocity level is obtained from Eq. 4.5. The resulting velocity relationship is used to develop the velocity transformation matrix that allows formulating the equations of motion in terms of a minimum set of independent coordinates.

4.2.5.1 Velocity Constraint

In the special case of constant AOA, the constraint equation at the velocity level can be obtained by differentiating Eq. 4.5 with respect to time as

$$\left(R_y - y_c\right)\dot{R}_y + \left(R_z - z_c\right)\dot{R}_z \sin^2\alpha = 0 \tag{4.6}$$

Using this equation, one can show that the contact constraint equation of 4.5 in the case of constant AOA can be written at the velocity level as

$$\dot{R}_y - h_z\dot{R}_z = 0 \tag{4.7}$$

where

$$h_z = -\frac{R_z - z_c}{R_y - y_c}\sin^2\alpha = -\frac{d_z}{d_y}\sin^2\alpha \tag{4.8}$$

where $d_y = R_y - y_c$ and $d_z = R_z - z_c$ are, respectively, the lateral and vertical distances of the wheel center from the contact point. Note that if R_z and θ and their derivatives are known, Eq. 4.4 can be used to solve for R_y and s^w, and the time derivative of Eq. 4.4 can be used to solve for $\dot{R}_y$ and $\dot{s}^w$. The calculation of R_y and s^w and their derivatives is necessary in order to be able to determine the position of the contact point on the wheel.

4.2.5.2 A Wheel Climb Mechanism

The constraint relationship of Eq. 4.5 plays a significant role in the analysis presented in this section. This equation can be used to shed light on the initiation of wheel climb in the case of relatively large AOA. It is clear that this equation includes the positive terms d_y^2, $d_z^2\sin^2\alpha$, and

$r^2 \sin^2 \alpha$. In the case of a lateral force applied in a direction that leads to a decrease in d_y^2, Eq. 4.4 clearly shows that d_z^2 must increase if the AOA is to remain constant. Such an increase in d_z^2 is governed by an algebraic equation, and therefore, the initiation of such a wheel climb can be instantaneous. This kinematic condition leads to motion that is fundamentally different from force-produced motion that evolves with time.

4.2.5.3 Velocity Transformation

Assuming that the yaw angle ψ and the roll angle ϕ of the wheel remain constant and using the velocity constraint of Eq. 4.7, one can write the following velocity transformation:

$$\begin{bmatrix} \dot{R}_x \\ \dot{R}_y \\ \dot{R}_z \\ \dot{\psi} \\ \dot{\phi} \\ \dot{\theta} \end{bmatrix} = \begin{bmatrix} 1 & 0 & 0 \\ 0 & h_z & 0 \\ 0 & 1 & 0 \\ 0 & 0 & 0 \\ 0 & 0 & 0 \\ 0 & 0 & 1 \end{bmatrix} \begin{bmatrix} \dot{R}_x \\ \dot{R}_z \\ \dot{\theta} \end{bmatrix} \tag{4.9}$$

Let $X^w Y^w Z^w$ be the centroidal wheel coordinate system as shown in Fig. 4.18. In the case of the sequence of Euler angles defined by a rotation ψ about the Z^w axis, a rotation ϕ about the X^w axis, and a rotation θ about the Y^w axis, the angular velocity vector defined in the wheel coordinate system can, in general, be written as

$$\bar{\boldsymbol{\omega}} = \begin{bmatrix} -\cos\phi \sin\theta & \cos\theta & 0 \\ \sin\phi & 0 & 1 \\ \cos\phi \cos\theta & \sin\theta & 0 \end{bmatrix} \begin{bmatrix} \dot{\psi} \\ \dot{\phi} \\ \dot{\theta} \end{bmatrix} \tag{4.10}$$

Using the yaw and roll angle constraints, it follows that the angular velocity and angular acceleration vectors defined in the wheel coordinate system are $\bar{\boldsymbol{\omega}} = \begin{bmatrix} 0 & 1 & 0 \end{bmatrix}^T \dot{\theta}$ and $\bar{\boldsymbol{\alpha}} = \begin{bmatrix} 0 & 1 & 0 \end{bmatrix}^T \ddot{\theta}$, respectively. Using this fact, the acceleration transformation can be written as

$$\begin{bmatrix} \ddot{R}_x \\ \ddot{R}_y \\ \ddot{R}_z \\ \bar{\alpha}_x \\ \bar{\alpha}_y \\ \bar{\alpha}_z \end{bmatrix} = \begin{bmatrix} 1 & 0 & 0 \\ 0 & h_z & 0 \\ 0 & 1 & 0 \\ 0 & 0 & 0 \\ 0 & 0 & 1 \\ 0 & 0 & 0 \end{bmatrix} \begin{bmatrix} \ddot{R}_x \\ \ddot{R}_z \\ \ddot{\theta} \end{bmatrix} + \begin{bmatrix} 0 \\ \dot{h}_z \dot{R}_z \\ 0 \\ 0 \\ 0 \\ 0 \end{bmatrix} \tag{4.11}$$

In this equation, $\dot{h}_z = -\left(\left(\left(R_y - y_c \right) \dot{R}_z - \left(R_z - z_c \right) \dot{R}_y \right) \Big/ \left(R_y - y_c \right)^2 \right) \sin^2 \alpha$. The transformation of Eq. 4.11 will be used in the following section to obtain the independent differential equations of motion of the wheel for a given AOA α.

4.2.6 Equations of Motion

The spatial Newton-Euler equations of motion of the wheel are given as

$$\begin{bmatrix} m\mathbf{I} & \mathbf{0} \\ \mathbf{0} & \bar{\mathbf{I}}_{\theta\theta} \end{bmatrix} \begin{bmatrix} \ddot{\mathbf{R}} \\ \bar{\boldsymbol{\alpha}} \end{bmatrix} = \begin{bmatrix} \mathbf{F}_e + \mathbf{F}_c \\ \bar{\mathbf{M}}_e + \bar{\mathbf{M}}_c - \bar{\boldsymbol{\omega}} \times (\bar{\mathbf{I}}_{\theta\theta} \bar{\boldsymbol{\omega}}) \end{bmatrix} \tag{4.12}$$

where m is the mass of the wheel, $\mathbf{I}$ is a 3×3 identity matrix, $\bar{\mathbf{I}}_{\theta\theta}$ is the inertia tensor defined with respect to the centroidal body coordinate system, $\bar{\boldsymbol{\alpha}} = \dot{\bar{\boldsymbol{\omega}}}$ is the absolute angular acceleration vector defined in the body coordinate system, $\mathbf{F}_e$ and $\mathbf{F}_c$ are, respectively, the resultant of the external and constraint forces defined in the global coordinate system, and $\bar{\mathbf{M}}_e$ and $\bar{\mathbf{M}}_c$ are, respectively, the resultant of the external and constraint moments defined in the body coordinate system.

Because of the definition of Euler equations in the body coordinate system, the inertia matrix is constant. It is assumed that the constant inertia tensor $\bar{\mathbf{I}}_{\theta\theta}$ is diagonal with diagonal elements I_{xx}, I_{yy}, and I_{zz}. One can show that in the case of the simple rotation of the wheel about its Y^w axis, the gyroscopic moment $\bar{\boldsymbol{\omega}} \times (\bar{\mathbf{I}}_{\theta\theta} \bar{\boldsymbol{\omega}})$ is equal to zero.

4.2.6.1 Equations in Terms of the Degrees of Freedom

Using the transformation of Eq. 4.11, the independent equations of motion of the wheel in the simplified semi-analytical model can be written as

$$\begin{bmatrix} m & 0 & 0 \\ 0 & m\left(1+h_z^2\right) & 0 \\ 0 & 0 & I_{yy} \end{bmatrix} \begin{bmatrix} \ddot{R}_x \\ \ddot{R}_z \\ \ddot{\theta} \end{bmatrix} = \begin{bmatrix} F_x \\ F_z + h_z F_y \\ \bar{M}_y \end{bmatrix} - \begin{bmatrix} 0 \\ m h_z \dot{h}_z \dot{R}_z \\ 0 \end{bmatrix} \tag{4.13}$$

The solution of this equation defines $\ddot{R}_z$ as

$$\ddot{R}_z = \frac{1}{m\left(1+h_z^2\right)} \left(F_z + h_z F_y - m h_z \dot{h}_z \dot{R}_z \right) \tag{4.14}$$

Using the definition of $\dot{h}_z$ given after Eq. 4.11, the preceding equation can be written as

$$\ddot{R}_z = \frac{1}{m\left(1+h_z^2\right)} \left(F_z + h_z F_y + c_z \dot{R}_z^2 \right) \tag{4.15}$$

In this equation, $c_z = m h_z \left(\sin^2 \alpha + h_z^2\right) \big/ \left(R_y - y_c\right)$. If the contact point lies below the center of mass of the wheel, one can show that c_z is always positive, and h_z is always negative. This

implies that the last two terms in Eq. 4.15 lead to positive vertical forces in the case of negative lateral force.

4.2.6.2 Contact Force

In the case of friction, the friction force is function of the normal force at the contact point and it has direction opposite to the direction of the sliding velocity. Using the expressions of $\ddot{R}_z$ and $\ddot{\theta}$ obtained in the preceding section, the coordinates R_z and θ and their first derivatives $\dot{R}_z$ and $\dot{\theta}$ can be obtained using the methods of numerical integration. The coordinate R_y and the non-generalized coordinate s^w can be determined using the constraint relationship of Eq. 4.4. Knowing s^w, the coordinates that define the location of the contact point $\bar{\mathbf{u}}_P$ of Eq. 4.2 can be evaluated. The absolute velocity of the contact point can then be determined as $\mathbf{v}_P = \dot{\mathbf{r}}_P = \dot{\mathbf{R}} + \boldsymbol{\omega} \times \mathbf{u}_P$, where $\boldsymbol{\omega} = \mathbf{A}\bar{\boldsymbol{\omega}}$, and $\mathbf{u}_P = \mathbf{A}\bar{\mathbf{u}}_P$; both $\bar{\boldsymbol{\omega}}$ and $\bar{\mathbf{u}}_P$ are previously defined in this chapter. Note that the direction of the velocity vector $\mathbf{v}_P$ of the contact point, which defines the direction of the friction force, depends on the direction of the wheel forward velocity as well as the pitch rotation of the wheel.

In order to have an estimate of this friction force, the lateral contact force resulting from the constraints must be evaluated. Using Eqs. 4.11 and 4.15, the acceleration component $\ddot{R}_y$ can be written as

$$\begin{aligned}\ddot{R}_y &= h_z\ddot{R}_z + \dot{h}_z\dot{R}_z \\ &= \frac{h_z}{m\left(1+h_z^2\right)}\left(F_z + h_z F_y + c_z\dot{R}_z^2\right) + \dot{h}_z\dot{R}_z\end{aligned} \tag{4.16}$$

Using this result and the equations of motion, the lateral constraint force F_{cy} at the contact point can be written as

$$\begin{aligned}F_{cy} &= m\ddot{R}_y - F_y \\ &= \frac{h_z}{\left(1+h_z^2\right)}\left(F_z + h_z F_y + c_z\dot{R}_z^2\right) + m\dot{h}_z\dot{R}_z - F_y\end{aligned} \tag{4.17}$$

This equation shows that the lateral reaction force F_{cy} is in general different from the external force F_y that produces the motion. One can also show that even in this very simplified example, there is a vertical reaction force $F_{cz} = -h_z F_{cy}$. Therefore, the resultant of the constraint force F_c makes an angle with the lateral *Y*-axis that can be determined from the ratio between the vertical and lateral constraint force components. This ratio is defined by h_z which depends on the AOA. The ratio between the lateral and vertical reaction force is defined by $\left(F_{cy}/F_{cz}\right) = -1/h_z$. Note that this ratio is function of the parameters that define the contact constraints, and if the contact conditions are maintained this ratio is governed by a well-defined algebraic equation. This ratio can be expressed in terms of the AOA as $d_y/\left(d_z \sin^2\alpha\right)$, where d_y and d_z are, respectively, the lateral and vertical distances of the wheel center from the contact point. Note that this ratio does not depend explicitly on the applied forces or the coefficient of friction. The resultant of the constraint force is therefore defined as $F_c = \sqrt{1+h_z^2}F_{cy}$. It is important to point out that while the constraint

force does not do work, such a force restricts the motion of the wheel to be in certain directions, one possible direction can be the climb direction.

If the effect of friction is considered, the friction force μF_c, where μ is the friction coefficient, must be calculated. This friction force, however, can have three components in three different directions because the relative velocity at the contact point can have three non-zero components with respect to the rail. This general relative velocity is attributed to the longitudinal motion, climb, and pitch rotation. The lateral relative velocity can be easily understood because of the climb vertical motion. Such a lateral velocity is necessary in order to ensure that the contact constraints are satisfied. Therefore, the resultant of the friction force F_f is not directed upward and this resultant can be written as

$$F_f = \mu F_c = \mu\sqrt{\left(1+h_z^2\right)}\left(\frac{h_z}{\left(1+h_z^2\right)}\left(F_z + h_z F_y + c_z \dot{R}_z^2\right) + m\dot{h}_z\dot{R}_z - F_y\right) \quad (4.18)$$

It is interesting to note the relationship between the lateral and vertical components of the constraint force. This relationship, for this simplified wheel model, clearly shows that these two reaction components are not independent since they are related by an algebraic equation. This should be the case because the contact constraint conditions reduce to one algebraic equation that relates the generalized coordinates of the wheel. Therefore, if the L and V measured are interpreted as the reaction forces at the contact point, one must keep in mind that these force components are not independent when the simple wheel climb scenario discussed in this section is considered. These important and new results, obtained using the simplified model, are compared against the general fully nonlinear unconstrained MBS model results at the climb initiation. If a

more complex climb scenario is considered, the governing kinematic equations must be developed in order to have a better understanding of the relationship between the reaction forces at the contact point.

4.2.6.3 Solution Algorithm for the Simplified Semi-Analytical Model

In this subsection, the computational algorithm used to solve the wheel differential/algebraic equations of the simplified model is summarized. Note that a positive AOA corresponds to a negative value of the angle ψ. Note also that in the case of a constant AOA and zero roll, the degrees of freedom of the wheel model considered in this investigation are R_x, R_z, and θ. Nonetheless, one needs to determine s^w in order to be able to determine the location of the contact point on the wheel as well as the absolute velocity of this point. The steps of the numerical algorithm used in this investigation to determine the solution of the simplified model equations can be summarized as follows:

1. Given the AOA α, degrees of freedom R_x, R_z, and θ, and their derivatives $\dot{R}_x, \dot{R}_z$, and $\dot{\theta}$, the algebraic constraint equations of 4.4 can be solved for R_y and s^w. The parameter s^w can be used to determine the location of the contact point as shown by Eq. 4.3.
2. The constraint equations at the velocity level (time derivative of Eq. 4.4) can be solved for $\dot{R}_y$ and $\dot{s}^w$. The time derivative of $\mathbf{R}$ and the angular velocity $\boldsymbol{\omega}$ can be used to determine the absolute velocity of the contact point using the equation $\mathbf{v}_P = \dot{\mathbf{r}}_P = \dot{\mathbf{R}} + \boldsymbol{\omega} \times \mathbf{u}_P$, where the vectors used in this equation are as previously defined in this chapter.

3. Knowing all the coordinates and velocities, $h_z, \dot{h}_z$, and c_z can be calculated.
4. Given the external forces, the equations of motion of Eq. 4.13 can be formulated and solved for the accelerations $\ddot{R}_x, \ddot{R}_z$, and $\ddot{\theta}$. These accelerations can be integrated forward in time to determine the degrees of freedom R_x, R_z, and θ, and their derivatives $\dot{R}_x, \dot{R}_z$, and $\dot{\theta}$.
5. If the end of the simulation time is not reached, the previous steps are repeated.

The computational algorithm outlined above is used in this investigation to obtain the numerical results for the simple wheel model.

4.2.6.4 Distance to Climb

It is shown in Eq. 4.13 that the longitudinal motion R_x of the wheel is completely decoupled from the vertical motion R_z. In the case of friction, sliding in the longitudinal direction can produce a friction force that in turns creates a moment on the wheel. This moment, in the case of sliding and large lateral force, can have an effect on the wheel rotation which in turn has an effect on the velocity of the contact point. However, it is clear from Eq. 4.13, that there is no direct relationship between R_x and R_z, which is also the case when the AOA is allowed to vary. Consequently, the use of the distance to climb in some of the existing derailment criteria needs to be investigated. In the case of curved tracks, the effect of the distance to climb needs to be investigated using a three-dimensional analysis that is not based on the planar Nadal's formula.

4.3 Numerical Comparative Study

The results of the two different models developed in this investigation, the fully nonlinear unconstrained MBS model and the simplified semi-analytical model, are compared in this section. The comparison shows a good agreement in the vicinity of the climb initiation. The motion of the semi-analytical model is numerically investigated in this section using the solution algorithm described in the preceding section, while the results of the general MBS system model are obtained using a general MBS algorithm. The numerical results obtained are used to examine the motion of the wheel during derailment and to shed light on the contributors to the wheel climb phenomenon. Such an analysis allows one to call into question the validity of the use of derailment criteria such as the Nadal L/V Limit.

The analysis provided below will show that the lateral and vertical reaction forces exerted by the rail onto the wheel are coupled due to the kinematic condition that is developed as the wheel flange comes into contact with the rail. This kinematic condition in turn results in a loss of a degree of freedom of the wheel, which is shown to contribute to the climb initiation. The friction forces, which are also developed when the wheel flange comes into contact with the rail at a relative velocity, are shown to have non-zero components in three Cartesian directions with respect to the rail. The friction force, in combination with the normal force, is often measured at the wheel/rail interface. The analysis presented in this investigation, however, demonstrates that the measured forces are not representative of the applied force that drives the climb of the wheel. It then follows that such forces are not adequate for developing derailment prevention criteria, and therefore, the use of derailment criteria such as the Nadal L/V Limit is investigated and shown to not be a conservative measure of derailment initiation.

The results of the semi-analytical model yield multiple contributions. Because the lateral and vertical components of the reaction force can be related by an algebraic expression that is independent of the applied force, the measurement of one component can lead to the calculation of the other. The results shown in this section are contrary to the current interpretation of wheel climb initiation, which claim that the saturation of the friction force provides sufficient vertical force to develop wheel climb. Nonetheless, the forces involved in the derailment are shown to be three-dimensional, which should eliminate the rationale of using any planar force analysis in the case of wheel climb. Furthermore, the Nadal L/V Limit is currently interpreted as a conservative limit in the prediction of wheel climb derailments, which now must be questioned as the results show otherwise using analytical and computational models. The results of the fully nonlinear MBS model are also used to demonstrate that the semi-analytical model properly captures the climb *initiation* phenomena. It is understood that the forces that produce climb initiation are different from the forces that sustain the wheel climb through derailment. It is also understood that the results of the semi-analytical model will deviate from the results of the MBS model as the climb propagates from climb initiation; this difference is attributed to the motion constraints and geometric simplifications that are employed in order to develop a closed-form expression of the climb initiation.

4.3.1 Model Parameters

In this section, the semi-analytical model is discussed and the parameters used as input to the numerical analysis are given. The model in question is a geometric simplification of a wheel flange in contact with a tangent rail section while oriented at a large AOA, as shown in Fig. 4.17. The

model geometry and coordinates are shown in Fig. 4.18. The model input parameters required to perform the simulation are given in Table 4.4.

Initial Conditions		Wheel Properties		Input
$R_x = 0$ m	$\dot{R}_x = 5$ m/s	$m = 1568$ kg	$I_{xx} = 656$ kg.m^2	$\alpha = 50$ mrad
$R_z = 0.4699$ m	$\dot{R}_z = 0$ m/s	$r = 0.4737$ m	$I_{xx} = 168$ kg.m^2	$y_c = 0$ m
$\theta = 0$ rad	$\dot{\theta} = 10.4339$ rad/s	$\mu = 0.5000$	$I_{zz} = 656$ kg.m^2	$z_c = 0$ m

Table 4.4. Semi-Analytical Disk/Rail Model Input

In order to drive the climb of the wheel, an absolute lateral force is applied to the wheel center of mass that is equal in magnitude to the weight of the wheel. For simplicity, the numerical results of the semi-analytical model will be referred to in figures as *SAM*, while the numerical results of the multibody system model will be referred to as *MBS*.

4.3.2 Wheelset Motion

The lateral displacement of the wheelset, for both the semi-analytical model and the MBS model, are shown in Fig. 4.19.

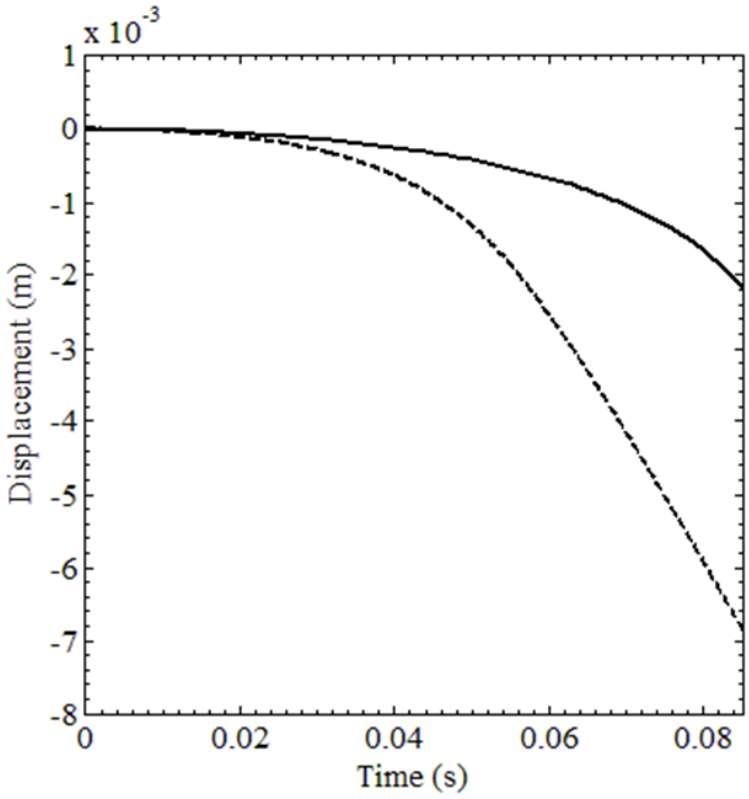

Figure 4.19. Wheelset Lateral Displacement

(——— SAM, – – – – MBS)

The plot demonstrates that under the application of the lateral force, the lateral distance between the wheelset and the rail decreases. The vertical displacement of the wheelset is shown in Fig. 4.20; it is clear that for a lateral motion for the simulation scenario considered in this chapter, the wheelset is required to undergo subsequent vertical motion as well.

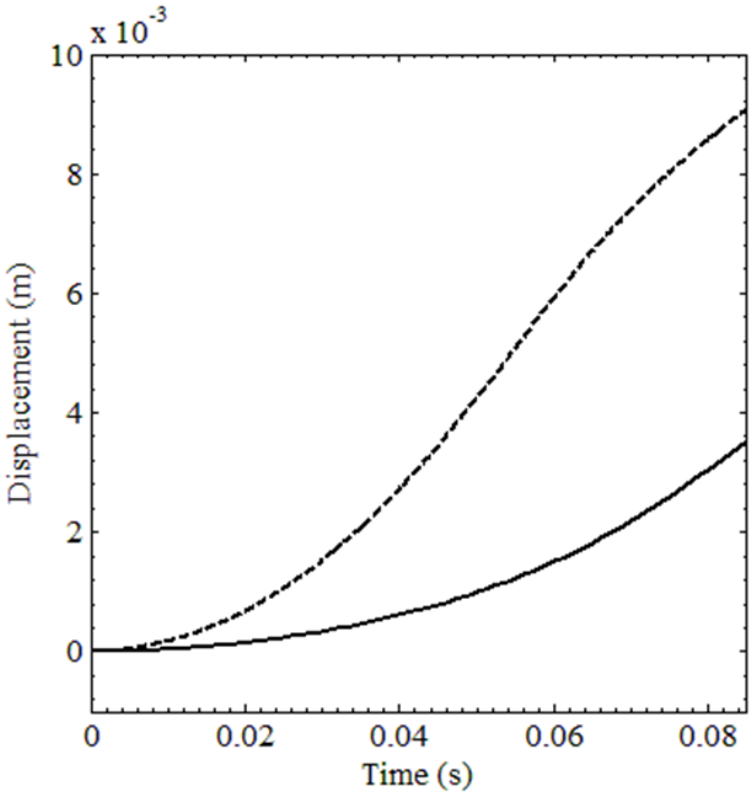

Figure 4.20. Wheelset Vertical Displacement

(——— SAM, – – – – MBS)

This is the result of the loss of the degree of freedom resulting from the kinematic constraint that is developed when the wheel flange comes into contact with the rail. The wheelset will climb to derailment in a shorter period of time if the applied lateral force increases; climb may also occur very quickly and without dependence on vehicle motion history thus creating a dangerous derailment scenario.

4.3.3 Three-Dimensional Climb Scenario

The components of the friction force developed at the wheel flange are shown in Fig. 4.21.

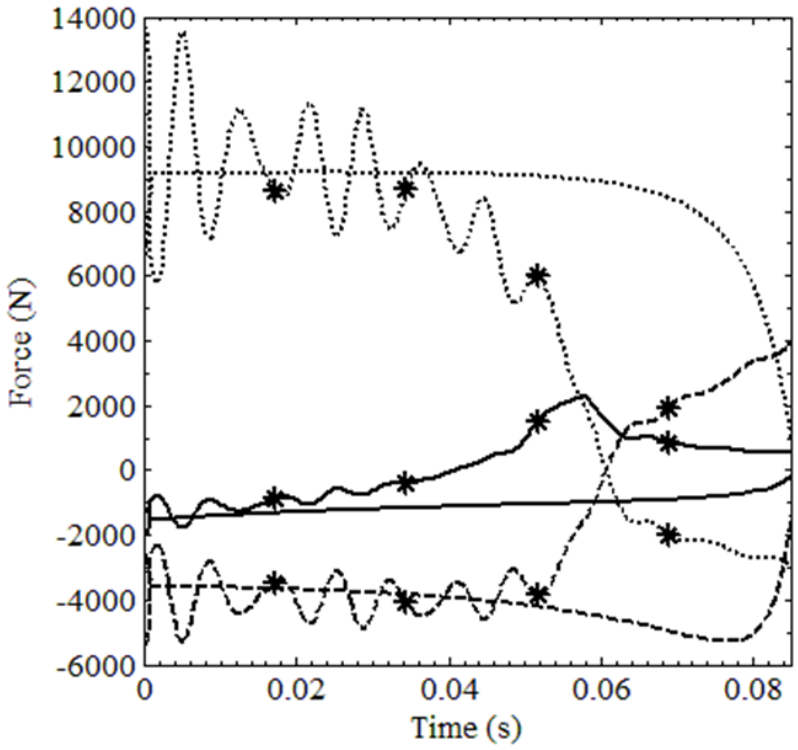

Figure 4.21. Flange Friction Components

(——— X, – – – – Y, ------- Z, * MBS)

It is clear from this figure that the friction force is not directed purely downward, but instead has, in general, three non-zero components in the three Cartesian directions with respect to the rail. This three-dimensionality can be attributed to the AOA of the wheelset. Consequently, the forces

developed during wheel climb cannot be captured using two dimensional analysis. Additionally, attempting to model the friction between the wheel and the rail as two dimensional will result in an incorrect magnitude.

4.3.4 Lubrication and Pure Kinematic Climb

It is worthy of mention that the wheel may climb without the influence of any friction components, leading to a purely kinematic derailment. The loss of the degree of freedom that is created when the wheel flange comes into contact with the rail then plays a significant role and should not be neglected. Under sufficient lateral force, the wheel will displace laterally which in turn requires vertical climb, regardless of the lubrication of the wheel flange. It should then not be misconceived that vertical friction forces are exclusively responsible for wheel climb derailments.

4.3.5 Kinematic Contribution

Kinematic constraints, which are introduced by the wheel/rail contact, restrict the wheelset motion to certain directions during a climb scenario and must be understood. Under the application of lateral force, friction forces as well as reaction forces will be developed at the point of contact. To understand the importance of the kinematic contribution to the climb of the wheelset, it becomes convenient to define a *kinematic contribution measure* (KCM) as the ratio of the vertical component of the reaction force applied at the flange to the total contact forces acting upwards at the flange, represented as a percentage. The KCM allows one to see the impact of the constraint during the climb of the wheel. Figure 4.22 shows this ratio as the wheel climbs the rail for the semi-analytical and MBS models.

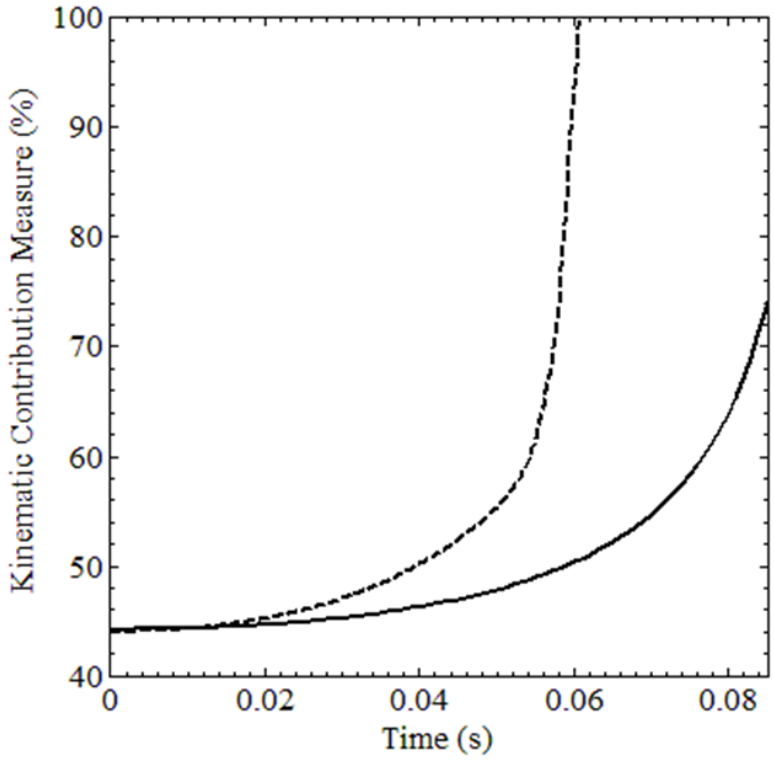

Figure 4.22. Kinematic Contribution Measure

(——— SAM, – – – –MBS)

It is clear from this figure that the kinematic contribution is significant during the climb initiation, and becomes even more significant as the wheel climbs the rail.

4.3.6 Lateral Force Relationship

An applied lateral force to the wheelset can drive the wheel flange into the rail, causing derailment. It is incorrect to assume, however, that the forces measured at the contact point generally balance the forces that drive the derailment. Figure 4.23 shows the ratio of the lateral force developed at the contact point to the applied lateral force acting on the wheel.

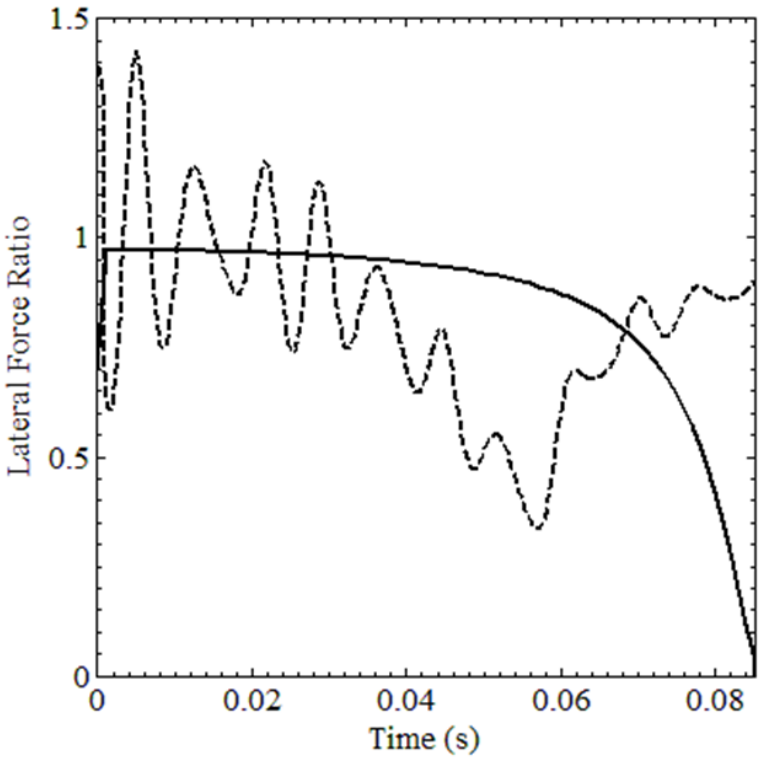

Figure 4.23. Lateral Force Ratio

(——— SAM, – – – – MBS)

The lateral contact force is, in general, different from the lateral applied force. Because these forces are not representative of one another for the semi-analytical or MBS models, similar investigations may need to be considered in railroad vehicle derailment studies that rely heavily on the forces developed at the wheel/rail interface to predict motion.

4.3.7 The Nadal L/V Limit

Figure 4.24 shows the L/V of the flange contact forces for the semi-analytical and MBS models.

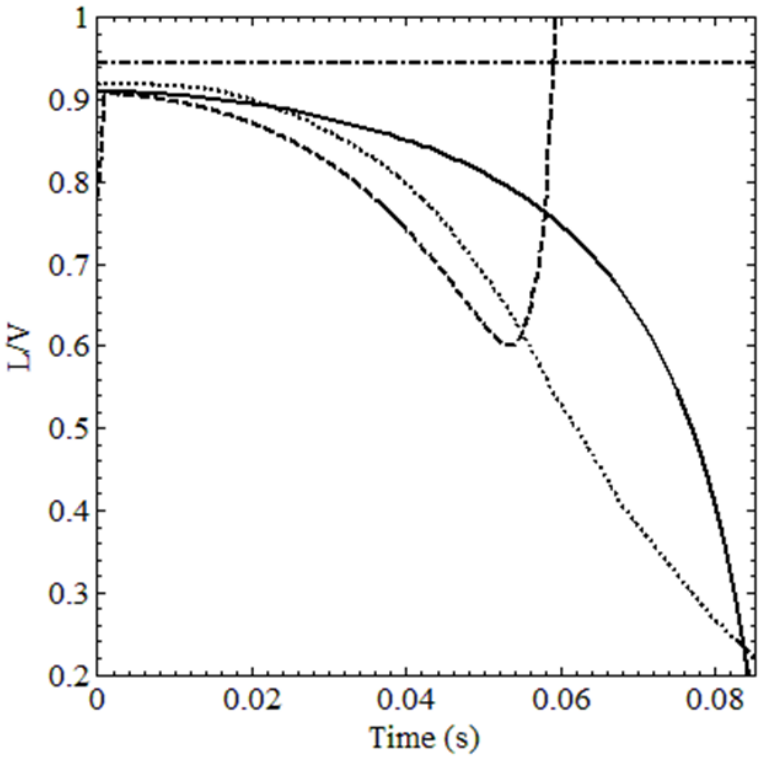

Figure 4.24. Measured L/V vs. Derailment Criteria

(——— SAM, – – – – MBS, ... Updated Nadal, – · – · – Max Nadal)

As the wheel climb propagates, the L/V of the two models actually *decrease* as the danger of derailment becomes more prevalent. This phenomenon is contrary to the belief that the L/V will increase until a critical value is exceeded. The critical value of the Nadal equation, updated at each time step with the proper flange angle at the point of contact, is also shown in Fig. 4.24 to decrease as the climb propagates. It can be seen that the climb of the two wheelset models initiates at measured L/V values that are below that of the Nadal L/V Limit, indicating that the derailment criteria may not be, then, referred to as *conservative*. Also included in Fig. 4.24 is the Nadal L/V limit using the maximum flange angle, which is even less conservative.

4.3.8 Comments on Model Simplification

It is clear that the semi-analytical model can be considered as a useful tool for understanding the conditions at which wheel climb initiates, as well as understanding the physical principles that are at play during a climb scenario. The results of the semi-analytical model diverge as the climb propagates as expected since the semi-analytical model does not take into account the geometry of the wheel and rail profiles, and makes assumptions on the motion of the wheelset. The trends of the MBS model results were represented by the semi-analytical model in the vicinity of the climb initiation, and therefore, the simplified model has potential as a tool for understanding basic derailment concepts, particularly in the vicinity of the climb initiation. The validation of any new concepts, however, will require the use of fully nonlinear MBS models as it is done in this chapter.

4.4. Fully Nonlinear MBS Counter Example

The MBS model examined in this chapter is considered in this section in order to rationalize the use of the contact angle in derailment criteria.

The L/V force ratio measured at the wheel flange/rail interface is shown in Fig. 4.25.

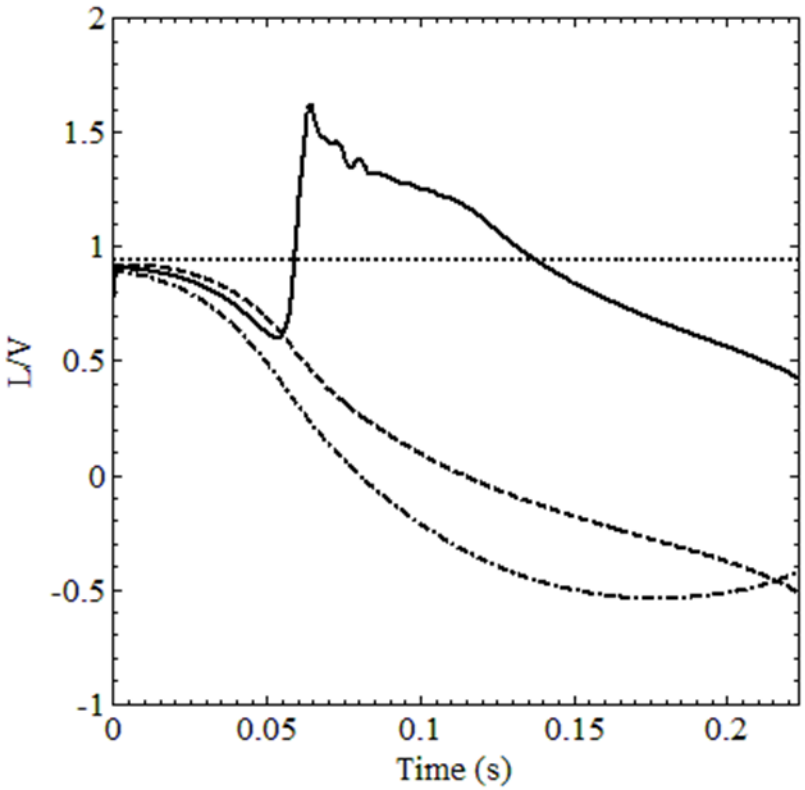

Figure 4.25. Wheel Flange L/V

(_____Measured, - - - - - -Updated Nadal, ... Max Nadal, - . - . - . -Updated Criteria)

The ratio decreases for approximately the first 50 ms of the derailment, where the ratio increases sharply then continues to decrease. Also shown in the figure is the "updated Nadal" derailment limit, where the limit is recalculated at each time step for the current flange angle. It is realized from the figure that the derailment initiates at a L/V ratio less than the limit predicted by Nadal's criteria. The Nadal limit is also shown to decrease as the risk of derailment becomes more prevalent. The *maximum Nadal* derailment limit, where the maximum flange angle is used in the calculation, is also shown as a horizontal reference line. It is seen from the figure that this derailment limit is even less conservative. Finally, an "updated criteria" is shown in Fig. 4.25, which is calculated by substituting the *contact angle* (discussed in chapter 3) for the *flange angle* in the Nadal formula such that

$$L/V = \left(\tan\delta - \mu\right)/\left(1+\mu\tan\delta\right) \tag{4.19}$$

This criteria is shown to accurately predict the derailment that Nadal's original formulation was unable to predict. This result does not justify the use of such a criteria, as it was shown in this chapter that the forces developed in wheel climb derailments cannot be captured by planar analysis; however it does rationalize the use of the contact angle in derailment investigations as well as shed light on the miscalculation that can be made through assuming the flange angle is representative of the contact angle.

4.5 Concluding Remarks

There is a strong belief in the rail industry and research community that wheel climb at a large AOA is initiated by friction forces. It is believed that when the wheel comes into flange contact with the rail at a large AOA, an increase in the lateral force acting on the wheel leads to an increase

in the normal reaction force at the flange contact point. Since in this case the contact point on the wheel is moving downward, the large reaction force normal to the flange produces significant upward friction force that results in wheel climb. A fully nonlinear MBS wheel climb model is used in this study in order to investigate the above interpretation of wheel climb derailments.

The results obtained using this numerical model are analyzed in order to shed light on the forces that contribute to the wheel climb mechanism. It is shown that the contact between the wheel flange and rail introduces motion constraints that play a significant role in the initiation of the climb, and become more significant as the wheel climbs the rail. In addition to the reaction forces, the contact between the wheel flange and rail produces a friction force that is shown to have non-zero components in three Cartesian directions with respect to the rail and therefore cannot be captured using any planar analysis. It follows that the Nadal L/V Limit, which makes use of a planar force balance, does not correctly capture the friction force at the flange. This investigation also demonstrates that the forces measured at the flanging rail are not representative of the force that drives the derailment. The above conclusions raise question to the current state of derailment criteria, and in particular the Nadal L/V Limit, which is shown to not predict the derailment presented in this investigation. The criteria may then not be deemed conservative.

These important conclusions are further investigated using a semi-analytical model that is additionally formulated in this investigation. The semi-analytical model is formulated using assumptions that are derived from the current interpretation of wheel climb in order to analyze the *initiation* of the wheel climb motion and the initiation only. The results of the semi-analytical model are compared with the results of the MBS model in order to validate the assumptions made to develop the semi-analytical model as well as provide insight into the derailment initiation of the

MBS model. The two models, although very different in formulation, are in good agreement in the vicinity of the wheel climb initiation. The semi-analytical formulation raises question in regards to use of the "distance to climb" measure used in some derailment criteria, as it is shown that the longitudinal motion is decoupled from the vertical and yaw displacements.

The results of both models confirm the following important conclusions:

1. Nadal's limit cannot be used as the basis for a conservative derailment criterion.
2. The ratio of the lateral force to the vertical force, L/V, decreases as the wheel continues to climb.
3. Wheel climb can be initiated in the case of zero friction if the wheel is subjected to significant lateral force.

Finally, the correct *contact angle* was substituted into the formulation of the Nadal L/V derailment limit in order to provide an updated criterion that correctly predicted the derailment of the wheelset. This result should not be interpreted as an appropriate derailment measure, but rather, as a rationalization and justification of the use of the correct contact geometry in derailment investigations. These results support the need for the use of correct contact geometry in the investigations of the derailments of modern railroad systems.

CHAPTER 5

SUBSTRUCTURING AND CMS

Previously prepared in (O'Shea et al., 2016) and reproduced in this dissertation with permission which is listed in Appendix A. Dr. Paramsothy Jayakumar and David Mechergui are contributors.

The floating frame of reference (FFR) formulation is widely used in the analysis of deformable bodies in multibody system (MBS) simulations. The modeling of deformable bodies requires the use of elastic degrees of freedom, which can increase the model size significantly. Therefore, modal reduction techniques have been proposed in order to define a proper set of assumed body deformation modes at a preprocessing stage. Crucial to the proper definition of these modes when the finite element (FE) FFR formulation is used is the understanding of the concept of the reference conditions that define the nature of the deformable body coordinate system. Substructuring techniques, such as the Craig-Bampton method, on the other hand, have been proposed to allow for efficient model assembly and reduce model dimensionality. However, it is important to distinguish between substructuring techniques which aim at obtaining efficient model assembly and coordinate reduction and the reference conditions that define the problem to be solved. In this chapter, the appropriateness and generality of using the Craig-Bampton method in MBS implementation is discussed. It is shown that, when a set of reference conditions are not applied at a preprocessing stage, the Craig-Bampton transformation leads to the free-free modes of deformation as well as the natural frequencies associated with these modes. It is also shown that a square Craig-Bampton transformation is equivalent to a similarity transformation that does not alter the problem to be solved. Therefore, the goal of using the Craig-Bampton transformation is

not to improve the solution accuracy, but rather to obtain a reasonably accurate solution using lower dimension models, as with any other substructuring method. This chapter also demonstrates that free-free deformation modes cannot be used in all applications, shedding light on the importance of the concept of the reference conditions when using the FE/FFR formulation in modeling flexible bodies in MBS applications. To this end, this chapter demonstrates numerically for the first time that the unique resonance frequency of a model can be achieved using the definition of different mode shapes associated with different boundary conditions provided that the shapes are similar. Due to the subtleties inherent to the FFR formulation, care must be taken when using and/or designing flexible MBS software in order to obtain acceptable results.

5.1 Background

In rigid body dynamics, a body-fixed coordinate system located at the body center of mass is often used. In deformable body dynamics, on the other hand, the body coordinate system may or may not be rigidly attached to a point on the deformable body. Nonetheless, there should be no rigid body motion between the body and its coordinate system. This can be clearly explained using the simple example of the simply supported beam shown in Fig. 5.1.

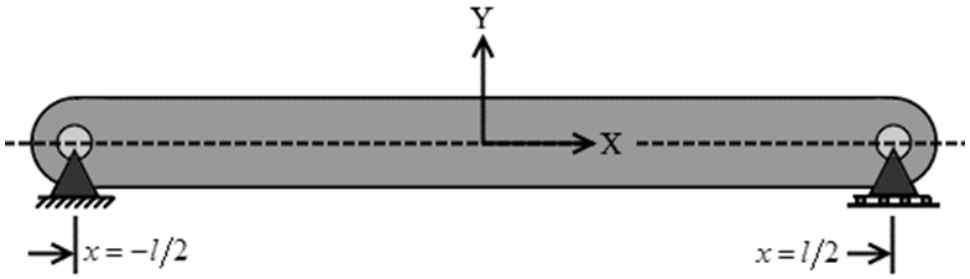

Figure 5.1. Simply-Supported Beam

If $u = u(x)$ and $v = v(x)$ are, respectively, the longitudinal extension/compression and transverse deflection of the beam and x is the longitudinal coordinate, the simply supported end conditions require that $u(x = -l/2) = 0, v(x = -l/2) = 0,$ and $v(x = l/2) = 0$. These three boundary conditions eliminate the rigid body motion of the beam and require that the X axis of the beam coordinate system shown in Fig. 5.1 must pass by the beam end points in order to ensure that the boundary condition algebraic equations are satisfied as the beam vibrates. It is clear from this simple example that as the beam vibrates the coordinate system does not move with a material point on the beam; this is the case of a *floating coordinate system*. Furthermore, the boundary conditions define the shape of the beam deflection which is described using the simply supported mode shapes. It is therefore important to understand the relationship between the boundary conditions, the body coordinate system, and the assumed shape of displacement. This relationship is fundamental when the FFR formulation is used in modeling flexible bodies that undergo finite rotations and are subjected to kinematic constraints. It will be demonstrated numerically in this

chapter that the reference conditions (boundary conditions) that eliminate the rigid body motion also define the shape of deformation. It will also be demonstrated that the unique resonance frequency of a model can be achieved using mode shapes obtained using different boundary conditions, provided that the shapes are similar.

In flexible MBS applications, deformable bodies undergo finite rotations and are subjected to kinematic constraints that describe mechanical joints. One of the most fundamental problems when the FFR formulation is used in flexible MBS application is the selection of the deformable body coordinate system and the selection of the assumed shape of deformation. In the FFR formulation, an FE mesh is developed at a preprocessing stage in order to determine the inertia shape integrals that enter into the formulation of the nonlinear mass matrix and the Coriolis and centrifugal forces (Shabana, 2013). These inertia shape integrals as well as the stiffness matrix can be expressed in their modal form in order to allow for using coordinate reduction techniques. When the FE mesh is created at a preprocessing stage, boundary conditions can be introduced in order to define the *deformation vector space* as well as the deformable body coordinate system. In order to explain this fundamental problem, consider the slider-crank mechanism shown in Fig. 5.2a. The figure shows a dotted line that represents a possible deflection shape of the flexible connecting rod of the mechanism. The deflected flexible connecting rod is shown in Fig. 5.2b.

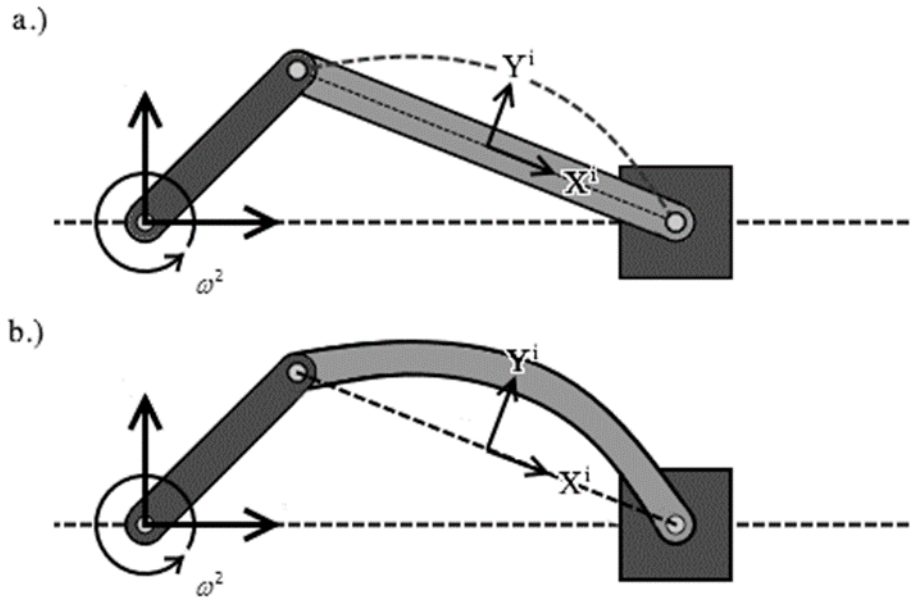

Figure 5.2. Slider-Crank Mechanism with Elastic Connecting Rod

In reality, coordinate systems do not exist and they are introduced for the convenience of measuring the deformation or other physical variables. There are an infinite number of choices for the coordinate system of the connecting rod. Some of these different choices are associated with different reference conditions. Figure 5.3 shows three possible choices of the connecting rod coordinate system. The first choice, Fig. 5.3a, can be defined using reference conditions (boundary conditions) similar to the case of the simply supported beam considered previously in this section. That is, if this coordinate system is to be selected, one must impose boundary conditions of a simply supported beam when the FE mesh is created at the preprocessing stage. This choice will automatically define the assumed shape of the deflected connecting rod. Other choices are the

body-fixed coordinate system shown in Fig. 5.3b, and the mean axis coordinate system shown in Fig. 5.3c.

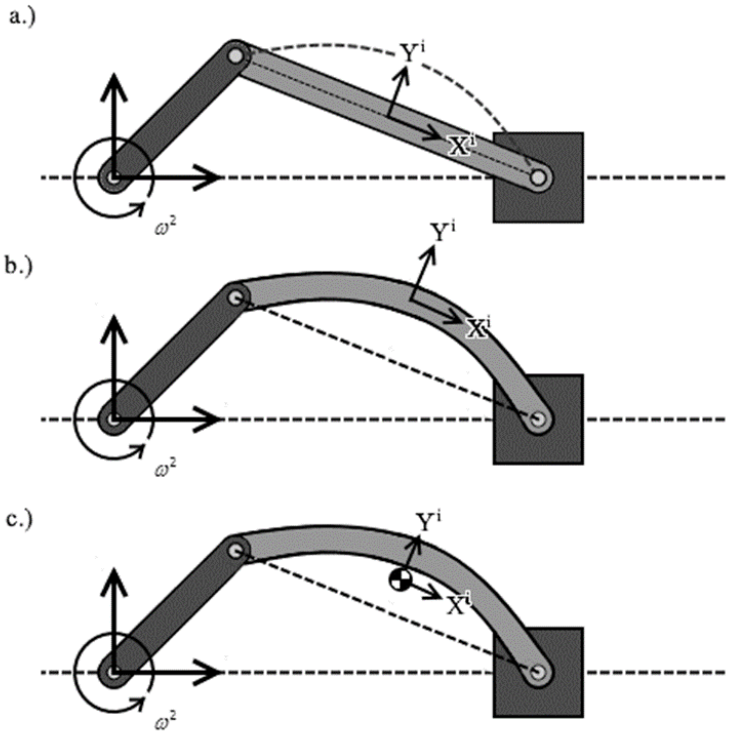

Figure 5.3. Simply-Supported, Body-Fixed, and Mean-Axis Reference Conditions

The body-fixed coordinate system can be obtained by imposing the three conditions $u(x=0)=0, v(x=0)=0$, and $\partial v/\partial x(x=0)=0$, which are equivalent to the clamped boundary conditions at the center of the beam. The mean axis conditions, on the other hand, correspond to

the case of free-free end conditions. The resulting mode shapes are the free-free mode shapes as discussed in the literature (Ashley, 1967; and Agrawal and Shabana, 1985). One can show that these three different choices in the selection of the reference conditions lead to assumed modes with similar shapes, despite the fact that the natural frequencies of the linear problem of the three cases can be significantly different. This important issue will be revisited in a later section of this chapter.

The slider-crank mechanism example clearly explains the fundamental relationship between the assumed mode shapes and the selection of the body coordinate system. It also demonstrates clearly that the deformation is relative and should not be viewed as absolute. For the same deformable body and same deformed shape, in one coordinate system the deformation can assume a very large value, while in another coordinate system the deformation can assume a very small or zero value. That is, the definition of the deformation lacks uniqueness. For this reason, in continuum mechanics texts, strains are used as deformation measures since the strains at a point and along certain directions are unique. The uniqueness of the strains is the result of the uniqueness of the position vector gradients that represent tangents to coordinate lines (fibers).

The reference conditions, therefore, define a problem which has a unique solution. In the case of complex structures, different substructuring techniques can be used to obtain an efficient solution that converges to the unique solution. The reference conditions define the deformation vector space, while substructuring techniques are not intended to change this deformation vector space. Rather, the substructuring techniques use a subset of the vectors that span this space and provide an efficient method for the model assembly.

5.2 FE/FFR Reference Conditions

In order to have a general implementation of the FE/FFR formulation, it is necessary to have a good understanding of the concept of the reference conditions that define the nature of the flexible body coordinate system and also define the mode shapes that describe the body deformation with respect to its coordinate system. In this section, this concept is reviewed briefly in order to better understand the implementation of substructuring techniques in flexible MBS algorithms. To this end, a brief review of the FE/FFR formulation is provided.

5.2.1 FE/FFR Kinematics

The displacement field of a deformable body can be approximated using the conventional finite elements that employ infinitesimal rotations as nodal coordinates. However, inherent in the element shape functions are rigid body modes. The linearized rotations used as nodal coordinates in the finite element method are not suitable for arbitrary rigid body motion. Therefore, the displacement of the body is represented by the motion of a selected body reference. The deformation of the body is then defined with respect to the body reference using a set of reference conditions. For simplicity, the case of planar motion is considered in this section.

In the FE/FFR formulation, the displacement field across an element j of deformable body i is defined in an element coordinate system $X^{ij}Y^{ij}$ as $\mathbf{w}^{ij} = \mathbf{S}^{ij}\mathbf{e}^{ij}$, where $\mathbf{S}^{ij}$ is the element shape function matrix, and $\mathbf{e}^{ij}$ is the vector of element nodal coordinates. Figure 5.4 shows the coordinates of a planar Euler-Bernoulli beam element.

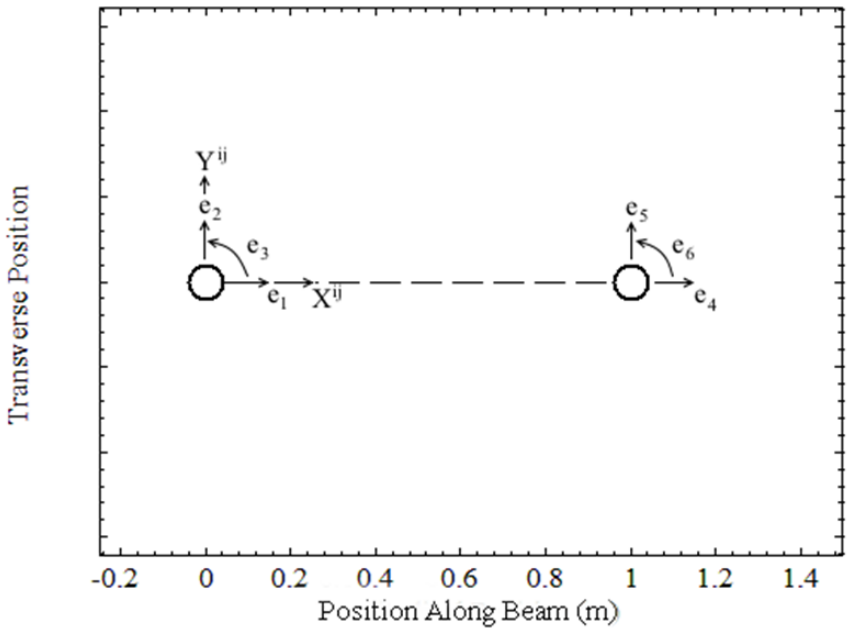

Figure 5.4. Euler-Bernoulli Beam Nodal Coordinates

(○ Original nodal position, ---------- Undeformed element)

Figure 5.5 shows the shape functions of the left node of this element, while Fig. 5.6 shows the shape functions of the right node of this element, which has total of six nodal coordinates $e_k^{ij}, k = 1, 2, \ldots, 6$.

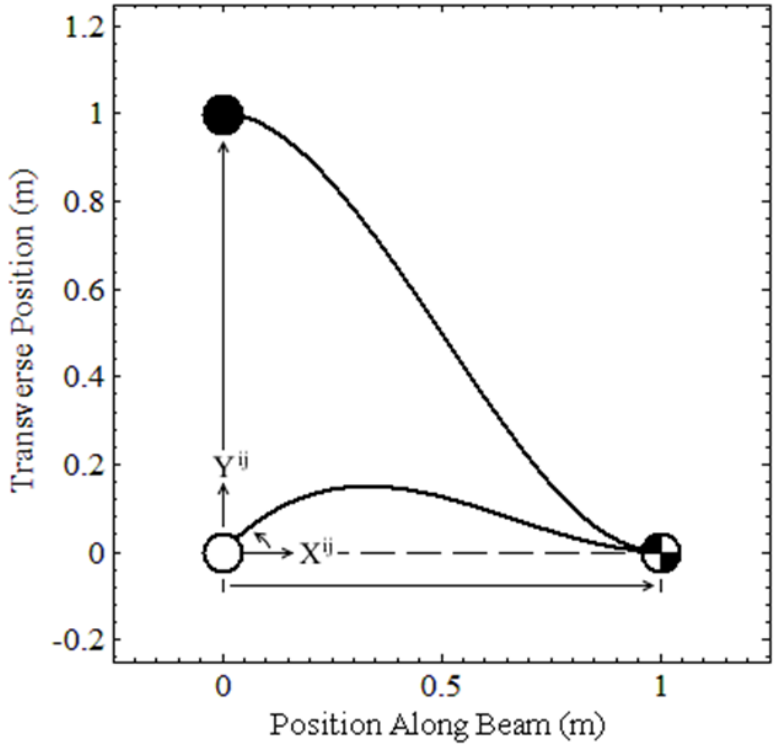

Figure 5.5. Euler-Bernoulli Beam Left Node Shape Functions

(○ Original nodal position, ● Displaced nodal position, ◓ Overlapped original/displaced node)

(---------- Undeformed element, ———— Deformed element)

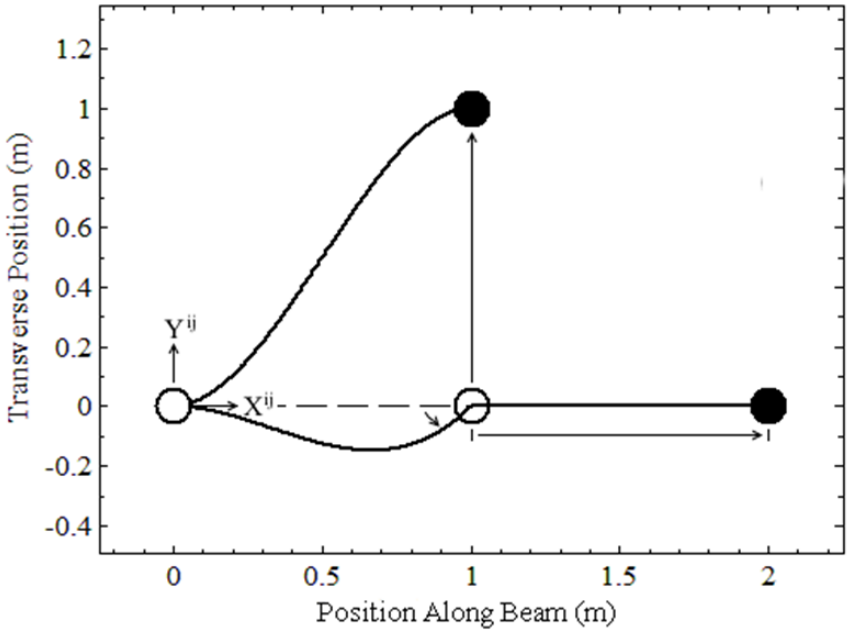

Figure 5.6. Euler-Bernoulli Beam Right Node Shape Functions

(○ Original nodal position, ● Displaced nodal position)

(---------- Undeformed element, ——— Deformed element)

In order to meet convergence requirements, the displacement field across an element must be continuous. Also, the element must be able to assume the state of constant strain. To this end, the rigid body modes must exist in the element shape functions. For example, as shown in Fig. 5.7 for the planar Euler-Bernoulli beam element, a transverse rigid body mode can be produced with nodal coordinates $\mathbf{e}^{ij} = \begin{bmatrix} 0 & 1 & 0 & 0 & 1 & 0 \end{bmatrix}^T$.

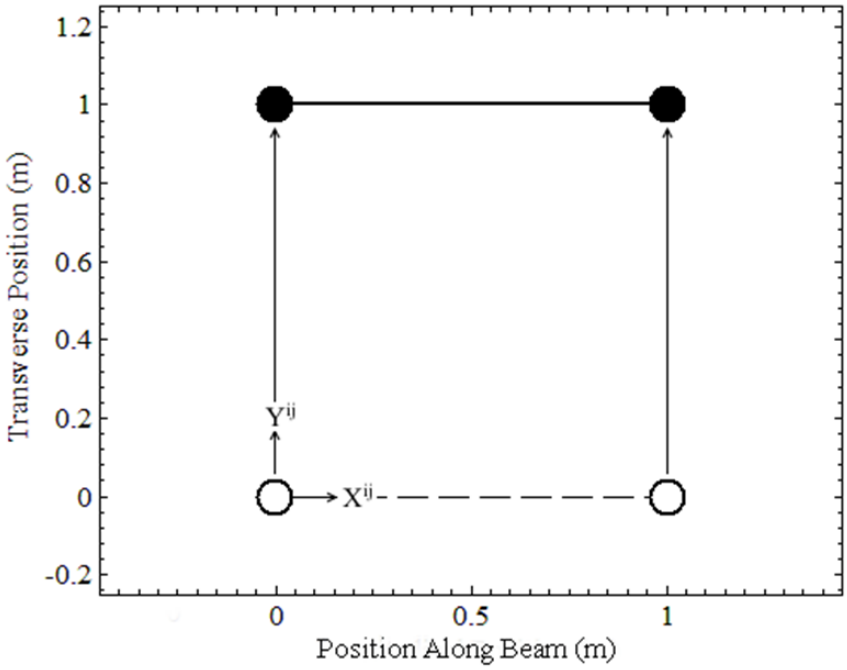

Figure 5.7. Euler-Bernoulli Beam Transverse Rigid Body Mode

(○ Original nodal position, ● Displaced nodal position)

(---------- Undeformed element, ——— Deformed element)

5.2.2 Coordinate Systems

The shape functions of conventional structural finite elements such as beams, plates, and shells cannot accurately describe arbitrary rigid body rotations (Shabana, 1996; Shabana, 2013). This is the result of using infinitesimal rotations as nodal coordinates. The FE/FFR formulation was introduced to allow using conventional structural finite elements and avoid using incremental rotation solution procedures in MBS simulations. In this formulation, a body coordinate system $X^iY^iZ^i$ is introduced to describe the large displacements including finite rotations of the FE mesh with respect to an absolute reference XYZ. An intermediate element coordinate (IEC) system

$X_i^{ij} Y_i^{ij} Z_i^{ij}$ is also introduced in order to be able to describe complex geometries characterized by discontinuities common in automotive and machine applications. The origin of the IEC system is rigidly fixed to the origin of the body coordinate system. The axes of the IEC system are oriented such that they are initially parallel to the element coordinate system axes as shown in Fig. 5.8.

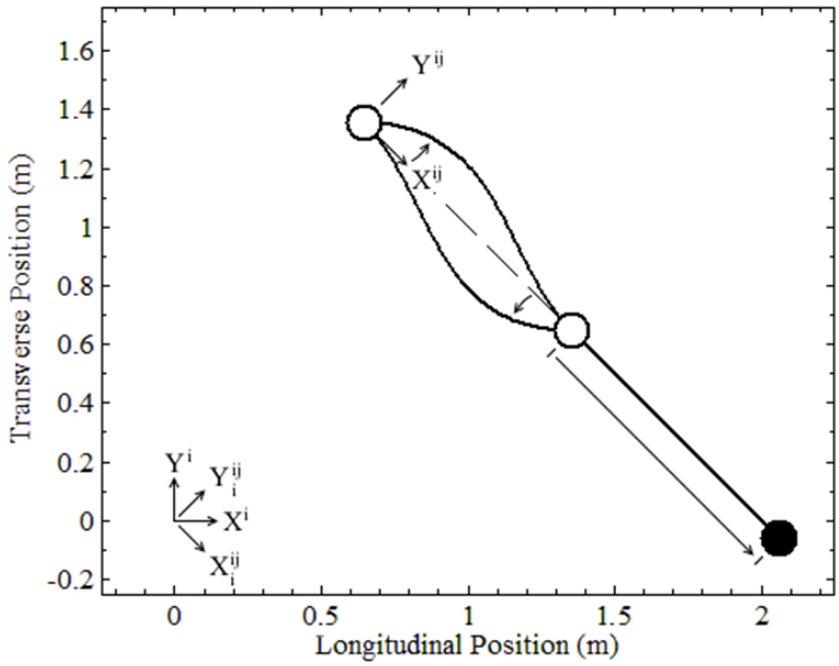

Figure 5.8. Simply-Supported Reference Conditions in the FFR Formulation

(○ Original nodal position, ● Displaced nodal position)

(---------- Undeformed element, ——— Deformed element)

(Body Reference $X^i Y^i Z^i$, IECS Reference $X_i^{ij} Y_i^{ij} Z_i^{ij}$, Element Reference $X^{ij} Y^{ij} Z^{ij}$)

Since the FE shape function can describe arbitrarily large translation, a new definition for the displacement field in the IEC system is $\mathbf{w}_i^{ij} = \mathbf{S}^{ij} \mathbf{e}_i^{ij}$, where the vector of nodal coordinates $\mathbf{e}^{ij}$ is

replaced by a new coordinate vector $\mathbf{e}_i^{ij}$. A constant transformation exists between the IEC system and the body reference. This relation can be written as $\mathbf{e}_i^{ij} = \bar{\mathbf{C}}^{ij}\mathbf{q}_n^{ij}$, where the matrix $\bar{\mathbf{C}}^{ij}$ is a constant transformation matrix, and the vector $\mathbf{q}_n^{ij}$ represents the nodal coordinates defined in the body coordinate system (Shabana, 2013).

5.2.3 Reference Conditions

To define a unique displacement field in which the body large displacement is represented by the motion of the body coordinate system, the rigid body modes must be eliminated from the element shape functions. To this end, one can write the vector $\mathbf{q}_n^{ij}$ as the sum of two vectors such that $\mathbf{q}_n^{ij} = \mathbf{q}_0^{ij} + \bar{\mathbf{q}}_f^{ij}$, where $\mathbf{q}_0^{ij}$ represents a constant vector of the undeformed nodal coordinates, and $\bar{\mathbf{q}}_f^{ij}$ represents the vector of nodal displacements. These coordinates are shown in Fig. 5.9 for the right node of the Euler-Bernoulli beam element.

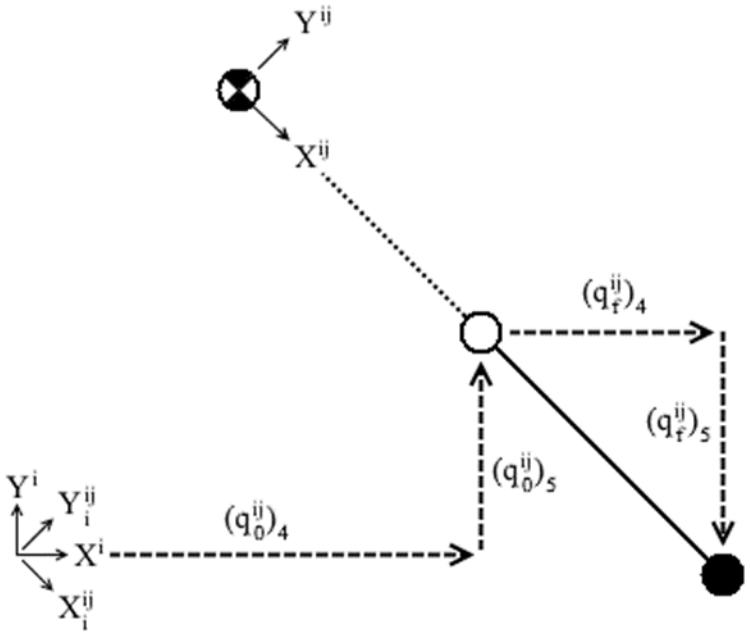

Figure 5.9. Right Nodal Coordinates Defined in Body Reference Frame

(○ Original nodal position, ● Displaced nodal position, ◓ Overlapped original/displaced node)

(····· Undeformed element, ——— Deformed element)

Using a standard FE assembly process, one can write $\mathbf{q}_n^i = \mathbf{q}_0^i + \bar{\mathbf{q}}_f^i$, where $\mathbf{q}_n^{ij} = \mathbf{B}_1^{ij}\mathbf{q}_n^i$, and $\mathbf{B}_1^{ij}$ is a Boolean matrix that defines the element coordinates in the body coordinate vector. It follows that $\bar{\mathbf{q}}_f^{ij} = \mathbf{B}_1^{ij}\bar{\mathbf{q}}_f^i$. In order to eliminate the rigid body modes of the element shape functions, a set of reference conditions similar to the boundary conditions must be imposed on the deformation coordinates of the body. The resulting linear algebraic equations can be used to define dependent deformation coordinates that can be expressed in terms of the independent deformation coordinates. This leads to the transformation $\bar{\mathbf{q}}_f^i = \mathbf{B}_2^i\mathbf{q}_f^i$, where $\mathbf{B}_2^i$ is the matrix of reference

conditions, and $\mathbf{q}_f^i$ is the vector of independent nodal deformations. Using the FE/FFR kinematic equations developed in this section, one can write the position vector of an arbitrary point p on the finite element j in the coordinate system of body i

$$\mathbf{r}_p^{ij} = \mathbf{R}^i + \mathbf{A}^i \bar{\mathbf{u}}_p^{ij} = \mathbf{R}^i + \mathbf{A}^i \mathbf{C}^{ij} \mathbf{S}_p^{ij} \bar{\mathbf{C}}^{ij} \mathbf{B}_1^i \left(\mathbf{q}_0^i + \mathbf{B}_2^i \mathbf{q}_f^i \right) \tag{5.1}$$

where $\bar{\mathbf{u}}_p^{ij} = \mathbf{C}^{ij} \mathbf{S}_p^{ij} \bar{\mathbf{C}}^{ij} \mathbf{B}_1^{ij} \left(\mathbf{q}_0^i + \mathbf{B}_2^i \mathbf{q}_f^i \right)$, $\mathbf{S}_p^{ij}$ is the element shape function evaluated at the arbitrary point p , $\mathbf{C}^{ij}$ is the matrix that defines the orientation of the IEC system with respect to the body coordinate system, $\mathbf{R}^i$ is the vector that defines the global position of the origin of the body coordinate system origin, and $\mathbf{A}^i$ is the transformation matrix that defines the orientation of the body coordinate system in the global system (Shabana, 2013). A case of a special interest in the discussion that will be presented in this chapter is the case in which $\mathbf{B}_2^i$ is the identity matrix, that is $\mathbf{B}_2^i = \mathbf{I}$, which is the case of free-free boundary conditions that defines a body coordinate system that satisfies the mean axis conditions (Ashley 1967; Agrawal and Shabana, 1985)

5.2.4 FE/FFR Equations of Motion

Using the FE/FFR kinematic description presented in this section, the equations of motion can obtained using Eq. 5.1 and the principle of virtual work or Lagrange's equation as

$$\begin{bmatrix} \mathbf{m}_{rr}^i & \mathbf{m}_{rf}^i \\ \mathbf{m}_{fr}^i & \mathbf{m}_{ff}^i \end{bmatrix} \begin{bmatrix} \ddot{\mathbf{q}}_r^i \\ \ddot{\mathbf{q}}_f^i \end{bmatrix} + \begin{bmatrix} \mathbf{0} & \mathbf{0} \\ \mathbf{0} & \mathbf{k}_{ff}^i \end{bmatrix} \begin{bmatrix} \mathbf{q}_r^i \\ \mathbf{q}_f^i \end{bmatrix} = \begin{bmatrix} \left(\mathbf{Q}_e^i \right)_r \\ \left(\mathbf{Q}_e^i \right)_f \end{bmatrix} + \begin{bmatrix} \left(\mathbf{Q}_v^i \right)_r \\ \left(\mathbf{Q}_v^i \right)_f \end{bmatrix} + \begin{bmatrix} \left(\mathbf{Q}_c^i \right)_r \\ \left(\mathbf{Q}_c^i \right)_f \end{bmatrix} \tag{5.2}$$

In this equation, subscripts r and f refer, respectively, to reference and elastic coordinates, $\mathbf{q}_r^i$ and $\mathbf{q}_f^i$ are, respectively, the reference and elastic coordinates, $\mathbf{k}_{ff}^i$ is the stiffness matrix, and $\mathbf{Q}_e^i, \mathbf{Q}_v^i$, and $\mathbf{Q}_c^i$ are, respectively, the vector of external, Coriolis and centrifugal, and constraint forces. If the reference conditions eliminate all the rigid body modes of the element shape function, the stiffness matrix $\mathbf{k}_{ff}^i$ is positive definite. If, on the other hand, free-free end conditions are used, the stiffness matrix $\mathbf{k}_{ff}^i$ is a semi-definite matrix.

5.2.5 Use of Component Modes

Using the preceding equation, the free vibration of the body with respect to its reference is defined by the equation $\mathbf{m}_{ff}^i \ddot{\mathbf{q}}_f^i + \mathbf{k}_{ff}^i \mathbf{q}_f^i = \mathbf{0}$. This equation can be used to define the generalized eigenvalue problem $\mathbf{k}_{ff}^i \mathbf{a}^i = \left(\omega^i\right)^2 \mathbf{m}_{ff}^i \mathbf{a}^i$, where $\left(\omega^i\right)^2$ is the eigenvalue and $\mathbf{a}^i$ is the eigenvector. The eigenvalue problem can be solved for a set of eigenvectors $\mathbf{a}_l^i$ and the corresponding eigenvalues $\left(\omega_l^i\right)^2$, where l is the mode number. Using the eigenvectors (mode shapes), a coordinate transformation from the physical nodal coordinates to the modal elastic coordinates can be obtained as $\mathbf{q}_f^i = \bar{\mathbf{B}}_m^i \mathbf{p}_f^i$, where $\bar{\mathbf{B}}_m^i$ is the modal transformation matrix whose columns are the low-frequency mode shapes. The vector $\mathbf{p}_f^i$ is the vector of modal coordinates which represent the amplitudes of the mode shapes. The total deformation of the body is then represented by a linear combination of the low-frequency mode shapes. Using the modal transformation, the equations of motion can be written in its modal form as

$$\begin{bmatrix} \bar{\mathbf{m}}^i_{rr} & \bar{\mathbf{m}}^i_{rf} \\ \bar{\mathbf{m}}^i_{fr} & \bar{\mathbf{m}}^i_{ff} \end{bmatrix} \begin{bmatrix} \ddot{\mathbf{p}}^i_r \\ \ddot{\mathbf{p}}^i_f \end{bmatrix} + \begin{bmatrix} \mathbf{0} & \mathbf{0} \\ \mathbf{0} & \bar{\mathbf{k}}^i_{ff} \end{bmatrix} \begin{bmatrix} \ddot{\mathbf{p}}^i_r \\ \mathbf{p}^i_f \end{bmatrix} = \begin{bmatrix} \left(\bar{\mathbf{Q}}^i_e\right)_r \\ \left(\bar{\mathbf{Q}}^i_e\right)_f \end{bmatrix} + \begin{bmatrix} \left(\bar{\mathbf{Q}}^i_v\right)_r \\ \left(\bar{\mathbf{Q}}^i_v\right)_f \end{bmatrix} + \begin{bmatrix} \left(\bar{\mathbf{Q}}^i_c\right)_r \\ \left(\bar{\mathbf{Q}}^i_c\right)_f \end{bmatrix} \tag{5.3}$$

In this equation, a bar over a matrix or a vector indicates the modal form of the matrix or the vector, and $\mathbf{p}^i_r = \mathbf{q}^i_r$. The modal mass and stiffness matrices $\bar{\mathbf{m}}^i_{ff}$ and $\bar{\mathbf{k}}^i_{ff}$ are diagonal matrices. In the FFR formulation, it is recommended to perform an orthonormalization respect to the stiffness matrix $\mathbf{k}^i_{ff}$. This choice, which leads to identity modal stiffness matrix, that is $\bar{\mathbf{k}}^i_{ff} = \mathbf{I}$, provides a natural scaling of the elastic coordinates.

5.2.6 Reference Conditions and Substructuring Techniques

It is clear from the brief review presented in this section that the reference conditions, in addition to automatically defining the flexible body coordinate system, also define the mode shapes that describe the body deformation with respect to its coordinate system. The reference conditions can be selected to obtain the deformation shapes expected as the result of the loading conditions and kinematic constraints imposed on the boundary of the deformable bodies. The reference conditions also define a problem that has a unique solution. It is, therefore, important to distinguish between the reference conditions and substructuring techniques. The reference conditions, including the free-free end conditions associated with the mean axis conditions, define the deformation vector space. Substructuring techniques, which do not alter the problem and has no effect on the choice of the body coordinate system, are mainly used for the purpose of efficient model development and coordinate reduction. The step of imposing the reference conditions is indispensable in the FE/FFR formulation in order to properly define the problem and the flexible body coordinate

system. The FE/FFR formulation can be implemented in its most general form whether or not substructuring techniques are used.

5.3 The Craig-Bampton Method

The Craig-Bampton method is a substructuring technique that was introduced to allow for dividing large structures into smaller substructures, reduce the number of degrees of freedom of the substructures, and assemble the reduced-order substructure models in order to obtain an efficiently assembled and/or lower-dimension structure model. The solution obtained using the Craig-Bampton substructuring method is expected to converge to the solution of the original problem. Therefore, the Craig-Bampton substructuring method should lead to a solution that agrees with the solution obtained using other techniques including the conventional CMS methods. The Craig-Bampton method does not define a new problem, but aims at solving an existing one. This substructuring method is widely used in MBS software, and therefore, it is important to understand this method and its relationship to the reference conditions that define the deformation vector space. This section reviews the Craig-Bampton method (Bampton and Craig, 1968; Craig, 1983).

5.3.1 Craig-Bampton Transformation

As shown in the preceding section, the free vibration of the deformable body with respect to its reference is governed by the equation $\mathbf{m}^i_{ff}\ddot{\mathbf{q}}^i_f + \mathbf{k}^i_{ff}\mathbf{q}^i_f = \mathbf{0}$. One may partition the vector of elastic coordinates $\mathbf{q}^i_f$ into boundary coordinates $\left(\mathbf{q}^i_f\right)_b$ and internal coordinates $\left(\mathbf{q}^i_f\right)_i$ such that

$\mathbf{q}_f^i = \left[\left(\mathbf{q}_f^i\right)_b^T \quad \left(\mathbf{q}_f^i\right)_i^T \right]^T$, and rewrite the equation $\mathbf{m}_{ff}^i \ddot{\mathbf{q}}_f^i + \mathbf{k}_{ff}^i \mathbf{q}_f^i = \mathbf{0}$ using this coordinate partitioning as

$$\begin{bmatrix} \left(\mathbf{m}_{ff}^i\right)_{bb} & \left(\mathbf{m}_{ff}^i\right)_{bi} \\ \left(\mathbf{m}_{ff}^i\right)_{fb} & \left(\mathbf{m}_{ff}^i\right)_{ii} \end{bmatrix} \begin{bmatrix} \left(\ddot{\mathbf{q}}_f^i\right)_b \\ \left(\ddot{\mathbf{q}}_f^i\right)_i \end{bmatrix} + \begin{bmatrix} \left(\mathbf{k}_{ff}^i\right)_{bb} & \left(\mathbf{k}_{ff}^i\right)_{bi} \\ \left(\mathbf{k}_{ff}^i\right)_{fb} & \left(\mathbf{k}_{ff}^i\right)_{ii} \end{bmatrix} \begin{bmatrix} \left(\mathbf{q}_f^i\right)_b \\ \left(\mathbf{q}_f^i\right)_i \end{bmatrix} = \begin{bmatrix} \mathbf{0} \\ \mathbf{0} \end{bmatrix} \tag{5.4}$$

Using the second matrix equation in the preceding equation and ignoring the effect of the inertia forces, one obtains the equation

$$\left(\mathbf{k}_{ff}^i\right)_{ib} \left(\mathbf{q}_f^i\right)_b + \left(\mathbf{k}_{ff}^i\right)_{ii} \left(\mathbf{q}_f^i\right)_i = \mathbf{0} \tag{5.5}$$

Assuming that $\left(\mathbf{k}_{ff}^i\right)_{ii}$ is nonsingular, one can use the technique of static condensation to write the coordinates of the internal nodes in terms of the coordinates of the boundary nodes as

$$\left(\mathbf{q}_f^i\right)_i = -\left(\mathbf{k}_{ff}^i\right)_{ii}^{-1} \left(\mathbf{k}_{ff}^i\right)_{ib} \left(\mathbf{q}_f^i\right)_b = \boldsymbol{\Psi}_{ib}^i \left(\mathbf{q}_f^i\right)_b \tag{5.6}$$

In this equation, $\boldsymbol{\Psi}_{ib}^i = -\left(\mathbf{k}_{ff}^i\right)_{ii}^{-1} \left(\mathbf{k}_{ff}^i\right)_{ib}$. Using Eq. 5.6, one can define a coordinate transformation matrix that relates all the coordinates to the boundary coordinates, that is $\mathbf{q}_f^i = \boldsymbol{\Psi}_{fb}^i \left(\mathbf{q}_f^i\right)_b$, where the matrix $\boldsymbol{\Psi}_{fb}^i$ is defined as

$$\boldsymbol{\Psi}_{fb}^i \equiv \begin{bmatrix} \mathbf{I} \\ \boldsymbol{\Psi}_{ib}^i \end{bmatrix} = \begin{bmatrix} \mathbf{I} \\ -\left(\mathbf{k}_{ff}^i\right)_{ii}^{-1} \left(\mathbf{k}_{ff}^i\right)_{ib} \end{bmatrix} \tag{5.7}$$

Note that this transformation matrix is not a square matrix since it has a number of rows equal to the number of elastic coordinates $\mathbf{q}_f^i$ and a number of columns equal to the number of boundary coordinates $\left(\mathbf{q}_f^i\right)_b$. Note also that the column of the matrix $\boldsymbol{\Psi}_{ib}^i$ can be easily obtained since they

represent the change in the internal node coordinates as the result of a unit displacement in the boundary node coordinates. The columns of this matrix are referred to as the *static correction modes*.

In order to develop a square coordinate transformation, the second equation in Eq. 5.4 is used again by considering the case of free vibration of the internal nodes with respect to the boundary nodes. This leads to the equation $\left(\mathbf{m}_{ff}^{i}\right)_{ii}\left(\ddot{\mathbf{q}}_{f}^{i}\right)_{i}+\left(\mathbf{k}_{ff}^{i}\right)_{ii}\left(\mathbf{q}_{f}^{i}\right)_{i}=\mathbf{0}$. This equation can be used to define an eigenvalue problem that defines a number of eigenvectors equal to the number of the coordinates of the internal nodes. These eigenvectors define the columns of a modal transformation matrix $\mathbf{\Phi}_{ip}^{i}$. The new normal modes are called *fixed-interface modes*. Using this modal transformation matrix and the static correction modes, one obtains the following one-to-one coordinate transformation:

$$\mathbf{q}_{f}^{i}=\begin{bmatrix}\left(\mathbf{q}_{f}^{i}\right)_{b}\\ \left(\mathbf{q}_{f}^{i}\right)_{i}\end{bmatrix}=\begin{bmatrix}\mathbf{I} & \mathbf{0}\\ \mathbf{\Psi}_{ib}^{i} & \mathbf{\Phi}_{ip}^{i}\end{bmatrix}\begin{bmatrix}\mathbf{p}_{b}^{i}\\ \mathbf{p}_{f}^{i}\end{bmatrix}=\mathbf{\alpha}^{i}\mathbf{p}^{i} \tag{5.8}$$

In this equation, $\mathbf{p}_{b}^{i}=\left(\mathbf{q}_{f}^{i}\right)_{b}$, $\mathbf{p}_{f}^{i}$ is the vector of modal coordinates associated with the fixed-interface modes, and $\mathbf{\alpha}^{i}$ is the *Craig-Bampton transformation* defined as

$$\mathbf{\alpha}^{i}=\begin{bmatrix}\mathbf{I} & \mathbf{0}\\ \mathbf{\Psi}_{ib}^{i} & \mathbf{\Phi}_{ip}^{i}\end{bmatrix} \tag{5.9}$$

Since the number of internal degrees of freedom is normally much higher than the number of boundary degrees of freedom, insignificant fixed-interface modes can be eliminated, leading to a matrix $\mathbf{\Phi}_{ip}^{i}$ with small number of columns, thereby significantly reducing the number of

coordinates. Substituting Eq. 5.8 into the equation $\mathbf{m}_{ff}^{i}\ddot{\mathbf{q}}_{f}^{i}+\mathbf{k}_{ff}^{i}\mathbf{q}_{f}^{i}=\mathbf{0}$ that defines the free vibration of the deformable body with respect to its coordinate system and pre-multiplying by the transpose of the Craig-Bampton transformation $\boldsymbol{\alpha}^{i}$, one obtains

$$\left(\boldsymbol{\alpha}^{iT}\mathbf{m}_{ff}^{i}\boldsymbol{\alpha}^{i}\right)\ddot{\mathbf{q}}_{f}^{i}+\left(\boldsymbol{\alpha}^{iT}\mathbf{k}_{ff}^{i}\boldsymbol{\alpha}^{i}\right)\mathbf{q}_{f}^{i}=\mathbf{0} \tag{5.10}$$

Since the resulting mass and stiffness matrices $\left(\boldsymbol{\alpha}^{iT}\mathbf{m}_{ff}^{i}\boldsymbol{\alpha}^{i}\right)$ and $\left(\boldsymbol{\alpha}^{iT}\mathbf{k}_{ff}^{i}\boldsymbol{\alpha}^{i}\right)$ are not diagonal, existing MBS software use the preceding equation to solve for another eigenvalue problem in order to define diagonal modal mass and stiffness matrices.

5.3.2 Substructuring and Deformation Vector Space

As previously mentioned, it is important to distinguish between substructuring and the deformation vector space defined by the reference conditions. Before applying the transformation $\boldsymbol{\alpha}^{i}$ to the mass and stiffness matrices in the equation $\mathbf{m}_{ff}^{i}\ddot{\mathbf{q}}_{f}^{i}+\mathbf{k}_{ff}^{i}\mathbf{q}_{f}^{i}=\mathbf{0}$, one can still apply the reference conditions on the coordinates of the boundary nodes in order to define the deformable body coordinate system as well as the deformation vector space. If the number of reference conditions is larger than or equal to the number of rigid body modes of the finite element shape function, one obtains a positive definite stiffness matrix and the eigenvalue problem obtained using Eq. 5.10 does not lead to rigid body modes. If, on the other hand, no reference conditions are applied, the application of the transformation $\boldsymbol{\alpha}^{i}$ will lead to six rigid body modes in the spatial analysis. These rigid body modes can be eliminated with the understanding that the resulting deformable body coordinate system is a reference that satisfies the mean axis conditions, that is, this reference is a floating coordinate system that always remains at the structure center of mass which may not be a

material point as the structure deforms. The large displacement of this body reference is described in the FFR formulation using the absolute Cartesian coordinates and orientation parameters as previously discussed in this chapter.

5.3.3 Use in MBS Applications

If all the fixed interface modes are used, one has a square Craig-Bampton transformation that leads to the exact solution of the original problem since no coordinate reduction technique is used. If insignificant high frequency fixed-interface modes are neglected, the obtained solution is judged accurate if it converges to the solution of the original problem obtained using the square Craig-Bampton transformation. In the case of using a square Craig-Bampton transformation, one should obtain the same eigenvalues as the eigenvalues of the problem $\mathbf{m}_{ff}^{i}\mathbf{b}^{i} = \nu\mathbf{k}_{ff}^{i}\mathbf{b}^{i}$, where ν is the eigenvalue, and $\mathbf{b}^{i}$ is the eigenvector. That is, the two problems $\mathbf{m}_{ff}^{i}\mathbf{b}^{i} = \nu\mathbf{k}_{ff}^{i}\mathbf{b}^{i}$ and $\left(\boldsymbol{\alpha}^{iT}\mathbf{m}_{ff}^{i}\boldsymbol{\alpha}^{i}\right)\bar{\mathbf{b}}^{i} = \bar{\nu}\left(\boldsymbol{\alpha}^{iT}\mathbf{k}_{ff}^{i}\boldsymbol{\alpha}^{i}\right)\bar{\mathbf{b}}^{i}$ should have the same eigenvalues, that is $\nu = \bar{\nu}$, while the eigenvectors differ only by a coordinate transformation, that is $\mathbf{b}^{i} = \boldsymbol{\alpha}^{i}\bar{\mathbf{b}}^{i}$. If no reference conditions are imposed (case of mean axis conditions), one obtains the free-free mode shapes, regardless of the transformation used.

Some MBS computer programs that use the Craig-Bampton method allow for the use of the free-free modes only. It can be shown that if no reference conditions are defined, the stiffness matrices $\mathbf{k}_{ff}^{i}$ and $\left(\boldsymbol{\alpha}^{iT}\mathbf{k}_{ff}^{i}\boldsymbol{\alpha}^{i}\right)$ are semi-definite and the resulting mode shapes are the free-modes regardless of whether or not the Craig-Bampton transformation is used. It is important, however, to point out that the free-free modes, as will be demonstrated in this chapter, are not suited for the

use in many flexible MBS applications. Therefore, software that do not employ the concept of the reference conditions fail to exploit the generality of the FE/FFR formulation as it was originally proposed more than three decades ago, and the use of these software can be severely limited or can lead to wrong results as the result of not using the proper mode shapes that are suited for a particular application (Shabana, 1982).

5.4 Important Concept in Flexible Body Dynamics

In flexible body dynamics, it is important to understand that the mode shapes obtained as the result of imposing the reference conditions serve only the purpose of defining the deformation of the body with respect to its reference. That is, the natural frequencies obtained using a set of reference conditions applied to the structure at a preprocessing stage have no effect on the solution of the actual problem since what matters is the shape of deformation. Similar shapes can be obtained using different reference conditions that define different body coordinate systems. This is consistent with the fact of the non-uniqueness of the deformation as previously discussed in Section 5.1 of this chapter. This chapter demonstrates numerically for the first time this important concept.

To this end, the deflection of the slender steel beam shown in Fig. 5.10 is analyzed.

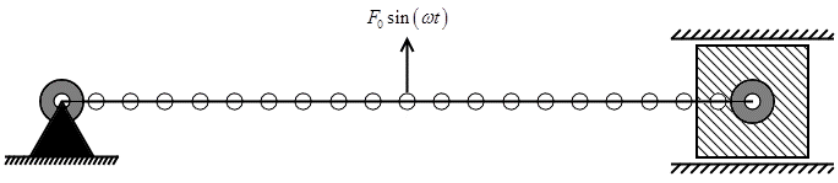

Figure 5.10. Simply-Supported Finite Element Beam under Actuated Load

(○ Original nodal position, ———— Undeformed element)

The MBS model is assumed to consist of three bodies including the ground, the beam, and a massless sliding block. The ground is assumed to be fixed in space. The beam is 0.3048 m in length, and is divided into 20 Euler-Bernoulli beam elements. The beam cross-section is circular with a 6.35 mm diameter. The elastic modulus is assumed to be 2.06843×10^{11} N/m^2. The free-free reference conditions that define a beam coordinate system whose origin remains at the beam center of mass are applied to the beam at a preprocessing stage. An eigenvalue analysis using the beam mass and stiffness matrices result in the free-free modes of vibration. Figure 5.11 shows the first six free-free modes resulting from this calculation.

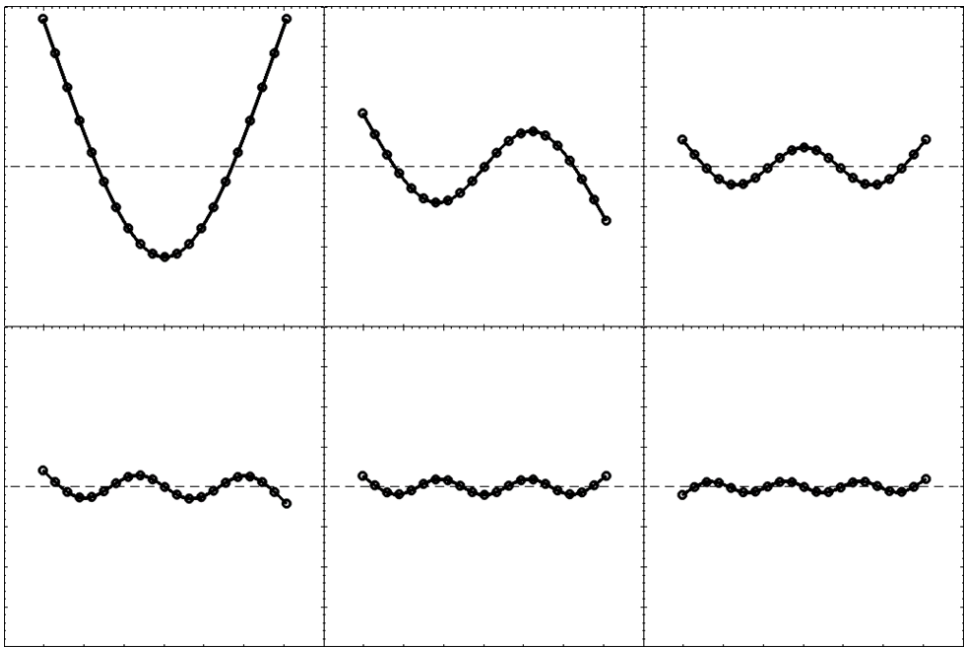

Figure 5.11. Free-Free Modes

(---------- Undeformed Beam Axis, ———— Deformed element)

(● Displaced nodal position)

Figure 5.12 shows the first six simply supported modes, for comparison. In the MBS model, the beam is pinned to the ground at its left end (node #1), and pinned to the sliding block at its right end (node #21).

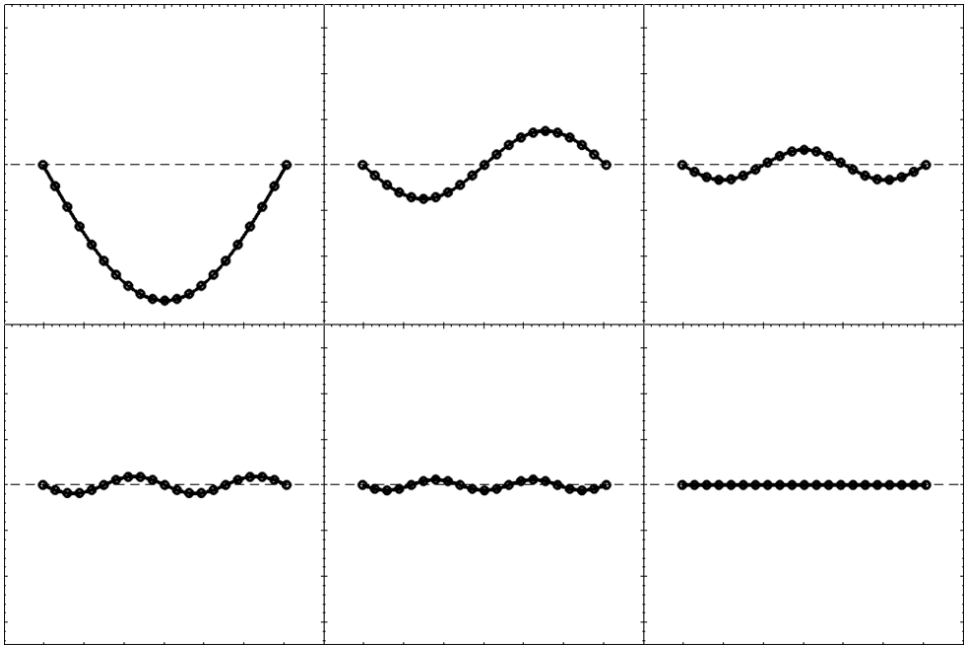

Figure 5.12. Simply-Supported Modes

(---------- Undeformed Beam Axis, ———— Deformed element)

(● Displaced nodal position)

A translational joint allows the sliding block to move in a lateral direction only, thereby physically defining simply supported end conditions. A sinusoidal force is applied by an actuator at the center of the beam (node #11) in the vertical direction. In this example, a parametric investigation is performed to study the maximum deflection of the beam center under various forcing frequencies

ranging from 15.9 Hz to 429.7 Hz. Figure 5.13 shows the largest deflection for each simulation scenario.

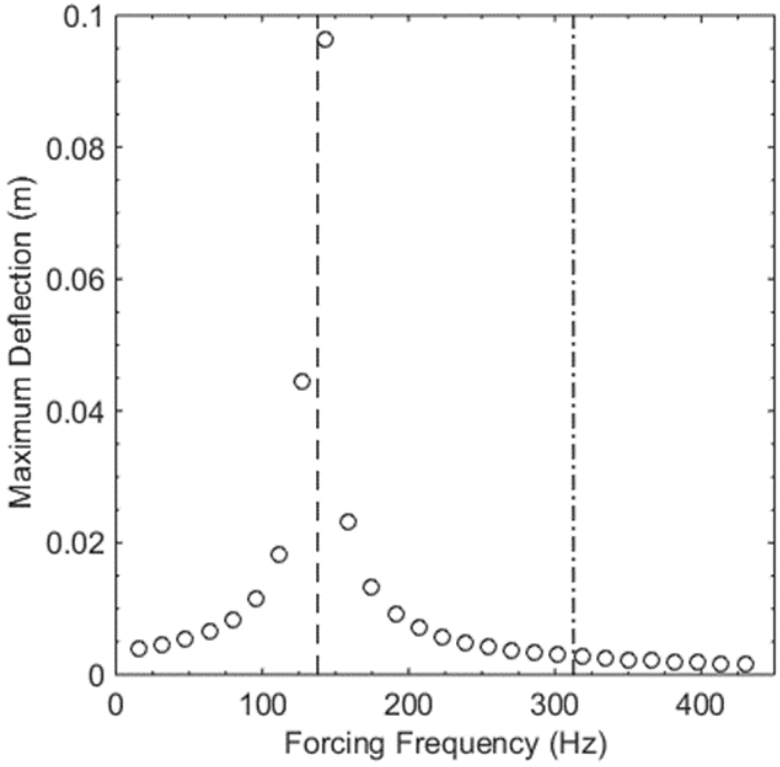

Figure 5.13. Maximum Deflection under Actuated Load using Free-Free Reference Conditions. (---------- Simply Supported Beam, -·-·-·-·-·- Free-Free Beam)

This figure also shows two vertical reference lines. The first reference line (~138 Hz) indicates the first natural frequency of a beam with simply-supported reference conditions. The second reference line (~312.5 Hz) indicates the first natural frequency of the beam with free-free reference

conditions. It is clear from this figure that the model achieves resonance for a forcing frequency equal to the simply-supported beam natural frequency despite the fact that free-free modes are used. That is, resonance is achieved not at the free-free natural frequency, but at the simply-supported natural frequency, implying that the natural frequencies obtained at the preprocessing stage have no effect on the solution of the problem.

As previously stated, the finite element method uses assumed shapes of deformation. To have an accurate solution, the shapes must represent the boundary conditions of the physical problem. This example demonstrates that it is the mode shapes, not the associated frequencies, which determine the solution accuracy. Although the free-free reference conditions have different natural frequencies than the simply supported reference conditions, the shapes are similar and this was the reason that the two different sets of reference conditions can produce similar results as demonstrated in the literature (Agrawal and Shabana, 1985). It is for this reason that resonance is seen at a forcing frequency equal to the natural frequency of the simply-supported beam, even though this frequency has no relationship to the natural frequency of the free-free beam. Numerical results show that the model does not produce resonance at the natural frequency of the free-free beam.

Even if Craig-Bampton substructuring method is used in MBS applications, the concepts discussed in this section remain fundamental and must be observed. In the remainder of this section, an example of the application of the Craig-Bampton method to the deformable beam of the previous example is considered. However, in this example, the beam is modeled using 6 Euler-Bernoulli beam elements in order to reduce the number of nodal degrees of freedom, for the

purpose of discussion only. Equation 5.7 gives the constraint modes for the beam, which are shown in Fig. 5.14.

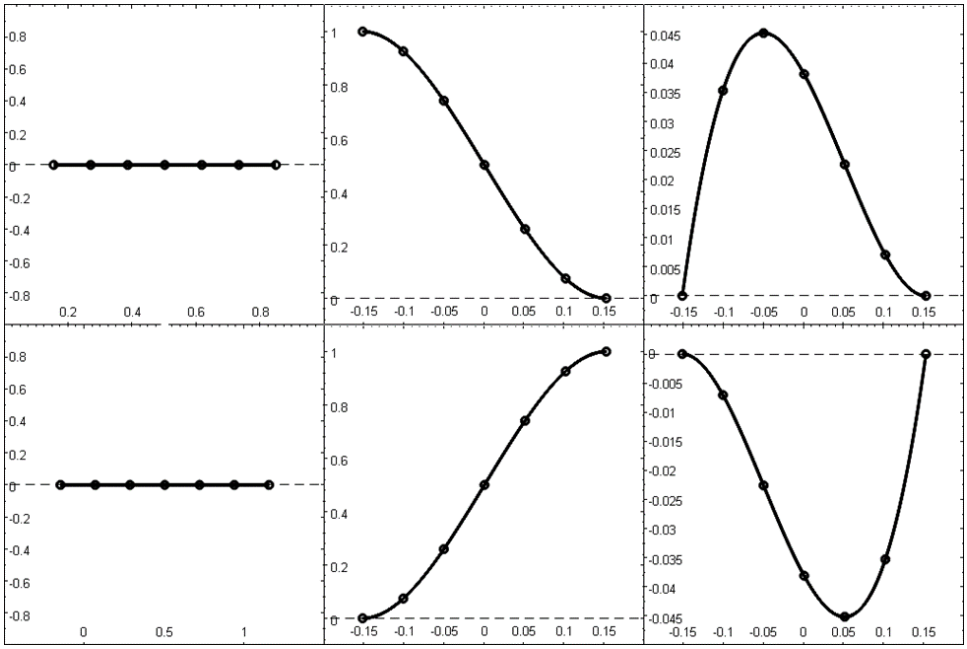

Figure 5.14. Constraint Modes

(---------- Undeformed Beam Axis, ———— Deformed element)

(● Displaced nodal position)

The columns of the matrix $\mathbf{\Phi}_{ip}^{i}$ of Eq. 5.8 are the fixed-interface normal modes. The first six fixed-interface normal modes are shown in Fig. 5.15 for visualization.

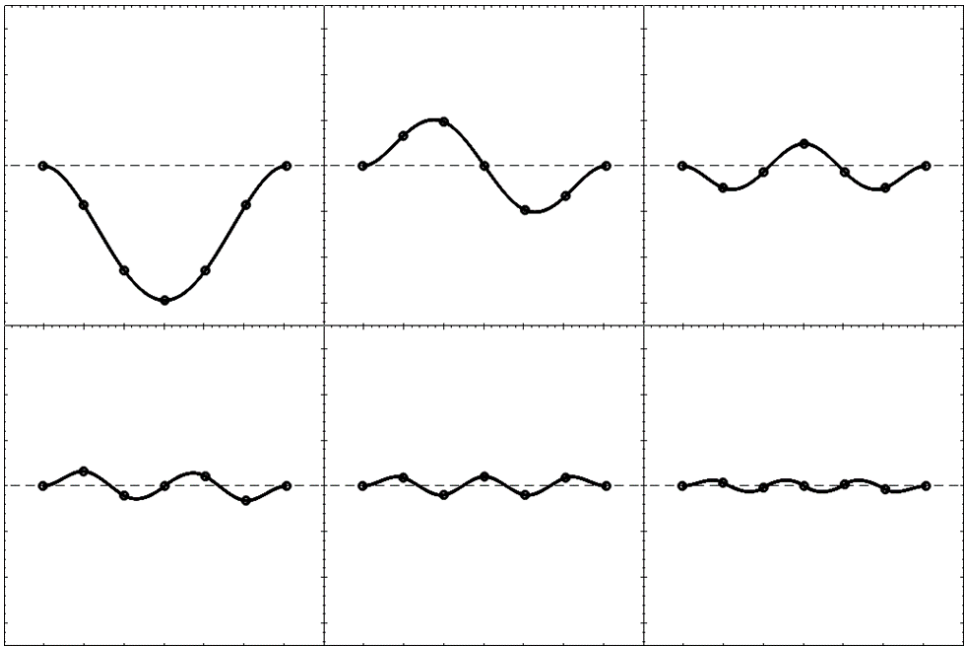

Figure 5.15. Fixed-Interface Normal Modes.

(---------- Undeformed Beam Axis, ——— Deformed element)

(● Displaced nodal position)

However, in this example, there may be up to fifteen fixed-interface normal modes which are all included to obtain the complete solution. The static correction and fixed-interface modes are combined to form the Craig-Bampton transformation as is given in Eq. 5.9. The beam mass and stiffness matrix are transformed according to the procedure described in the preceding section. Finally, an eigenvalue analysis is performed on the system, which is now written using a set of Craig-Bampton modal coordinates, resulting in a set of modes shown in Fig. 5.16.

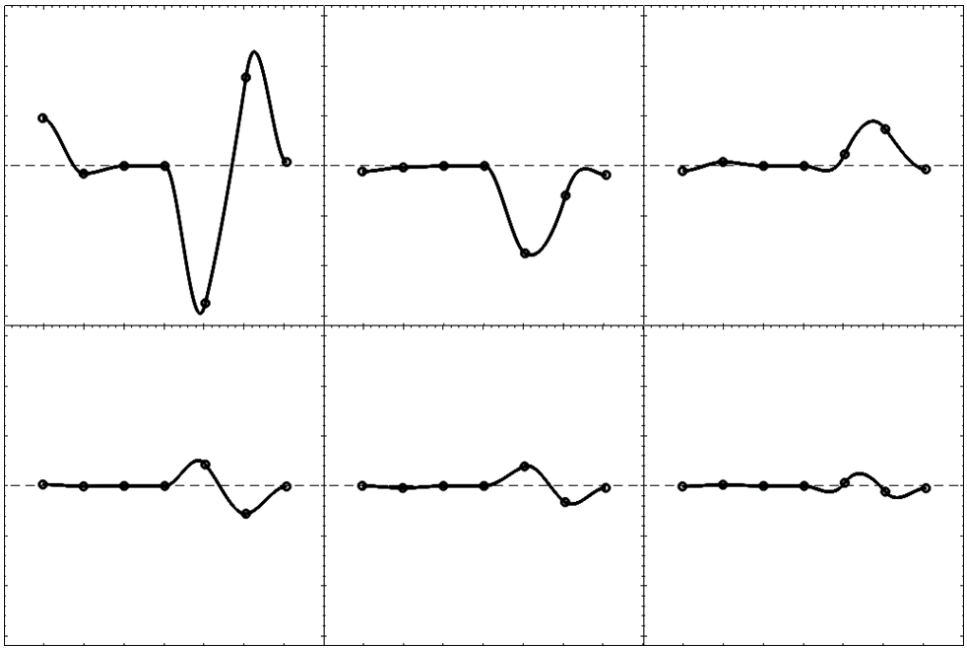

Figure 5.16. Modes Resulting from Eigenvalue Analysis of Craig-Bampton Equations of Motion
(---------- Undeformed Beam Axis, ——— Deformed element)
(● Displaced nodal position)

It is clear that the deflection shapes defined using this set of coordinates do not represent the deflection of the beam in a nodal coordinate space. Pre-multiplying the modes of Fig. 5.16 by the Craig-Bampton transformation yields a set of free-free normal modes. Figure 5.17 shows the first six free-free modes resulting from this calculation.

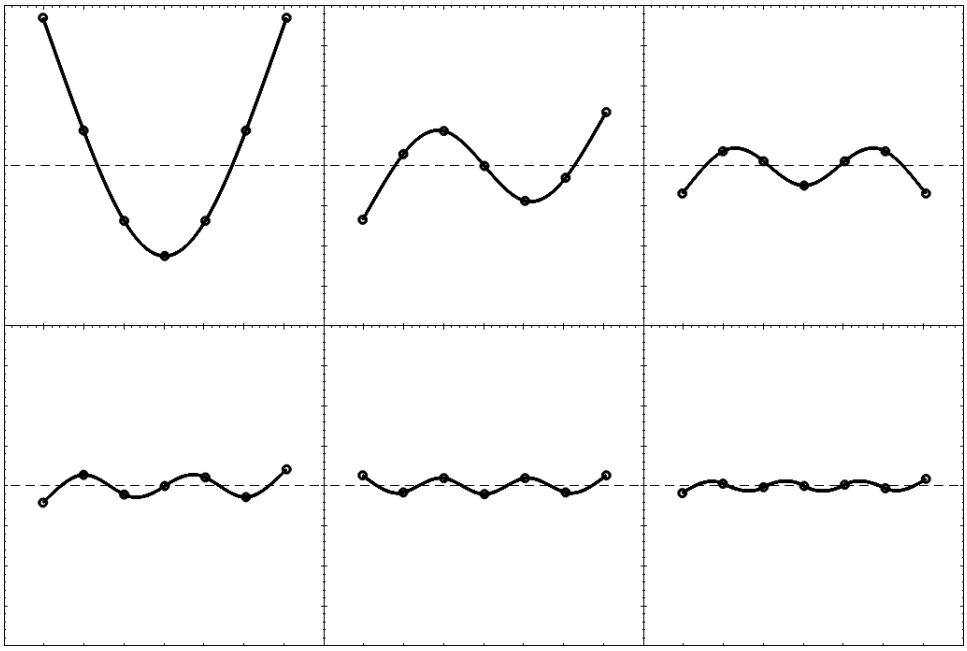

Figure 5.17. Resulting Free-Free Modes from Craig-Bampton Method

(---------- Undeformed Beam Axis, ——— Deformed element)

(● Displaced nodal position)

The frequencies associated with these modes are the frequencies associated with the free-free normal modes. Table 5.1 compares the first three natural frequencies against the respective analytical values.

Mode Order	Calculated Frequency (Hz)	Analytical Frequency (Hz)
1	312.7	312.6
2	863.3	861.8
3	1699.1	1689.5

Table 5.1. Beam Natural Frequencies

The error between the columns is small and is a result of the finite element approximation.

The finite element method makes use of assumed deformation shapes. These shapes are the result of the element shape functions that describe the element kinematics between nodal points. A square orthogonal transformation (as used in this example) will result in a change in the coordinates. But, this coordinate transformation does not change the original problem. The above example results in the free-free modes because, although the problem was solved using a set of Craig-Bampton coordinates, no algebraic equations were introduced to relate the nodal degrees of freedom. Such algebraic relations change the problem to be solved and the deformation vector space.

5.5. Appropriateness of Free-Free Modes for All MBS Applications

The answer to the question of whether or not the free-free modes are appropriate for applications is certainly negative. That is, the appropriate reference conditions must be used in order to obtain accurate solutions, as will be demonstrated in this section using simple slider-crank mechanism examples. The numerical study performed in this section will shed light on the serious limitation some MBS computer programs have when the boundary conditions are limited to the free-free mode shapes. To this end, two slider crank mechanism examples are used; one of them has an extended connecting rod.

5.5.1 Slider-Crank Mechanism Example

It has been shown in the previous examples that the mode shapes play a significant role in the accuracy of the physical problem, and that the Craig-Bampton method returns the free-free modes of vibration if no reference conditions are applied. This section demonstrates that the Craig-Bampton method will then yield accurate results in a case where free-free modes of vibration are appropriate. The beam of the previous examples is used as the elastic connecting rod in a slider-crank mechanism, as shown in Fig. 5.18.

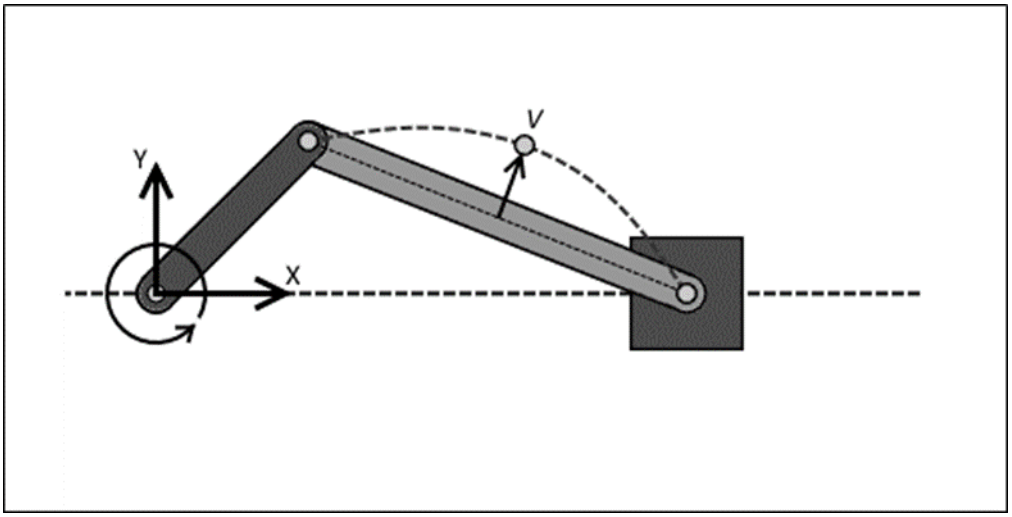

Figure 5.18. Slider-Crank Mechanism

However, in this example, the beam is modeled using 2 Euler-Bernoulli beam elements for simplicity. A pin joint connects the crankshaft to the ground. The crankshaft rotates about that joint with a constant angular velocity equal to 124 rad/s. A pin joint also connects the connecting rod and massless slider-block. A translational joint restricts the slider-block to lateral motion only.

The parameter of interest is the dimensionless deflection V of the beam center. This parameter is found by dividing the deflection of the beam center by the length of the beam.

The simulation is performed using two different computer programs. The first program (MBS-REF) uses a general modal analysis and takes into account the reference conditions discussed in this chapter. The second program (MBS-CB) uses the Craig-Bampton method. Figure 5.19 shows the dimensionless deflection of the beam center for the two simulations. Figure 5.19 also shows an analytical solution to the problem given by (Chu and Pan, 1975).

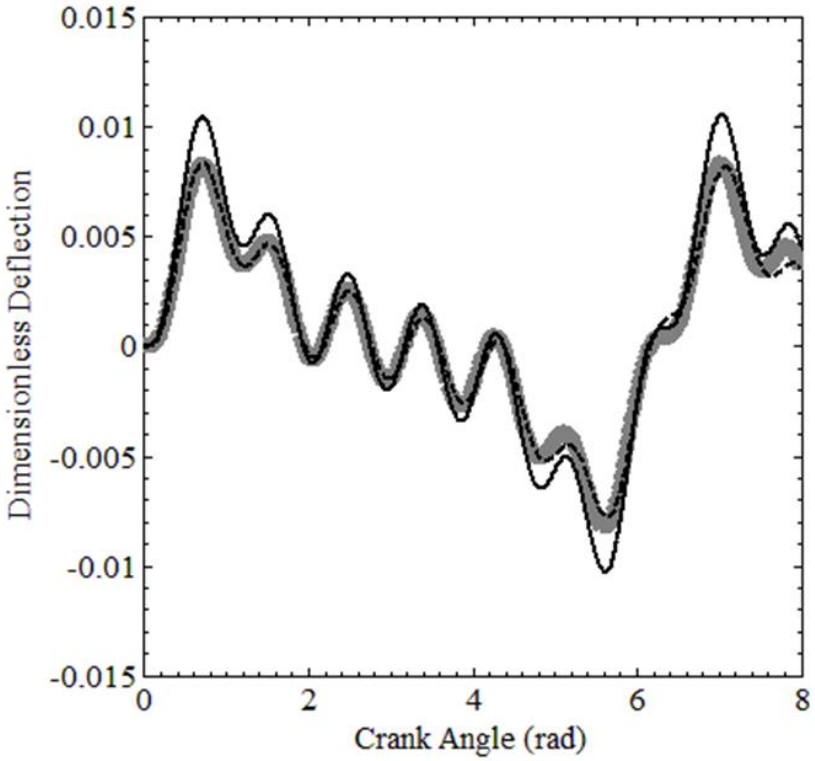

Figure 5.19. Dimensionless Deflection of Connecting Rod Center.

(▬▬▬ MBS-REF, - - - - - MBS-CB, ——— Analytical)

It is clear from the figure that both programs give an appropriate solution compared to the analytical solution. The error between the analytical and numerical solutions is due to the use of the finite element approximation when using two elements. The convergence of the two models is demonstrated in Figs. 5.20 and 5.21, where the simulation results are shown for a connecting rod discretized into 40 beam elements.

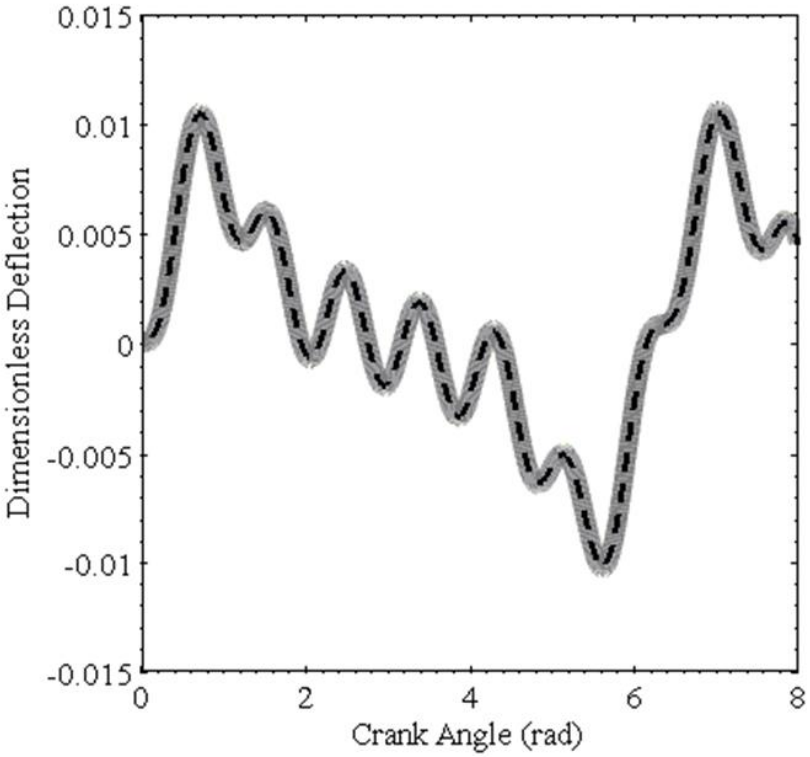

Figure 5.20. Dimensionless Deflection of Connecting Rod Center.

(Analytical, MBS-REF)

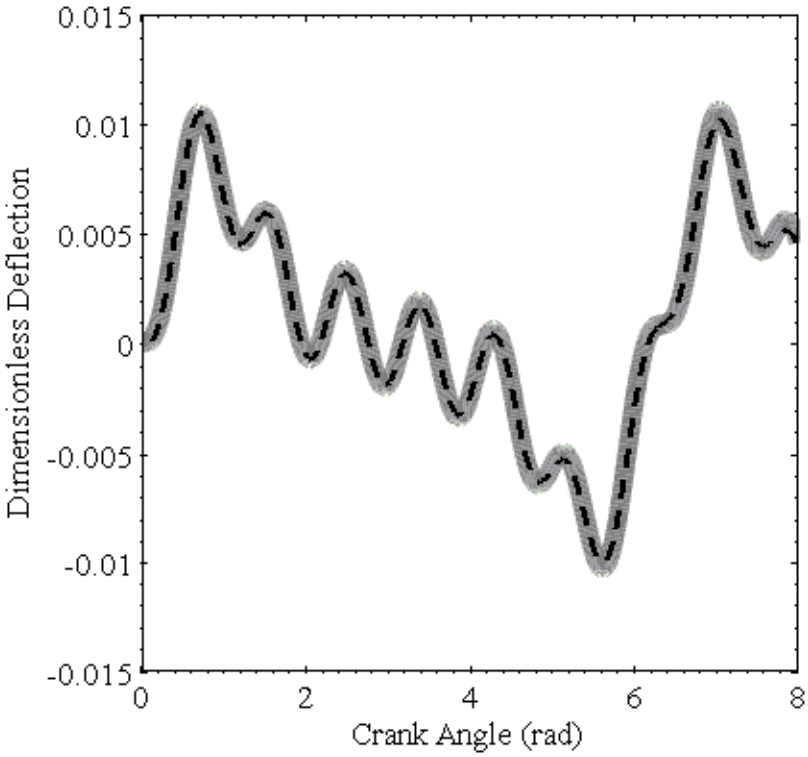

Figure 5.21. Dimensionless Deflection of Connecting Rod Center.

(Analytical, MBS-CB)

For this example, the free-free mode shapes are similar to the simply-supported mode shapes and therefore give similar results.

5.5.2 Extended Slider-Crank Mechanism Example

It was shown in the above section that the Craig-Bampton method performs correctly in the case where free-free modes of vibration have shapes that resemble the physical boundaries. This section

provides a counter-example to the use of free-free modes in all cases. A slider-crank mechanism similar to the one used in the previous example is shown in Fig. 5.22.

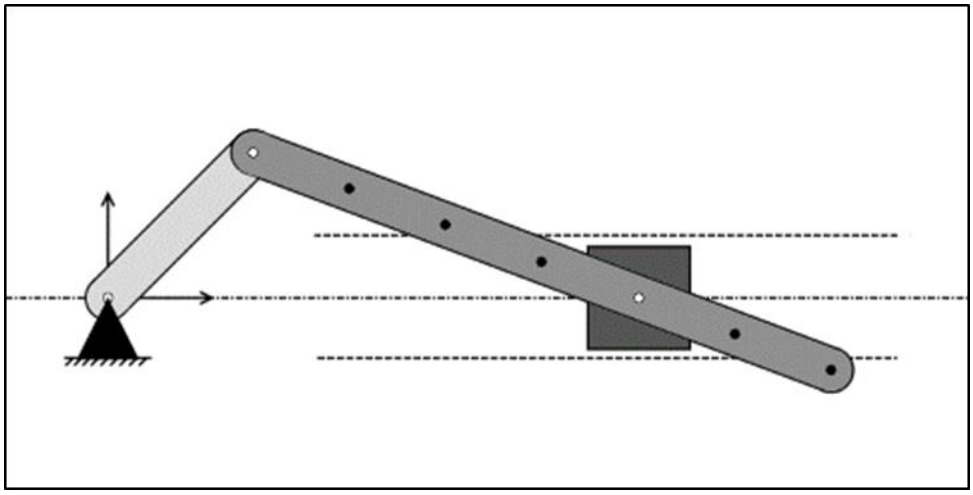

Figure 5.22. Extended Slider Crank Mechanism

In this example, the beam is 1.5 times longer and is modeled using 7 Euler-Bernoulli beam elements. This example will compare the use of the simply-supported modes to the free-free modes. The first six simply-supported modes are shown in Fig. 5.23.

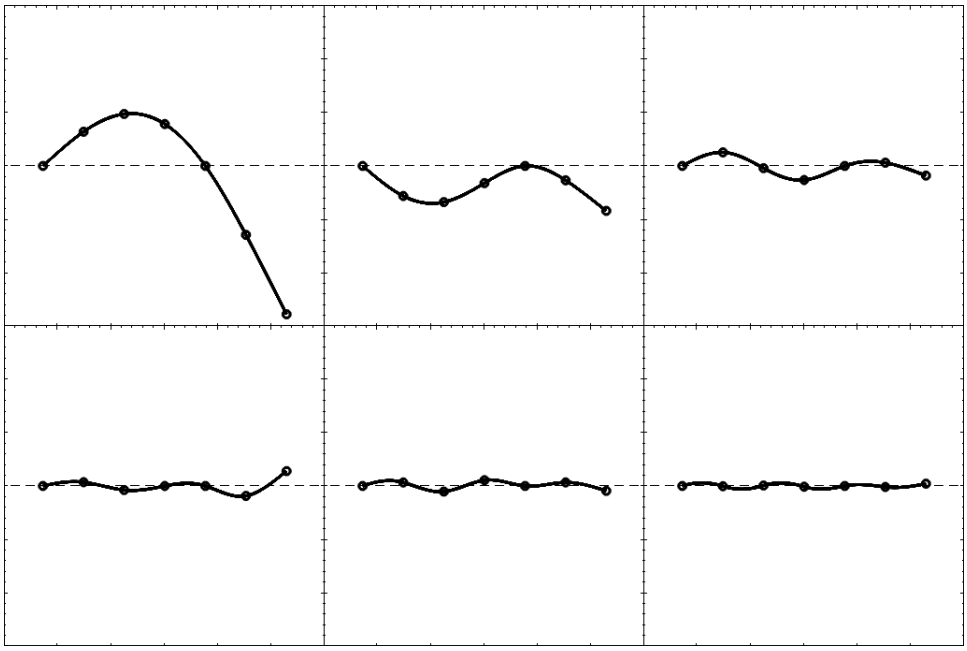

Figure 5.23. Simply-Supported Extended Connecting Rod Modes

(---------- Undeformed Beam Axis, ——— Deformed element)

(● Displaced nodal position)

Figure 5.24 shows the amplification of the first simply-supported mode. It is seen in the figure that increasing the modal coordinate does not affect the axial position of the nodes or the position of the slider block, which is consistent with Euler-Bernoulli beam theory.

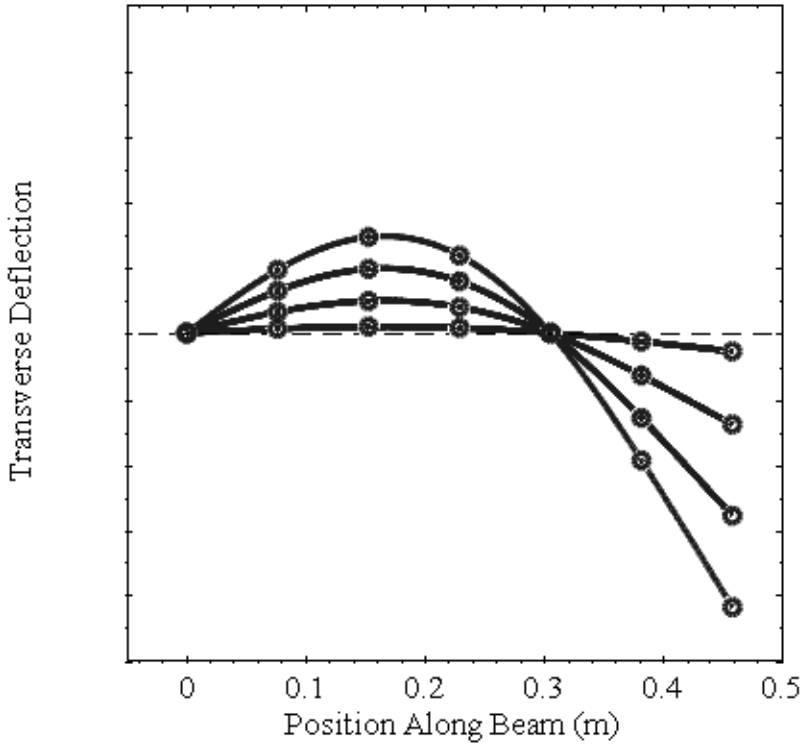

Figure 5.24. Amplification of the First Simply-Supported Extended Connecting Rod Mode

Figure 5.25 shows the amplification of the first free-free mode. It is seen that increasing this modal coordinate affects both the axial position of the nodes and the position of the slider block. One may then predict that the simulation of the model using free-free modes will result in an extension of the pinned section of the beam, and compression of the free section of the beam. This kind of axial extension and compression is not consistent with the kinematic constraints imposed on the boundary of the beam.

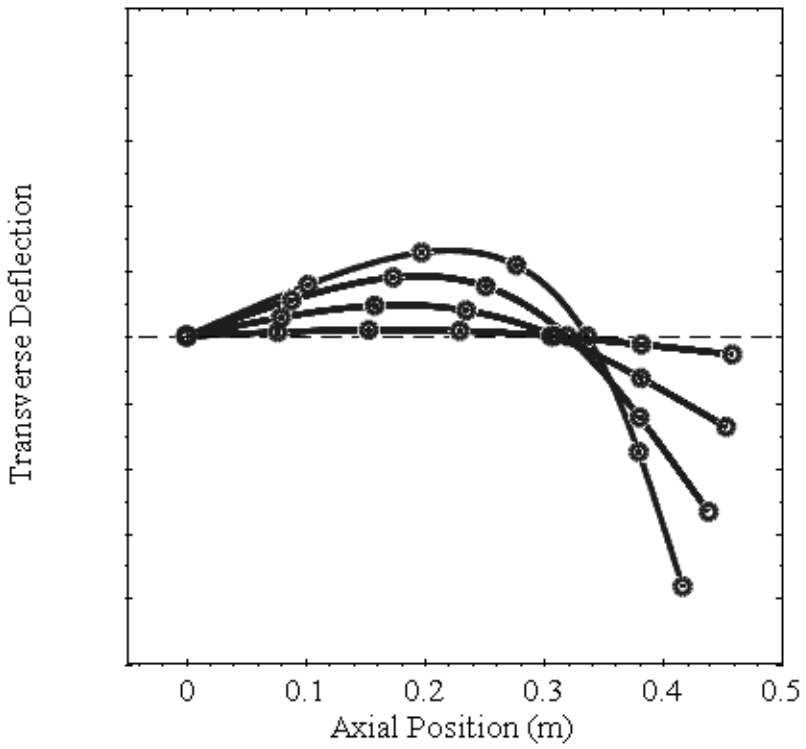

Figure 5.25. Amplification of the First Free-Free Extended Connecting Rod Mode

Figure 5.26 shows the deflection of the third node (center of the pinned section), while Fig. 5.27 shows the deflection of the seventh node (free end of the beam).

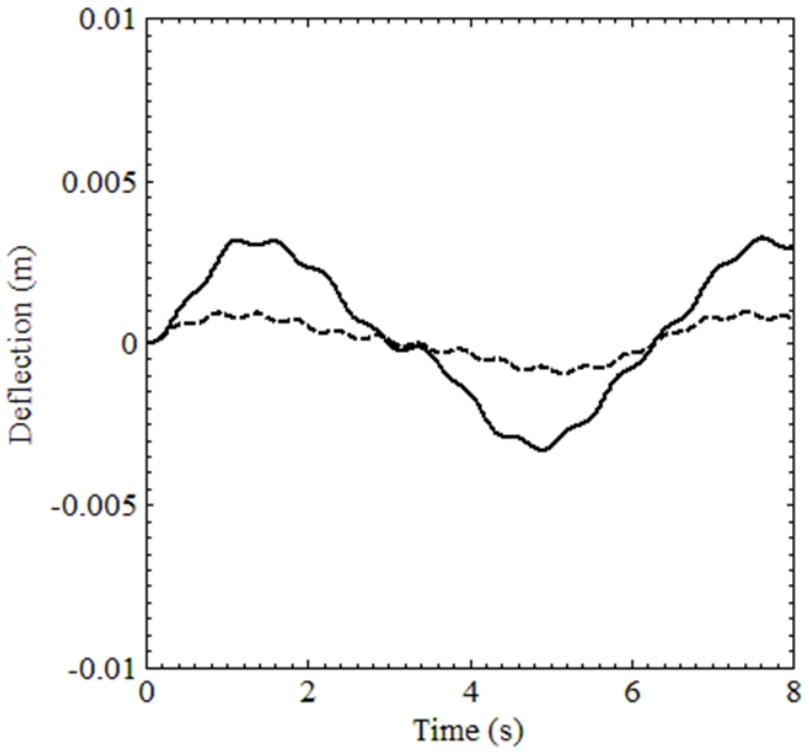

Figure 5.26. Deflection of the Connecting Rod 3rd Node

(———— Simply-Supported, ---------- Free-Free)

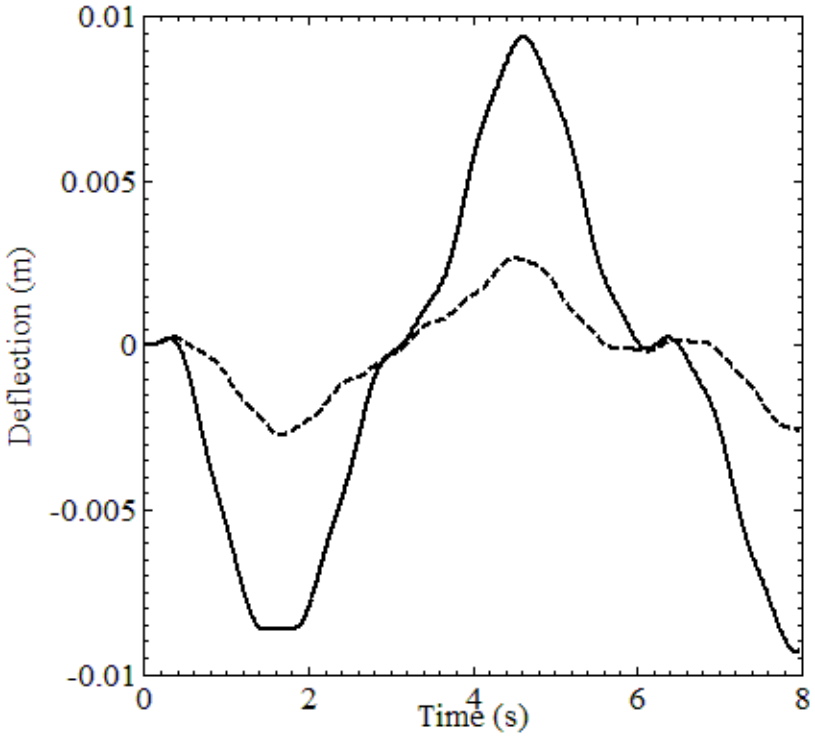

Figure 5.27. Deflection of the Connecting Rod Free End

(———— Simply-Supported, ---------- Free-Free)

In either case, the deflections produced using the free-free modes are smaller in magnitude than the results produced using the simply-supported modes. Figures 28 and 29 show the axial extension/compression of the pinned and free sections of the beam, respectively, as expected.

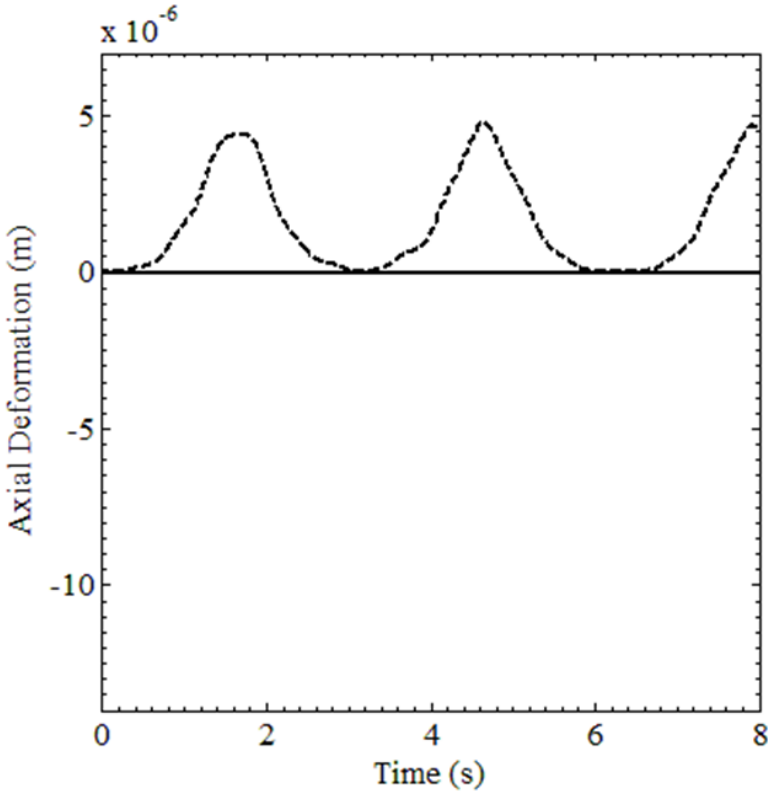

Figure 5.28. Extension of the Connecting Rod Pinned Section

(———— Simply-Supported, ---------- Free-Free)

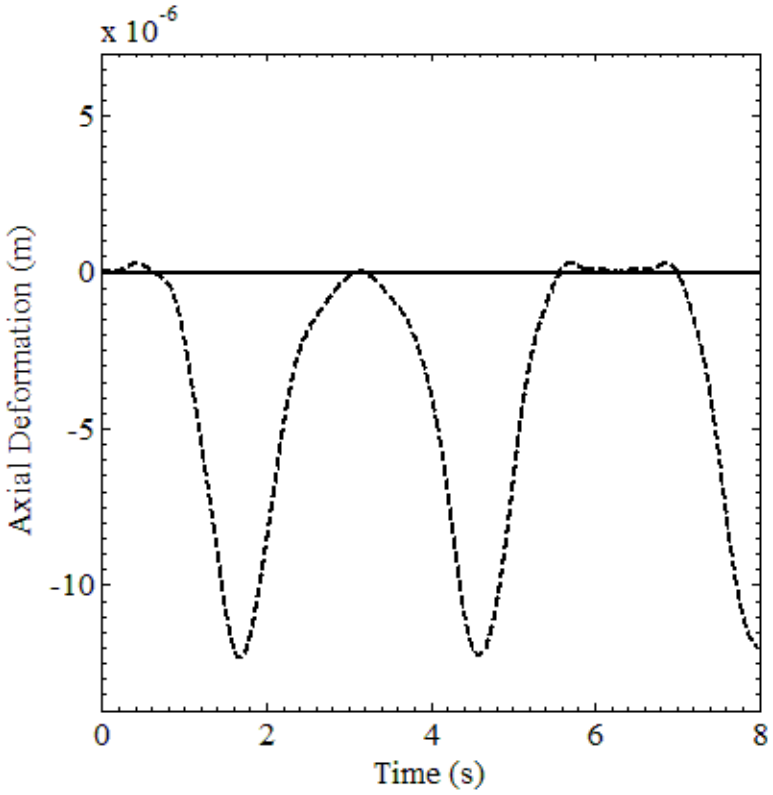

Figure 5.29. Extension of the Connecting Rod Free End
(———— Simply-Supported, ---------- Free-Free)

It is clear from these figures that axial extension/compression is only seen in the case of the free-free modes. This is a clear indication that the free-free modes are not appropriate for all cases.

5.6 Concluding Remarks

In this chapter, the motivation for the development and use of substructuring techniques and methods of component mode synthesis in MBS dynamics software is discussed. Subtleties of the FFR formulation, or the treatment of traditional finite elements for use in MBS software, are reviewed. In order to introduce some of the important concepts used in the FE/FFR formulation,

this chapter demonstrates numerically for the first time that the unique resonance frequency of a model can be achieved using different mode shapes associated with different boundary conditions provided that the shapes are similar. The Craig-Bampton method, a specific and popular substructuring technique used in MBS software, is also reviewed. Numerical results are then presented to demonstrate the importance of a general FFR implementation and the significance of the concept of the reference conditions. The Craig-Bampton method is a substructuring technique, which does not alter or improve the solution of the original problem, and it does not lead to a general implementation of the FFR formulation if its use is restricted to the free-free structure as demonstrated in this investigation. The use of the static correction modes does not alter this important fact. It is shown in this study that the Craig-Bampton method transforms the finite element problem to be defined in a new set of coordinates. While this transformation provides a convenient matrix structure for substructuring, such a transformation does not change the problem, and therefore, the Craig-Bampton transformation yields the solution of the original problem. It is shown by example that this transformation procedure is not general and cannot be used in all cases if restricted to one set of modes as it currently being used in some MBS software.

CHAPTER 6

CONCLUSIONS

Parts originally published or prepared in (Shabana et al., 2012; O'Shea and Shabana, 2015; O'Shea and Shabana, 2016; O'Shea et al., 2016) and reproduced in this dissertation with permission which is listed in Appendix A. Dr. Martin B. Hamper, Dr. Paramsothy Jayakumar, and Dave Mechergui are contributing authors.

It is shown in this dissertation that the generalized gyroscopic moment associated with the degree of freedom of a body can be insignificant in the case of curve negotiation when the yaw and roll angles are constrained and the motion is predominantly rolling. This, however, is not the case in derailment scenarios where the gyroscopic moments can be significant. As a result, the gyroscopic moments should be considered in developing derailment criteria for railroad vehicle systems. At high speeds, the roll gyroscopic moment can have a significant effect on the normal contact force at the wheels in contact with the rail. In the case of high speeds, all the moments acting on the wheel, including the gyroscopic moment, must be included in the analysis. The analysis presented in this chapter shows that the roll moment which can have a significant effect on the wheel/rail contact forces depends on the forward velocity in the case of curve negotiations. For this reason, roller rigs that do not allow for the wheelset forward velocity cannot be used in the analysis of curve negotiations.

The Nadal L/V derailment limit, along with subsequent derailment criteria, is developed in order to evaluate the proneness of a wheelset to a wheel climb derailment. Wheel climb derailments can initiate when the wheelset is in contact with the track at three distinct points. The

formulation presented in this dissertation demonstrates that the configuration of a wheelset in contact with a tangent track at three distinct points can be fully defined for a given AOA. It has been recently noted in the literature that the orientation of the wheelset at climb initiation, as well as the consequences of such orientation on the wheel/rail contact geometry, plays a significant role in the derailment. Because the system configuration is fully defined using the presented formulation, derailment parameters such as the wheel/rail contact angle can be solved for; this angle is compared against the wheelset flange angle for various angles of attack to enforce that a distinction must be made between the two values. Additionally, it is shown that the steepest point on the wheel flange is not necessarily in contact with the rail due to the orientation of the wheelset, and therefore, this point on the wheel profile should not be used in contact angle calculations by default. These results then raise concern with regards to the Nadal L/V derailment limit, which is a planar force balance and does not take into account the orientation of the wheelset. Additional concern is raised with regards to the practice of using the steepest section of the wheel flange to calculate the flange angle, which is then used as input to the Nadal calculation. The results of the formulation indicate the need for using the correct contact geometry in the investigations of the derailments of modern railroad systems.

Furthermore, there is a strong belief in the rail industry and research community that wheel climb at a large AOA is initiated by friction forces. It is believed that when the wheel comes into flange contact with the rail at a large AOA, an increase in the lateral force acting on the wheel leads to an increase in the normal reaction force at the flange contact point. Since in this case the contact point on the wheel is moving downward, the large reaction force normal to the flange produces significant upward friction force that results in wheel climb. A fully nonlinear MBS

wheel climb model is used in this dissertation in order to investigate the above interpretation of wheel climb derailments. The results obtained using this numerical model are analyzed in order to shed light on the forces that contribute to the wheel climb mechanism. It is shown that the contact between the wheel flange and rail introduces motion constraints that play a significant role in the initiation of the climb, and become more significant as the wheel climbs the rail. In addition to the reaction forces, the contact between the wheel flange and rail produces a friction force that is shown to have non-zero components in three Cartesian directions with respect to the rail and therefore cannot be captured using any planar analysis. It follows that the Nadal L/V Limit, which makes use of a planar force balance, does not correctly capture the friction force at the flange. This investigation also demonstrates that the forces measured at the flanging rail are not representative of the force that drives the derailment. The above conclusions raise additional questions to the current state of derailment criteria, and in particular the Nadal L/V Limit, which is shown to not predict the derailment presented in this investigation. The criteria may then not be deemed conservative. These important conclusions are further investigated using a semi-analytical model that is additionally formulated in this dissertation. The semi-analytical model is formulated using assumptions that are derived from the current interpretation of wheel climb in order to analyze the *initiation* of the wheel climb motion and the initiation only. The results of the semi-analytical model are compared with the results of the MBS model in order to validate the assumptions made to develop the semi-analytical model as well as provide insight into the derailment initiation of the MBS model. The two models, although very different in formulation, are in good agreement in the vicinity of the wheel climb initiation. The semi-analytical formulation raises question in regards

to use of the “distance to climb” measure used in some derailment criteria, as it is shown that the longitudinal motion is decoupled from the vertical and yaw displacements.

The fully nonlinear unconstrained MBS wheel climb derailment model is then used to confirm the importance of using the contact angle in the development of railroad vehicle derailment criteria. The correct contact angle was substituted into the formulation of the derailment limit in order to provide an updated criterion that correctly predicted the derailment of the wheelset. This result should not be interpreted as an appropriate derailment measure, but rather, as a rationalization and justification of the use of the correct contact geometry in derailment investigations.

Finally, the motivation for the development and use of substructuring techniques and methods of component mode synthesis in MBS vehicle dynamics software is discussed. Subtleties of the FFR formulation, or the treatment of traditional finite elements for use in MBS software, are reviewed. In order to introduce some of the important concepts used in the FE/FFR formulation, this dissertation demonstrates numerically for the first time that the unique resonance frequency of a model can be achieved using different mode shapes associated with different boundary conditions provided that the shapes are similar. The Craig-Bampton method, a specific and popular substructuring technique used in MBS software, is also reviewed. Numerical results are then presented to demonstrate the importance of a general FFR implementation and the significance of the concept of the reference conditions. The Craig-Bampton method is a substructuring technique, which does not alter or improve the solution of the original problem, and it does not lead to a general implementation of the FFR formulation if its use is restricted to the

free-free structure as demonstrated in this investigation. The use of the static correction modes does not alter this important fact. It is shown in this study that the Craig-Bampton method transforms the finite element problem to be defined in a new set of coordinates. While this transformation provides a convenient matrix structure for substructuring, such a transformation does not change the problem, and therefore, the Craig-Bampton transformation yields the solution of the original problem. It is shown by example that this transformation procedure is not general and cannot be used in all cases if restricted to one set of modes as it currently being used in some MBS software.

CITED LITERATURE

1. Agrawal, O.P., and Shabana, A.A., 1985, "Dynamic Analysis of Multibody Systems Using Component Modes", *Computers & Structures,* Vol. 21(6), pp. 1303-1312.

2. Ashley, H., 1967, "Observations on the Dynamic Behavior of Large Flexible Bodies in Orbit", *AIAA Journal,* Vol. 5, pp. 460 – 469.

3. Atmadzhova, D., and Mihaylov, E., 2010, "Tram Vehicle Movement Safety", *Transport Research and Business Cooperation in SEE Regional Workshop,* December 6-7, Sofia.

4. Bampton, M.C.C., and Craig Jr., R.R., 1968, "Coupling of Substructures for Dynamic Analyses", *AIAA Journal,* Vol. 6(7), pp. 1313-1319.

5. Barbosa, R.S., 2004, "A 3D contact force safety criterion for flange climb derailment of a railway wheel", *Vehicle System Dynamics,* vol. 42(5), pp. 289-300.

6. Blader, F.B., 1990, "A Review of Literature and Methodologies in the Study of derailment Caused by Excessive Forces at the Wheel/Rail Interface", *AAR Report,* R-717.

7. Braghin, F., Bruni, S., and Diana, G., 2006, "Experimental and Numerical Investigation on the Derailment of a Railway Wheelset with Solid Axle", *Vehicle System Dynamics,* vol. 44(4), pp. 305-325.

8. Caldwell, R.., 2010, "Pre-engineering the Wheel/Rail Interface." *Interface - The Journal of Wheel/Rail Interaction,* October Issue, http://www.interfacejournal.com/features/10-10/PreEngWRI/1.html.

9. Cherchas, D.B., 1981, "Determination of Railway Wheel Climb Probability Based on the Derailment Coefficient", *Journal of the Franklin Institute,* vol. 312 (1)

10. Choi, I. Y., Um, J. H., Lee, J. S., and Choi, H. H., 2012, "The Influence of Track Irregularities on the Running Behavior of High-Speed Trains", *Proceedings of the Institution of Mechanical Engineers, Part F: Journal of Rail and Rapid Transit,* 0954409712455146.

11. Chu, S.C., and K.C., Pan, 1975, "Dynamic Response of a High-Speed Slider-Crank Mechanism with an Elastic Connecting Rod", *Journal of Manufacturing Science and Engineering,* Vol. 97(2), pp. 542-550.

12. Craig Jr., R.R., 1983, *Structural Dynamics: An Introduction to Computer Methods*, 1st ed., Wiley, New York, New York.

13. Durali, M., and Jalili, M.M., 2010, "A New Criterion for Assessment of Train Derailment Risk", *Proceedings of the Institution of Mechanical Engineers, Part K: Journal of Multi-body Dynamics,* 224(1), 83-101.

14. Elkins, J., and Wu, H., 2000, "New Criteria for Flange Climb Derailment", *IEEE/ASME Joint Rail Conference,* Newark, New Jersey, April 4-6.

15. El-Sibaie, M., Jamieson, D., Tyrell, D.C., Dorsey, J.C., Mee, B., Whitten, B., and Kesler, K., 1997, "Engineering Studies in Support of the Development of High-Speed Track Geometry Specifications", *Proceedings of the IEEE/ASME Joint Railroad Conference,* Boston, Massachusetts, March 18-20.

16. Fraser, G. R., Leary, R. J., Marianeschi, M., Pellegrini, C., & Transportation Research Board, 2003, "Integrating New Light Rail Vehicle Technology into Mature Infrastructure. Experience", *Economics, and Evolution*, 119.

17. Ghazavi, M.R., and Taki, M., 2008, "Dynamic Simulations of the Freight Three-Piece Bogie Motion in Curve, *Vehicle System Dynamics*, vol. 46(10), pp. 955-973.

18. Gilchris, A.O., 1998. "The Long Road to Solution of the Railway Hunting and Curving Problems". *Proceedings of the Institution of Mechanical Engineers, Part F: Journal of Rail and Rapid Transit*, pp. 212–219.

19. Gilchrist, A.O., and Brickle, B.V., 1976, "A Re-Examination of the Proneness to Derailment of a Railway Wheel-Set", *Journal of Mechanical Engineering Science*, vol. 18(3), pp. 131-141.

20. Goldstein, H., 1950, *Classical Mechanics*, Addison-Wesley, Reading, Massachusetts.

21. Greenwood, D.T., 1988, *Principles of Dynamics*, Second edition, Prentice Hall, Englewood Cliffs, NJ.

22. Guan, Q., Zeng, J., & Jin, X., 2014, "An Angle of Attack-Based Derailment Criterion for Wheel Flange Climbing", *Proceedings of the Institution of Mechanical Engineers, Part F: Journal of Rail and Rapid Transit*, 228(7), 719-729.

23. Ishida, H., and Matsuo, M., 1999, "Safety Criteria for Evaluation of Railway Vehicle Derailment", *Quarterly Report of RTRI*, vol. 40(1), pp. 18-25.

24. Iwnicki, S., 2006, *Handbook of Railway Vehicle Dynamics*, CRC/Taylor & Francis, Boca Raton, FL.

25. Kalker, J.J., 1990, "Three-Dimensional Elastic Bodies in Rolling Contact", Kluwer, Dordrecht, Netherlands.

26. Kardas-Cinal, E., 2009, "Comparative Study of Running Safety and Ride Comfort of Railway Vehicle", C*oordinates*, 1(2), 27.

27. Koci, H.H., and Swenson, C.A., 1978, "Locomotive Wheel Loading – A System Approach", *Heavy Haul Railways Conference.* Perth, W.A., Australia.

28. Koo, J.S., and Oh, H.S., 2014, "A New Derailment Coefficient Considering Dynamic and Geometrical Effects of a Single Wheelset", *Journal of Mechanical Science and Technology*, vol. 28(9), pp. 3483-3498.

29. Kumar, A., 2014, "Derailment Assessment using FGB", *International Journal of Computer Sciences and Engineering*, vol. 2(8), pp. 103-107.

30. Leary, J.F., Handal, S.N., and Rajkumar, B., 1991, "Development of Freight Car Wheel Profiles", *Wear*, Vol. 144 (1-2).

31. Magel, E., Tajaddini, A., Trosino, M., & Kalousek, J., 2008, Traction, Forces, Wheel Climb and Damage in High-Speed Railway Operations, *Wear*, 265(9), 1446-1451.

32. Marquis, B., and Grief, R., 2011, "Application of Nadal Limit in the Prediction of Wheel Climb Derailment", *Proceedings of the ASME/ASCE/IEEE 2011 Joint Rail Conference*, Pueblo, Colorado, Paper # JRC2011-56064, March 16-18.

33. Matej, J., Piotrowski, J., Wojtyra, M., & Fraczek, J., 2002, "Modelling and Safety Examination of the Long Bimodal Train on Curved Track Using Adams/Rail", *In Proceedings of the 1st MSC. ADAMS European User Conference*, London, England, November.

34. Matsudaria, T., 1963, "Dynamics of high speed rolling stock", *Japanese National Railways RTRI Quarterly Reports*, Special Issue.

35. Mahyuddin, A.I., Febriartanto, A.N., Akbar, A., and Handoko, Y.A., 2011, "Multibody Dynamic Stability Analysis of a Diesel-Hydraulic Locomotive", *Journal of KONES*, vol. 18, pp. 219-226.

36. Mohammadzadeh, S., Sangtarashha, M., & Molatefi, H., 2011, "A Novel Method to Estimate Derailment Probability due to Track Geometric Irregularities using Reliability Techniques and Advanced Simulation Methods. *Archive of Applied Mechanics*, vol. 81(11), pp. 1621-1637.

37. Nadal, M.J., 1896, "Theorie de la Stabilité des Locomotives, Part 2", *Mouvement de Lacet, Annales des Mines*, vol. 10.

38. Nadal, M.J., 1908, Locomotives á Vapeur, *Collection Encyclopédie Scientifique, Bibliotéque de Mécanique Appliquée et Génie*, vol. 186.

39. Nagase, K., Wakabayashi, Y., & Sakahara, H., 2002, "A Study of The Phenomenon of Wheel Climb Derailment: Results of Basic Experiments Using Model Bogies", *Proceedings of the Institution of Mechanical Engineers, Part F: Journal of Rail and Rapid Transit*, 216(4), 237-247.

40. Nagumo, Y., Tanifuji, K., and Imai, J., 2010, "A Basic Study on Wheel Flange Climbing using Model Wheelset", *International Journal of Railway*, vol. 3(2), pp. 60-67.

41. Nagurka, M.L., Hedrick, J.K., and Wormley, D.N., 1983, "Curving Performance of Rail Transit Trucks", *Vehicle System Dynamics,* vol. 12(1-3), pp. 18-23.

42. Nishimura, Kazuhiko, Y. Terumichi, T. Morimura, and K. Sogabe, 2009, "Development of Vehicle Dynamics Simulation for Safety Analyses of Rail Vehicles on Excited Tracks". *Journal of Computational and Nonlinear Dynamics,* Vol 4(1), pp. 1-9.

43. O'Shea, J.J., Jayakumar, P., Mechergui, D., and Shabana, A.A., "Selection of Deformation Modes and Substructuring Techniques in Deformable Multibody Systems", in preparation.

44. O'Shea, J.J., and Shabana, A.A., 2015, "Analytical and Numerical Investigation of Wheel Climb at Large Angle of Attack", *Nonlinear Dynamics,* vol 83(1-2), pp. 555-577.

45. O'Shea, J.J., and Shabana, A.A., 2016, "Further Investigation of Wheel Climb Initiation: Three-Point Contact", in preparation.

46. Pearce, T.G., 1996, "Wheelset Guidance – Conicity, Wheel Wear and Safety", *Proceedings of the Institution of Mechanical Engineers, Part F: Journal of Rail and Rapid Transit,* Vol 210 (1) 1-9.

47. Rathod, C., and Shabana A.A., 2006, "Rail Geometry and Euler Angles", *ASME Journal of Computational and Nonlinear Dynamics,* Vol.1 (3), pp. 264-268.

48. Roberson, R.E., Schwertassek, R., 1988, *Dynamics of Multibody Systems,* Springer Verlag, Berlin.

49. Santamaria, J., Vadillo, E.G., and Gómez, J., 2009, "Influence of Creep Forces on the Risk of Derailment of Railway Vehicles, *Vehicle System Dynamics,* vol. 47(6), pp. 721-752.

50. Sato, Y., Matsumoto, A., Ohno, H., Oka, Y., & Ogawa, H., 2008, "Wheel/Rail Contact Analysis of Tramways and LRVs Against Derailment", *Wear,* 265(9), 1460-1464.

51. Schindler, C., Schwickert, M., & Simonis, A, 2010, "Structural Safety of Trams in Case of Misguidance in a Switch", *Vehicle System Dynamics,* vol. 48(8), pp. 967-981.

52. Shabana, A.A., 1982, "Dynamics of Large Scale Flexible Mechanical Systems", Ph.D. dissertation, University of Iowa, Iowa City.

53. Shabana, A.A., 1996, "Resonance Conditions and Deformable Body Co-ordinate Systems", *Journal of Sound and Vibration,* Vol. 192(1), pp. 389-398.

54. Shabana, A. A., 2010, Computational Dynamics. 3rd ed. Chichester, West Sussex: John Wiley & Sons.

55. Shabana, A.A., 2012, "Nadal's Formula and High Speed Rail Derailments", *ASME Journal of Computational and Nonlinear Dynamics,* Vol 7(4): 041003-041003-8.

56. Shabana, A.A., Hamper, M.B., and O'Shea, J.J., 2012, "Rolling Condition and Gyroscopic Moments in Curve Negotiations", *Journal of Computational and Nonlinear Dynamics*, Vol. 8(1), 011015-011015-10.

57. Shabana, A.A, 2013, *Dynamics of Multibody Systems*, 4th ed., Cambridge University Press, New York, New York.

58. Shabana, A.A. and O'Shea, J.J., 2013, "Large Angle of Attack Wheel Climb", *Proceedings of the ASME 9th International Conference on Multibody System, Nonlinear Dynamics, and Control*, **7**, Portland, Oregon.

59. Shabana, A.A., and Sany, J.R., 2001, "An Augmented Formulation for Mechanical Systems with Non-Generalized Coordinates: Application to Rigid Body Contact Problems", *Nonlinear Dynamics*, Vol. 24(2), 183-204.

60. Shabana, A.A., Zaazaa, K.E., and Sugiyama, H., 2008, Railroad Vehicle Dynamics: A Computational Approach, Taylor & Francis/CRC, Boca Raton, FL.

61. Shust, W.C., Elkins, J.A., Kalay, J.A., and El-Sibaie, M., 1997, "Wheel Climb Derailment Tests Using AAR's Track Loading Vehicle", *Association of American Railroads Report,* R-910.

62. Simpson, M., Blewitt, W., Ushaw, G., & Morgan, G., 2014, "Utilization of Video Game Physics Techniques in Real Time Simulation of the Wheel Rail Interface for Predicted Derailment of Rail Vehicles", *Newcastle University Computing Science Technical Report Series,* CS-TR-1438.

63. Takai, H., Uchida, M., Muramatsu, H., and Ishida, H., 2002, "Derailment Safety Evaluation by Analytic Equations", *Quarterly Report of RTRI*, vol. 43(3), pp. 119-124.

64. Wang, W., & Li, G. X., 2010, "Development of a Simulation Model of a High-Speed Vehicle for a Derailment Mechanism", *Proceedings of the Institution of Mechanical Engineers, Part F: Journal of Rail and Rapid Transit*, 224(2), 103-113.

65. Wei, L., Zeng, J., Wu, P., and Gao, H., 2014, Indirect Method for Wheel–Rail Force Measurement and Derailment Evaluation", *Vehicle System Dynamics*, vol. 52(12), pp. 1622-1641.

66. Weinstock, H., 1984, "Wheel Climb Derailment Criteria for Evaluation of Rail Vehicle Safety", *In Proceedings of the ASME Winter Annual Meeting*, Vol. 84, pp. 1-7.

67. Wilson, N., Shu, X., and Kramp, K., 2004, "Effect of Independently Rolling Wheels on Flange Climb Derailment", *Proceedings of the ASME International Mechanical Engineering Congress,* 10.1115/IMECE2004-60293.

68. Wu, H., and Elkins, J., 1999, "Investigation of Wheel Flange Climb Derailment Criteria" *Association of American Railroads Report,* R-931.

69. Wu, H., Shu, X., Wilson, N. and Shust, W, 2005, “Flange Climb Derailment Criteria and Wheel/Rail Profile Management and Maintenance Guidelines for Transit Operations”, *TCRP Report*, 71.

70. Wu, H., and Wilson, N., 2006, “Railway Vehicle Derailment and Prevention”, *Handbook of Railway Vehicle Dynamics*, S.D. Iwnicki, Chapter 8, Taylor & Francis, London.

71. Xiao, X., Jin, X., Deng, Y., and Zhou, Z, 2008, “Effect of Curved Track Support Failure on Vehicle Derailment”, *Vehicle System Dynamics*, vol. 46(11), pp. 1029-1059.

72. Zeng, J., & Guan, Q.H., 2008, “Study on Flange Climb Derailment Criteria of a Railway Wheelset,” *Vehicle System Dynamics*, vol. 46(3), pp. 239-251.

73. Zeng, J., and Wu, P., 2008, “Study on the Wheel/Rail Interaction and Derailment Safety”, *Wear*, Vol. 265, pp. 1452 – 1456

APPENDIX A

PERMISSIONS - SPRINGER

This is a license agreement between:	James J. O'Shea and Springer.
License Number:	3827680050218
License Date:	March 14, 2016
Licensed Content Publisher:	Springer
Licensed Content Publication:	Nonlinear Dynamics
Licensed Content Title:	Analytical and Numerical Investigation of Wheel Climb at Large Angle of Attack
Licensed Content Author:	James J. O'Shea
Licensed Content Date:	Jan 1, 2015
Type of Use:	Thesis/Dissertation
Portion:	Full Text
Number of Copies:	100000
Author of this Springer Article:	James J. O'Shea, and he is the sole author of the new work
Title of Thesis/Dissertation:	Use of Multibody System Techniques in the Analysis of Railroad Vehicle Stability and Derailment
Expected Completion Date:	Mar 2016

PERMISSIONS - ASME

It is our pleasure to grant you permission to use **all or any part of** the following ASME papers:

· Rolling Condition and Gyroscopic Moments in Curve Negotiations, by Ahmed A. Shabana; Martin B. Hamper; James J. O'Shea, Paper Number DETC2012-70675
· Rolling Condition and Gyroscopic Moments in Curve Negotiations, by Ahmed A. Shabana; Martin B. Hamper; James J. O'Shea, J. Comput. Nonlinear Dynam. 2012; 8(1)

cited in your letter for inclusion in a Doctoral Dissertation entitled Use of Multibody System Techniques in the Analysis of Railroad Vehicle Stability and Derailment to be published by University of Illinois at Chicago (UIC).

Permission is granted for the specific use as stated herein and does not permit further use of the materials without proper authorization. Proper attribution must be made to the author(s) of the materials. **Please note**: if any or all of the figures and/or Tables are of another source, permission should be granted from that outside source or include the reference of the original source. ASME does not grant permission for outside source material that may be referenced in the ASME works.

As is customary, we request that you ensure full acknowledgment of this material, the author(s), source and ASME as original publisher. Acknowledgment must be retained on all pages printed and distributed.

Many thanks for your interest in ASME publications.

Sincerely,

Beth Darchi
Publishing Administrator
ASME
2 Park Avenue, 6th Floor
New York, NY 10016-5990
Tel 1.212.591.7700
darchib@asme.org

APPENDIX B

CONSTRAINT BASED FORMULATION

A vector of system coordinates is defined as $\mathbf{q}=\left[\left(\mathbf{q}^1\right)^T \quad \left(\mathbf{q}^2\right)^T \quad \ldots \quad \left(\mathbf{q}^{n_b}\right)^T\right]^T$, where $\mathbf{q}^i=\left[\left(\mathbf{R}^i\right)^T \quad \left(\boldsymbol{\theta}^i\right)^T\right]^T$ is the vector that contains the translational $\mathbf{R}^i$ and rotational $\boldsymbol{\theta}^i$ coordinates of body i, and n_b is the number of bodies in the system. The position of a point p on body i may then be written as $\mathbf{r}_p^i=\mathbf{R}^i+\mathbf{A}^i\bar{\mathbf{u}}_p^i$, where $\mathbf{A}^i=\mathbf{A}\left(\boldsymbol{\theta}^i\right)$ is the matrix that defines the orientation of body i in terms of the orientation parameters $\boldsymbol{\theta}^i$, and $\bar{\mathbf{u}}_p^i$ is the local definition of the position of point p with respect to a body coordinate system. In order to define the contact between bodies in the system, the local position of a point on body i is written using two surface parameters s_1^i and s_2^i as $\bar{\mathbf{u}}_p^i=\bar{\mathbf{u}}_p^i\left(s_1^i,s_2^i\right)=\left[x_p^i\left(s_1^i,s_2^i\right) \quad y_p^i\left(s_1^i,s_2^i\right) \quad z_p^i\left(s_1^i,s_2^i\right)\right]^T$. The vector of system surface parameters can be written as $\mathbf{s}=\left[\mathbf{s}_1^T \quad \mathbf{s}_2^T \quad \ldots \quad \mathbf{s}_{n_k}^T\right]^T$, where $\mathbf{s}_k$ is the set of surface parameters required to define a contact point on the surfaces of the two bodies, and n_k is the number of contact points in the system. The vector of surface parameters is then combined with the vector of system coordinates to form the vector of system variables $\mathbf{p}=\left[\mathbf{q}^T \quad \mathbf{s}^T\right]^T$, which has a total of n coordinates (Shabana, 2010).

In order to solve for the n unknown system variables, a system of n equations must be formulated and then solved for, which can be accomplished by formulating a set of kinematic constraint equations $\mathbf{C}$ such that $\mathbf{C}\left(\mathbf{p}\right)=\mathbf{0}$. The translational and rotational motion of a body i, and in the case of this investigation: the track, may be completely restricted using six fixed coordinate constraint equations $\mathbf{q}^i-\mathbf{c}^i=\mathbf{0}$, where $\mathbf{c}^i$ is a constant vector containing the fixed coordinates (Shabana, 2010). The requirement that two bodies i and j remain in contact requires the definitions of tangent planes and normal vectors at each contact point on body i which may be defined by $\bar{\mathbf{t}}_1^i=\partial\bar{\mathbf{u}}_p^i/\partial s_1^i$ and $\bar{\mathbf{t}}_2^i=\partial\bar{\mathbf{u}}_p^i/\partial s_2^i$. The normal to this plane may be then written as $\bar{\mathbf{n}}^i=\bar{\mathbf{t}}_1^i\times\bar{\mathbf{t}}_2^i$. Each contact introduces five constraint equations that may be written as $\left[\mathbf{t}_1^j\cdot\mathbf{r}_p^{ij} \quad \mathbf{t}_2^j\cdot\mathbf{r}_p^{ij} \quad \mathbf{n}^j\cdot\mathbf{r}_p^{ij} \quad \mathbf{t}_1^i\cdot\mathbf{n}^j \quad \mathbf{t}_2^i\cdot\mathbf{n}^j\right]^T=\mathbf{0}$, where $\mathbf{r}_p^{ij}=\mathbf{r}_p^i-\mathbf{r}_p^j$. The first three equations require that the positions of the contact points on the two surfaces coincide, while the last two equations require that the two surfaces have the same tangent plane at the point of contact (Shabana et al., 2008). Finally, the values of any remaining degrees of freedom may be specified using driving constraints, which define the system configuration.

APPENDIX C

USE OF SIMPLIFIED MODEL

In the analysis of railroad vehicle systems, wheel climb at a large angle of attack is an example of a complex dynamic situation. The results of a MBS formulation are presented in this study, which have contributions from many factors that may not be clear. Therefore, in this dissertation, a model is presented that uses simplified wheel/rail contact geometry as well as motion constraints, in order to distinctly highlight certain contributions to the wheel climb initiation and to formulate a semi-analytical solution. The results of the MBS model in the vicinity of the wheel climb initiation are verified using this semi-analytic model. It is understood that, because of the assumptions and simplifications made, the results of the simplified model will deviate from the results of the fully nonlinear unconstrained model as the wheel climb progresses, and therefore, the results of the simplified model are of interest only in the vicinity of the climb initiation. While this simplified model may differ from the actual physical situation, the advantage of the simplified model shedding light on the basic principles and forces that govern the conditions at which wheel climb initiates hold useful. The simplified model has additional advantages such as being able to model multiple geometric scenarios; for example, climb that occurs on the wrong side of the flange when making contact with a guard rail could additionally be modeled using the presented simplified formulation. The results of the two models, in conjunction, can provide comprehensive insight into the derailment process and can help in the future to develop derailment prevention criteria.

APPENDIX D

ALTERNATIVE CONTACT CONSTRAINT FORMULATION

This appendix provides an alternative derivation of the single constraint of Eq. 4.5. This derivation was proposed by one of the chapter's anonymous reviewers of a previous version of the chapter and is outlined as follows. Two right triangles can be formed when considering a disk that is in contact with a line on its lower half. The first exists in the local $X^w Z^w$ plane of the disk and is shown in Fig. D.1.

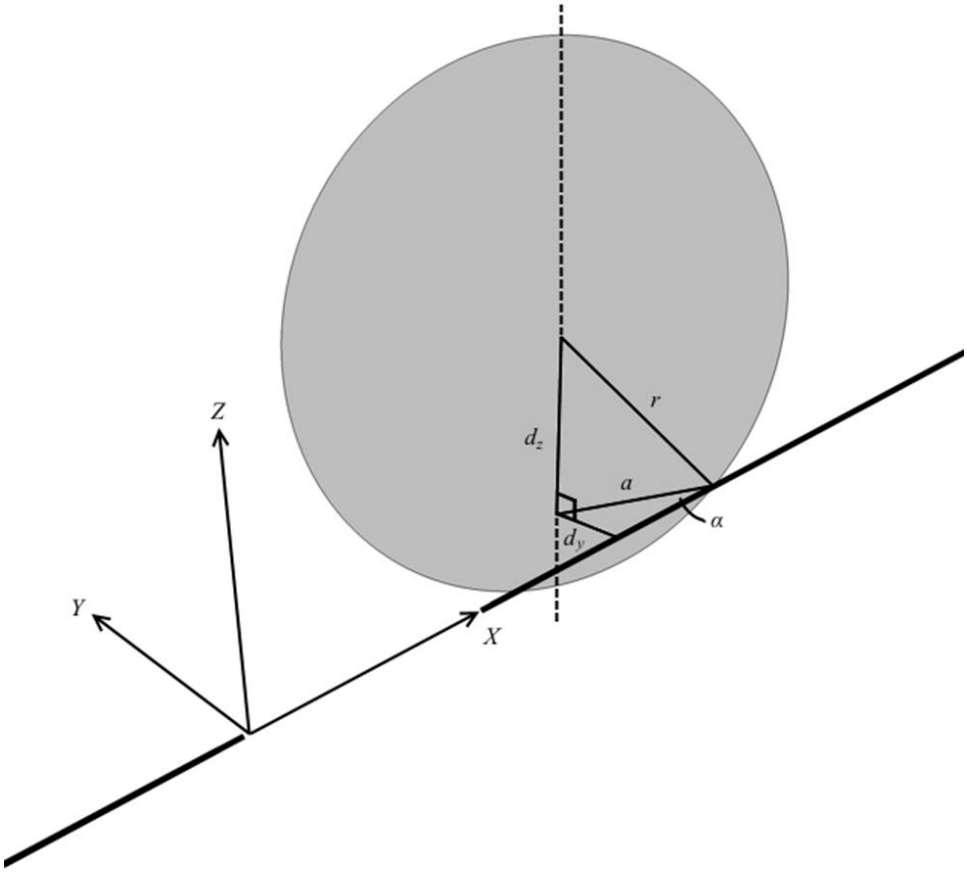

Figure D.1. Disk/Rail Contact Constraint

Using the Pythagorean Theorem, one has

$$\left(d_z\right)^2 + a^2 = r^2 \tag{D.1}$$

The second triangle exists in the XY plane and is also shown in Fig. C.1. The angle of attack α and the lateral position of the disk center with respect to the point of contact R_y are related by

$$d_y = a\sin\alpha \tag{D.2}$$

If Eqs. D.1 and D.2 are combined by eliminating the variable a, the resulting equation is

$$\left(d_y\right)^2 + \left(d_z\right)^2 \sin^2\alpha = r^2 \sin^2\alpha \tag{D.3}$$

which is the same as Eq. 4.5 previously presented in the dissertation.

VITA

JAMES JOSEPH O'SHEA

EDUCATION

Doctoral Candidate, Mechanical Engineering **Expected May 2016**
University of Illinois at Chicago
- Use of Multibody System Techniques in the Analysis of Railroad Vehicle Stability and Derailment

Bachelor of Science, Mechanical Engineering **Earned May 2011**
University of Illinois at Chicago

PROFESSIONAL EXPERIENCE

Research and Development Engineer **May 2014 - Present**
Computational Dynamics, Inc.
- Design, development, testing, and optimization of MBS software engine and interface. Development tasks include upgrading research software to commercial standards, implementation of finite element concepts into graphics calculations. Design tasks include MBS model creation for applications such as railroad transportation as well as various mechanisms.

Teaching Assistant **Jan 2013 - May 2014**
Department of Mechanical Engineering, UIC
- Tasks include grading of homework assignments and examinations, validation of homework solutions provided by faculty, and holding of office hours to which students attend voluntarily for additional assistance with the lecture material.

Research Assistant **May 2011 - May 2014**
Dynamic Simulation Laboratory, UIC
- Development of the general purpose MBS dynamics software SAMS/2000 (now SIGMA/SAMS), as well as railroad industry specific module SAMS/RAIL and stand-alone application ATTIF. Tasks include formulating mathematical models of multibody systems of interconnected rigid and deformable bodies. Additionally, extensive use of FORTRAN in the development and use of wheel/rail contact subroutines.

ADDITIONAL EXPERIENCE

Student Researcher | NASA Student Airborne Research Project 2011
Corporate Intern | Caterpillar, Inc. 2010

ACADEMIC HONORS & AWARDS

Outstanding Student of the Year **Jan 2015**
National University Rail (NURail) Center
- Awarded by the United States Department of Transportation (USDOT) Council of University Transportation Centers (CUTC) at the Transportation Research Board (TRB) annual meeting in Washington, DC.

Member **May 2010**
Pi Tau Sigma (PTS) Mechanical Engineering Honor Society

JOURNAL PUBLICATIONS

O'Shea, J.J. & Shabana, A.A., 2015, "Analytical and Numerical Investigation of Wheel Climb at Large Angle of Attack", *Journal of Nonlinear Dynamics,* Vol. 83, pp. 555-577.

Shabana, A.A., Hamper, M.B., & O'Shea, J.J., 2013, "Rolling Condition and Gyroscopic Moments in Curve Negotiations" *Journal of Computational and Nonlinear Dynamics*, Vol. 8(1), 011015.

CONFERENCE PUBLICATIONS & TECHNICAL REPORTS

Shabana, A.A. & O'Shea, J.J., 2013, "Large Angle of Attack Wheel Climb", *Proceedings of the ASME 2013 International Design Engineering Technical Conferences and Computers and Information in Engineering Conference,* Vol. 7B: 9th International Conference on Multibody Systems, Nonlinear Dynamics, and Control, Portland, OR, USA, August 4-7.

Shabana, A.A., Hamper, M.B., & O'Shea, J.J., 2012, "Rolling Condition and Gyroscopic Moments in Curve Negotiations", *Proceedings of the ASME 2012 International Design Engineering Technical Conferences and Computers and Information in Engineering Conference,* Vol. 6: 1st Biennial International Conference on Dynamics for Design; 14th International Conference on Advanced Vehicle Technologies, Chicago, Illinois, USA, August 12-15.

CONFERENCE & SEMINAR PRESENTATIONS

O'Shea, J.J., 2013, "Wheel Climb at a Large Angle of Attack", *2013 UIC Workshop on Multibody System Dynamics,* Chicago, IL, USA, August 10.

O'Shea, J.J., 2013, "Large Angle of Attack Wheel Climb", *ASME 2013 International Design Engineering Technical Conferences and Computers and Information in Engineering Conference,* Portland, OR, USA, August 4-7.

O'Shea, J.J., 2013, "Large Angle of Attack Wheel Climb", *ASME 2013 Joint Rail Conference*, National University Rail Center Session, Knoxville, TN, USA, April 15-18.

O'Shea, J.J., 2012, "Rolling Condition and Gyroscopic Moments in Curve Negotiations", *ASME 2012 International Design Engineering Technical Conferences and Computers and Information in Engineering Conference*, Chicago, Illinois, USA, August 12-15.

PROFESSIONAL SERVICE

Reviewer of Technical Journal Papers

- Proceedings of the Institution of Mechanical Engineers, Part F: Journal of Rail and Rapid Transit — 2013 - 2015

- ASME Journal of Computational and Nonlinear Dynamics — 2014

Reviewer of Technical Conference Papers

- International Design Engineering Technical Conferences & Computers and Information in Engineering Conference — 2014

COLLABORATIONS

Selection of Deformation Modes and Substructuring Techniques in Deformable Multibody Systems — **July 2015 - Present**
- Dr. Paramsothy Jayakumar, US Army TARDEC
- David Mechergui, US Army TARDEC

Significance of Forward Velocity in Roller Rig Simulations — **Mar 2012 - Dec 2012**
- Andrea Erba, Politecnico di Milano

Rail Motion and Gyroscopic Moments in Seismic Regions — **Mar 2012 - Dec 2012**
- Samuele Reggiani, Politecnico di Milano

TECHNICAL ACUMEN

Computer Languages:	.NET Frameworks, MATLAB, FORTRAN, & Introductory C++
Programming Approaches:	Object-Oriented, Procedural
Source/Revision Control:	Git, Bitbucket
CAE Simulation:	SIGMA/SAMS (formerly SAMS/2000)
Office Suites:	Microsoft Office, iWork
Productivity & Management:	GTD in Evernote, XMind
Operating Systems:	Windows, Mac

LEADERSHIP

Member | National University Rail (NURail) Student Leadership Council	2013 - Present
Secretary | Pi Tau Sigma (PTS) National Engineering Honor Society	2010 - 2011
President | Beta Kappa Zeta (BKZ) Philanthropic Fraternity	2011 - 2013

CITIZENSHIP

United States Citizen